NTNU
Det skapende universitet

Evaluering av Bentonittplugg for tetning av borehull i en brønn

Samir Abdellah Rashid

Geofag og petroleumsteknologi
Innlevert: Februar 2013
Hovedveileder: Sigbjørn Sangesland, IPT

Norges teknisk-naturvitenskapelige universitet
Institutt for petroleumsteknologi og anvendt geofysikk

NTNU – Trondheim
Norwegian University of
Science and Technology

NTNU
Institutt for petroleumsteknologi
og anvendt geofysikk

Samir A. Rashid

Evaluation of Bentonite Plug for Sealing of Well Bore

Master of Science Thesis **February 28th 2013**

Norwegian University of Science and Technology
Department of Petroleum Engineering and Applied Geophysics

NTNU

Norges teknisk-naturvitenskapelige universitet

Fakultet for ingeniørvitenskap og teknologi

Faculty of Engineering and Technology

Studieprogram i Geofag og petroleumsteknologi

Study Programme in Earth Sciences and Petroleum Engineering

Institutt for petroleumsteknologi og anvendt geofysikk

Department of Petroleum Engineering and Applied Geophysics

HOVEDOPPGAVE/DIPLOMA THESIS/MASTER OF SCIENCE THESIS

Kandidatens navn/The candidate's name:	*Samir A. Rashid*
Oppgavens tittel, norsk/Title of Thesis, Norwegian:	*Evaluering av Bentonittplugg for tetning av borehull i en brønn*
Oppgavens tittel, engelsk/Title of Thesis, English	*Evaluation of Bentonite Plug for Sealing of Well Bore*

Utfyllende tekst/Extended text:

Background:

Cement has always been the most used sealing material, both for primary cementing and for plug and abandonment (P&A) of oil and gas wells. However, cement has problems related to shrinking, micro annuli and cracking due to subsurface movements, etc. Alternative sealing may be to use more flexible materials like Bentonite and Baryte. The main objective is to investigate how Bentonite pellets /Baryte materials can be used for plugging of boreholes.

Tasks:

Review performed studies and researches focusing on experiences using bentonite pellets as sealing material for plug and abandonment operations.
Plan and perform laboratory experiments and evaluate the mechanism of fluid transport in Bentonite/Barite plugs.
Discuss the results and propose possible arrangements for plugging of wellbores using Bentonite/Baryte and/or other equivalent materials.

Supervisor	*Sigbjørn Sangesland*
Co-supervisor	
Studieretning/Area of specialization:	*Petroleum Engineering, Drilling Technology*
Fagområde/Combination of subject:	*Drilling*
Tidsrom/Time interval:	*August 27th 2012 – February 28th 2013*

……

Sigbjørn Sangesland

PREFACE

This report is a result of my master thesis written during my tenth semester at the department of Petroleum Engineering and Applied Geophysics, Norwegian University of Science and Technology in Trondheim. The subject was suggested by Professor Sigbjørn Sangesland.

The main object of this thesis has been to investigate how bentonite pellets and or barite materials can be used for plugging of boreholes. The materials have been tested each by itself and when mixed together.

Barite has besides been tested for in dry powder form, and when mixed with water and allowed to settle. The settled barite has then been prepared for testing of its sealing properties in a pipe against water under pressure.

Bentonite pellets have additionally been hydrated and mechanically drained of its water, then tested for its sealing properties. This was done through a series of tests where water under pressure was being pushing toward a column of bentonite mix with barite in a pipe. Hydrated bentonite has as well been drained of much of its water content in a specially made Oedometer. Then the drained sample tested for its sealing properties by injecting water from under the sample, inside the Oedometer, at the same time as a compressive piston force of varying magnitude placed on top of sample.

I would like to address my acknowledgments to my supervisor professor Sigbjørn Sangesland for support and guidance throughout the thesis. I would also like to show my sincere gratitude to professors Pål Skalle; Ole Torsæter; Rune Holt; Arnfinn Emdal and Charlie Lee for their advices and support from the beginning. I am also indebted to Roger Overå for help at NTNU laboratories and to PTS workshop personnel for manufacturing the equipment needed for the different tests. At last I would like to send special thanks to my SINTEF liaison Mohamed Bhujan for his help and guidance at SINTEF laboratories.

Trondheim 28th of February 2013

Samir Rashid

SUMMARY

The basic technologies associated with the plugging and abandoning of wells has not changed significantly since the 1970s. Water-based slurries of cement and drilling mud are still the basic materials used to plug most wells although progress has been made in use of additives to customize the cements and muds for specific types of wells.

The maturation of the oil and gas industry worldwide is resulting in a large number of idle and orphaned wells in addition to the ever increasing number of wells waiting to be abandoned. The need for reliable and cost effective means of well abandoning technology has never been more acute. In the search for new plugging materials, bentonite has been acknowledged as possibly the ideal alternative material.

In this thesis, bentonite has been evaluated as an alternative sealing material to cement for plug and abandonment of wells. The sealing properties of bentonite and barite has been investigated and put to test. Attempts have been made to connect the theories describing the mechanism of fluid transport in rigid porous material to the fluid transport mechanism in clays, specifically bentonite. For the rigid materials, the theories attribute displacement of fluids to capillary forces between fluids phases occupying pore spaces.

Theory of poroelasticity attributes fluid displacement in rigid materials to the pores and cracks filled with fluids. When the material undergoes compression, pore fluid pressure would cause the state of stress to move closer to the failure surface in a Mohr circle. Additionally, pore fluid pressures give rise to macroscopic elastic deformation of the material. Fluids flow in rocks in response to gradients in the pore pressure, but can also flow due to changes in the macroscopic stresses due to natural causes such as tectonic forces, and man-made causes such as the drilling of boreholes, etc. The hydrological behavior and the mechanical behavior of rocks are coupled.

In the laboratory experiments, hydrated bentonite pellets were mixed with barite and HEC to make the mud used in the tests. Additionally, tests were made on barite after the process of sagging. The materials were poured into a 4.1 cm ID PVC pipe. Sand was also poured into the pipe, making its own column on top of mud, this prevent mud from being blown out of pipe while water is being pumped into the pipe through one end.
Mud was found to undergo a process of drainage (compression) when water was being injected into pipe. Channels of injected water were passing apparently between mud column and inner pipe wall ending into sand column. A link between mud compression/drainage and the forming of channels has been established, by use of hose clamps to restrict pipe expansion, i.e. mud expansion and thus drainage. The effect of use of clamps was registered in decreasing mud drainage for same pressures, and retarding the creation of channels.

Drainage of bentonite mud in a mechanical compressor prior to water injection into pipe proved in an increase in deformation undergone by mud compared with undrained mud for the same pressures. Use of clamps for the case of drained mud caused a drop in the magnitude of deformation undergone by mud compared with the case of no clamps.

An auxiliary material, laponite, has been used to give provide a window into what happens inside of the mud during the process of drainage and the creation of channels. This was possible due to the transparent property of laponite.

Extensive laboratory testing does not provide evidences that suggest displacement of fluids inside of bentonite by the forces of capillarity. It suggests rather that transporting mechanism of fluids inside of bentonite mud is mainly attributed to the hydromechanical behavior of the material. This was arrived to with help of laponite gel.

In a special outfitted Oedometer, hydrated bentonite was being constantly compacted for a period of time. At the end of two weeks, with a sample height of 13 mm and a radius of 34.95 mm, water was then injected, while sample was constantly under compressive force, into the Oedometer. The compressive piston force applied constantly on bentonite sample on one side and water injection pressure from the other side created an increasing differential pressure inside of the compacted bentonite. The sample successfully managed for the duration of test, 35 hours, to prevent water from displacing through it. The last hours of test, the piston delivered a force equal to 100 bars on top of the sample, while under the sample, the pump was delivering a water injection pressure of 100 bars!

Further work is suggested to be carried out on the Oedometer that could also be used to conduct extra and more comprehensive testing on bentonite, like investigating the additional effect of heat on the sealing properties of the material.

TABLE OF CONTENTS

PREFACE I

SUMMARY II

LIST OF FIGURES VII

1. INTRODUCTION 1

2. BENTONITE AS PLUGGING MATERIAL: REVIEW OF FIELD EXPERIENCES 2

3. FLUID TRANSPORT IN POROUS MEDIA 8

4. POROELASTICITY 11

4.1 HYDROSTATIC POROELASTICITY 12
4.2 UNDRAINED COMPRESSION 19
4.3 BIOT'S POROELASTIC THEORY 22
4.4 EFFECTIVE STRESS CONCEPT 27
4.5 THE SKEMPTON COEFFICIENTS 29

5. FAILURE MECHANICS AND HYDRAULIC FRACTURING 30

5.1 ROCK STRENGTH CONCEPT 30
5.2 THE FAILURE SURFACE 33
5.3 EFFECT OF CONFINING STRESS 34
5.4 EFFECT OF PORE FLUIDS 35
5.5 HYDRAULIC FRACTURING 37

6. LABORATORY INVESTIGATION 40

6.1 TEST EQUIPMENT AND EXPERIMENTAL SETUPS 40
6.1.1 THE MAIN EXPERIMENTAL SETUP 40
6.1.2 THE ALTERNATIVE EXPERIMENTAL SETUP 42
6.2 TEST MATERIALS 46
6.3 EXPERIMENTS PROCEDURES 48
6.3.1 THE MAIN PROCEDURE 48
6.3.2 THE ALTERNATIVE PROCEDURE 51

7. RESULTS AND DISCUSSION 53

7.1 THE UNCLAMPED PIPE TEST 55
7.2 THE CLAMPED PIPE TEST 58
7.3 DRAINED MUD TEST WITH NO CLAMPS ATTACHED 59
7.4 DRAINED MUD TEST WITH ATTACHED CLAMPS 61
7.5 EXPERIMENTING ON LAPONITE GEL 63
7.6 EXPERIMENTING ON BARITE 66
7.7 EXPERIMENTING ON HYDRATED AND COMPACTED BENTONITE 67
7.8 THEORY APPLICATION 72
7.9 METHODS AND LIMITATIONS 74
7.10 FURTHER WORK 75

8. CONCLUSION 76

9. REFERENCES 78

APPENDIX A 83

A-1 83
SATURATION 83
1. FLOW OF IMMISCIBLE FLUIDS 84
1.1 INTERFACIAL TENSION AND CAPILLARY PRESSURE 85
1.1.1 SATURATION 85
1.1.2 INTERFACIAL TENSION AND WETTABILITY 85
1.1.3 CAPILLARY PRESSURE 88
1.2 SATURATION AND CAPILLARY PRESSURE 91
1.2.1 THRESHOLD PRESSURE AND SATURATION DISTRIBUTION 91
1.2.2 HYSTERESIS – IMBIBITION VS. DRAINAGE 94
1.3 PERMEABILITY 96
1.3.1 THE KLINKENBERG EFFECT 97
1.3.2 RELATIVE PERMEABILITY 98

A-2 101

RHEOLOGICAL CLASSIFICATION OF FLUIDS 101

A-3 105

MAXWELL–BETTI RECIPROCAL THEOREM 105

APPENDIX B 106

DATA SHEET FOR BENTONITE PELLETS 106

APPENDIX C **107**

LAPONITE MANUFACTURER DATA SHEET **107**

LIST OF FIGURES

Figure 2.1: Property comparison of cement to bentonite [1]……2

Figure 2.2: Hydration of compressed sodium bentonite nodules (Zonite) [2]……..3

Figure 2.3: Abandonment case schematics considered by task force [1]……4

Figure 2.4: Coalinga pilot abandonment results [1]……6

Figure 2.5: Time and Cost Estimates for Cement and Sodium Bentonite (Zonite) [3]…….6

Figure 3.1: Conventional Capillary Pressure Curve vs. Water Saturation characteristic curve after van Genuchten–Mualem. Modified from [6]……..9

Figure 3.2: Characteristics of typical relative permeability for a two phase flow, where water is the wetting phase(left) and oil is the wetting phase(right) [8]……10

Figure 4.1: Generic porous rock showing a) the bulk volume, pore volume, mineral/matrix volume, and b) the pore pressure and confining pressure [9]……..13

Figure 4.2: Pore strain (a) and pore compressibility (b) of a Frio sandstone from East Texas, measured at zero pore pressure [24]……..14

Figure 4.3: Illustration of the superposition concept used in deriving relationships between the various porous rock compressibilities. [9]……16

Figure 4.4: Undrained bulk compressibility of Fort Union sandstone, as a function of the pore fluid compressibility [32 & 33]. If the pore fluid is a mixture of water and air at atmospheric pressure, the symbols show the three cases of 0%, 99% and 100% water saturation……21

Figure 4.5: a) “Jacketed” and b) “unjacketed” test situations [35]… ……24

Figure 5.1: Typical specimen for uniaxial stress versus deformation in a uniaxial compression test. Typical diameter is 38 mm. [modified from 35]……..30

Figure 5.2: Principle sketch of stress versus deformation in a uniaxial compression test. In practice, the ductile region may be very small [35]……..31

Figure 5.3: Triaxial testing: typical influence of the confining pressure
on the shape of the differential stress (axial stress minus confining pressure)
versus axial strain curves. [35]……32

Figure 5.4: Schematic picture of a failure surface in principal stress space.
The dash–dot line represents the hydrostatic axis. Note that the
conventional relation $\sigma_1' \geq \sigma_2' \geq \sigma_3'$ has been abandoned in this figure,
in order to illustrate that the failure surface is closed: The rock is supposed
to fail at some stress level, for any ratios between the principal stresses. [35]……34

Figure 5.5: Stress-strain curves for *different* rocks at various confining pressures.
Crosses indicate abrupt brittle failure [9]……35

Figure 5.6: A stress state that lies below the failure curve. (b) Application of
a pore pressure causes the effective stress state to move closer to the failure curve. [9]……36

Figure 5.7: Vertical fracture around a vertical well [35]……37

Figure 5.8: Hydraulic fracturing of a porous and permeable rock [35]……38

Figure 6.1: Experimental setup for the pipe containing bentonite mud and sand.
During normal procedure, the hole in the outlet cap was kept open the whole time……41

Figure 6.2: Ruska pump used to inject colored water into pipe filled with
bentonite and sand……41

Figure 6.3: Schematic illustration of the main experimental setup……42

Figure 6.4: The Basic setup of Oedometer cell. Wave transducer were
not needed for our purpose and never used (written in red). One of
the two lower drainage channels was connected to Quisix pump and
used to inject water into sample holder, while the other bottom drainage
channel was closed. The two upper drainage channels were kept open all the time……43

Figure 6.5: Schematic illustration of the main chamber……44

Figure 6.6: Load frame to the left and Quisix pump and
its operating computer to the right……45

Figure 6.7: Compaction and stress data acquisition setup for Oedometer test……46

Figure 6.8: Sample of bentonite pellets and laponite powder top,
bentonite mud (lower left) and laponite gel (lower right)……47

Figure 6.9: Hydrated bentonite pellets after 72 hours (left).
The result of mixing described in point 2 and point 1 (right)…… 48

Figure 6.10: Top view (left) and bottom view (right) of the caps used for the PVC pipe with the injection inlet in the center of the cap……49

Figure 6.11: The Main Experimental Setup. Colored water, blue, is feed to the pump, which injects it into the pipe far to the left while continuously monitoring the pressure in the mud column with a pressure meter (left to the center in the picture)……50

Figure 7.0: Mud invading sand column at pressures above 15 bars. Note, pressure in the sand column is atmospheric……53

Figure 7.1: Forming of water zone. Here at 6.5 [bars]……54

Figure 7.2: Incremental water volume at increased pressures. Here at 13 [bars]……54

Figure 7.3: Blue water beams escaping the water zone into mud column at high pressures (left), similar behavior was found for the case of laponite gel, but at higher pressures……55

Figure 7.4: injection flow for different pressure ranges for mud in a pipe with unrestrained expansion. Note the magnitude of the decreasing trend of flow from start to end……57

Figure 7.5: Progression of water beams along inner pipe wall at increasing injection pressures……58

Figure 7.6: Hose clamps used to restrain the PVC pipe expansion……58

Figure 7.7: Injection flow for different pressure ranges for the case of mud in the pipe with restrained and unrestrained expansion. Notice the difference in magnitude of flow and the overall stable fluctuation in flow rate for clamped pipe compared to unclamped pipe……59

Figure 7.8: The mud inside pipe in a mechanical compressor. Notice the water draining from bentonite mud and into sand filter at both ends of the pipe……60

Figure 7.9: Injection flow for different pressure ranges for the case of mechanically drained mud with unrestrained expansion [Light blue line]. Notice the huge difference in flow rates at start and end of pressure scale……61

Figure 7.10: Injection flow for different pressure ranges for the case of mechanically drained mud with restrained expansion [Light green line]. The smooth and subtle changes in flow rates for the light green line remind us of the orange line……62

Figure 7.11: Propagation of water beam in Laponite gel. It starts vertically right upward limiting itself to a thin film moving in the area between gel and inner pipe wall, then changes the course and propagates radially into gel……64

Figure 7.12: Water propagating into gel at increasing pressures from Figure (7.11). Progression starts from top left to bottom right. Notice the different planes water is propagating through the gel at……..65

Figure 7.13: Water, blue, transporting through sagged barite in PVC pipe. Notice that water is not initially transporting between barite column and inner pipe wall, but rather right through it… ……67

Figure 7.14: The sample, at the end of testing. The upper left picture shows the sample as it was in the holder, the damages seen on the picture upper right comes solely from the operation of getting the sample out of its holder. Notice the bright green color. No traces of blue water going through it, as confirmed by no water production from the drainage channels during the whole injection period (32 hours)……68

Figure 7.15: The Cumulative water injected for the duration of the test, 32 hours. During the first few minutes, pump was started and water run through pipe to remove air from piping prior to injection into sample holder. The injection process starts from 240 ml and onward……69

Figure 7.16: Output pressure from the pump delivering constant pressure. The stepping effect observed is the process where injection pressure and net piston force were equalizing and then more dead weight was being placed on lever thus increasing net piston force. After this was done, injection pressure from pump was then increased and same process repeated all the way until 10 MPa. The line heading straight down at end of injection was when the pump was stopped and test terminated……70

Figure 7.17: Figure shows Compaction of for the very first hours of Bentonite compaction. The Vertical axis has been calibrated to show actual compaction in [mm]. The three different lines are combined to give an overall average of the compaction undergone by sample in three different directions. Compaction here has been converted to indicate positive values. Note, the figure is for the case of pure compaction, no water has been injected so far……71

Figure 7.18: reaction of compacted bentonite sample caught in between piston force stress on one side and injection pressures on the other. Compaction is negative. Notice the declining trend at start of the lines due to increase in piston force. The compaction levels out and further increase in piston force is applied; inducing further compaction. The small decrees in negative values in the middle of the figure are due to increase of injection pressure……72

1. INTRODUCTION

With the maturation experienced in the petroleum industry, many wells are at the end of their lifetime and these will need to be plugged and abandoned in the near future. From 2011-2040 it is estimated that around 2000 wells need to be abandoned, while 150 new wells will be drilled each year [49]. Plug and Abandonment operations are expensive and can contribute up to 25% of the total drilling costs of exploration wells [50]. Need for more research and alternative plugging materials that could help bring down the costs of the overall process of abandoning a well.

Traditionally, cement has always been used as the material of choice for sealing of both primary cementing of casing and when the well need to be permanently plugged and abandoned at the end of its lifetime. But cement has problems related to shrinkage while setting, creation of micro annuli and channeling. Cement is also brittle and can crack, making pathways for hydrocarbons to escape in events of subsurface movements such as earthquakes, salt swell or compaction/subsidence. If a plastic material such as bentonite, which swells and expands during hydration, was used, it has the ability to reshape itself to the surrounding and heal any cracks which may occur.

Bentonite has been used as a plugging material in monitoring wells, mining shafts, seismic shot holes and water wells. It has also been suggested to plug high level nuclear waste deposits [1].

The main objective of the thesis remains to be an investigation on how bentonite pellets and or barite materials can be used for plugging of boreholes. The materials have been tested each by itself and when mixed together. This will be presented in the course of the next chapters.

2. BENTONITE AS PLUGGING MATERIAL: REVIEW OF FIELD EXPERIENCES

The basic technologies associated with the plugging and abandoning of wells has not changed significantly since the 1970s. Water-based slurries of cement and drilling mud are still the basic materials used to plug most wells although progress has been made in use of additives to customize the cements and muds for specific types of wells.

The maturation of the oil and gas industry around the world has resulted in a large number of idle and orphaned wells. At the 1999 SPE Environment Forum in Breckenridge, Colorado, the number one environmental, health and safety issue was the ever-increasing number of wells waiting to be abandoned, the increasing number of orphan wells and the lack of funding to significantly reduce the liabilities.

In an effort to address idle and poorly abandoned wells, Chevron Environmental Management Company, formed a task force to search for reliable and cost effective means of well abandoning technology. [1]

In this search, the ideal alternative plugging material was defined as a compressed sodium bentonite nodule with a rounded shape and a specific density greater than 2.0. After reaching its intended depth in a well, the material would form an impermeable, geologically sound barrier. Additionally, the latent hydration characteristics of the dense, plastic material would continue to conform to its environmental as the formation around it changed. Sodium bentonite has been utilized to plug monitoring wells, mining shafts, seismic shot holes, water wells and occasionally oil and gas wells and suggested for use in plugging high level nuclear waste deposits due to its ability to confine waste migration in groundwater and resist alteration with time.

	Cement	**Sodium Bentonite**
Chemical	65% CaO 22% SiO_2 13% Other	63% SiO_2 21% $A1_2O_3$ 16% Other
Physical		
• Sp. Gravity	3.14-3.16	2.5-2.8
• Surf. Area (cm^2/g)	2500-4000	80000
• Bulk density ($g/cm^{3)}$	1.506	2.05-2.2 (1.75 g/cm^3 when hydrated
• Permeability (md)	10^{-1} - 10^{-3} md	10^{-2}-10^{-7}md
• Swelling	0.05-0.30%	10-25 times (unconfirmed)
Mechanical		
Swelling pressure (psi)	-0	1450-2900
Compressive strength (psi)	500-4000	174-369

FIGURE 2.1: PROPERTY COMPARISON OF CEMENT TO BENTONITE [1]

Figure (2.1) shows a comparison of the physical and chemical characteristics of sodium bentonite with cement the most commonly used plugging material for oil and gas wells. While bentonites and clays are considered superior confinement materials due to their extremely low permeability, their utilization in the oil and gas industry has been problematic

due to issues related to proper placement of material. The most common forms of sodium bentonite are flake (raw) or processed extruded pellets.

Historically, bentonite has been placed at depth with by means of several methods: 1) Pumped as a viscous pill; 2) Dropped with cardboard tube; 3) Placed with dump bailer; 4) In combination with cement; 5) Gravity fed; and 6) Pumped down in a diesel plug. The material's hydration capability and rapid swelling characteristics (10-25 times) presented bridging issues for placement at depth in all of the methods. [1]

The bridging issue was solved by compressing bentonite in powder form into bentonite nodules; this would slow down the hydration process and allow bentonite to reach designated depth. Figure (2.2) shows compressed bentonite nodules left to hydrate for 24 hours in a 6 inch plastic tube.

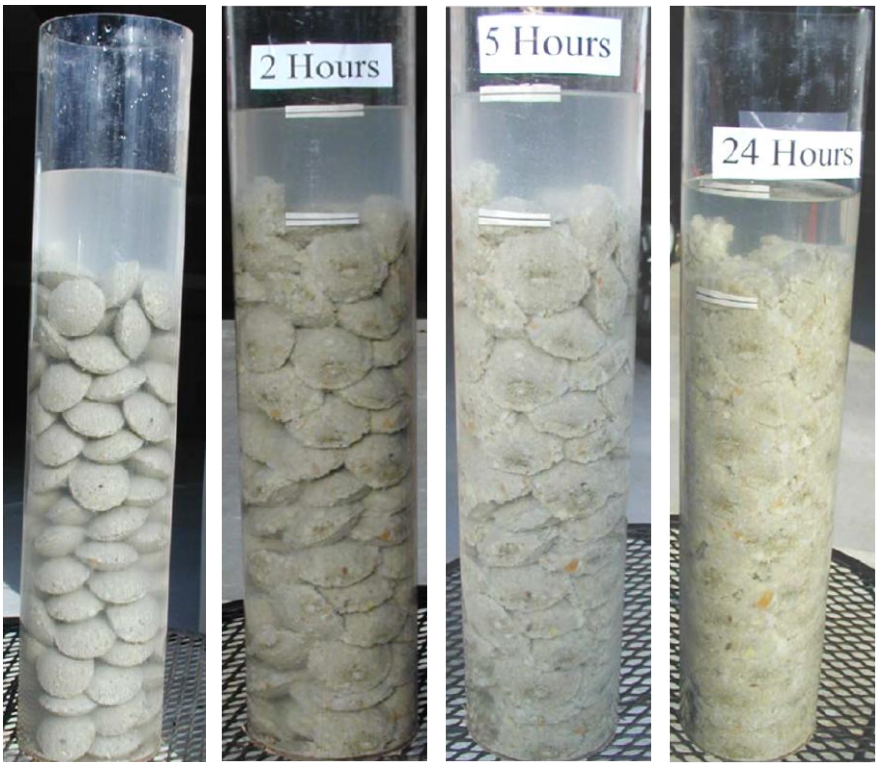

FIGURE 2.2: HYDRATION OF COMPRESSED SODIUM BENTONITE NODULES (ZONITE) [2]

A series of test were conducted on the compressed sodium bentonite nodules to fine the boundary limits [1]

- → Nodules were placed in a glass container and covered with freshwater, seawater (20 000mg/l) or saturated sodium chloride brine (189 000mg/l). In all cases the nodules had formed a hydraulically solid plug after 12 hours. Some flaking was observed for the case of seawater and brine.
- → Nodules were hydrated in freshwater and afterwards submerged in saturated seawater for 60 days; no deterioration or shrinkage of the plug was observed.

- → Nodules were placed in a plastic container with holes in the bottom; water was run continuously through the container, after 3 hours, the bentonite hydrated sufficiently to stop the flow of water.
- → Nodules were dropped into a glass container with oily produced water with a fresh oil layer thicker than one nodule, 12 hours later the nodules had formed a hydraulically solid plug.
- → A glass container with nodules was heated to boiling point, after 2 hours the flow paths for steams had been sealed due to hydration.
- → Nodules were submerged in saturated hydrogen sulfide water and hydrated to 70% of what was seen in fresh water.
- → At a different location, a 100 feet long bentonite plug was pressure tested for 1500 psi (103 bars); long term stability was also confirmed over a 9 months period.

Three generalized abandonment designs were considered. These are described in Figure (2.3). The task force proposed the abandonment of nineteen wells in Coalinga, California, including several from each case of the three generalized abandonment designs. It was also desired that the well population be as diverse as possible within a single oil field. Primary producers, water flood producers and injectors, cyclic stream wells, and steam flood producers were included in the pilot.

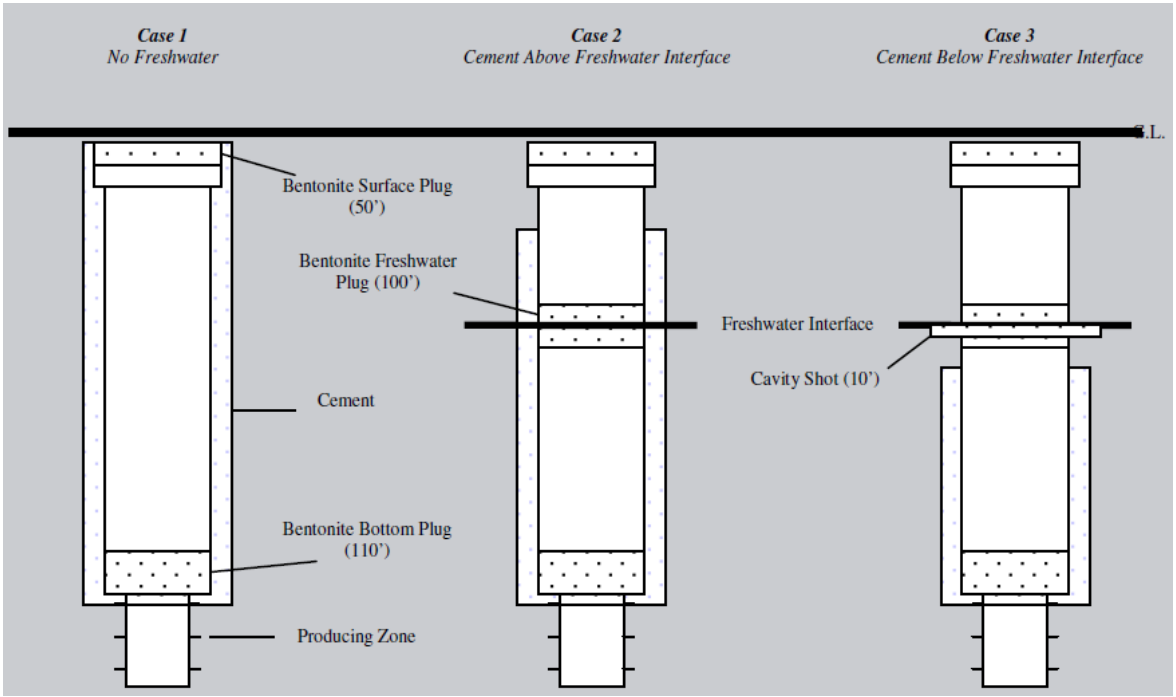

FIGURE 2.3: ABANDONMENT CASE SCHEMATICS CONSIDERED BY TASK FORCE [1]

- → Eleven of the nineteen wells were of case 1. In these wells, a 110 ft. plug was placed at top of the perforations to isolate the producing zone, in combination with a 50 ft. surface plug.
- → Four of the wells were of case 2. The wells in this case had a freshwater zone. In addition to the two set of plugs used in case 1, the freshwater zone in this case needed to be isolated by a 100 ft. across the interface.

→ The remaining four wells were of case 3. This case is identical to case 2 except that there is no cement behind the casing at the freshwater zone. This normally requires a cavity shot and using cement, but the task force had approval to use bentonite to fill the cavity and wellbore after firing a cavity shot.

Gravel was used to fill the wellbore between bentonite plugs in order to create a base for the plugs. Here a bridge plug instead of gravel could have been used as well. This was done for all the nineteen wells. Bentonite plugs were verified by a slickline tag after pouring [1].

Several procedures of related to filling the well with water or even hot water before adding gravel and bentonite were tried. The air-liquid interface was typically 1000 ft. deep. The nodules performed well when poured dry and penetrated the air-liquid interface without bridging; falling at last through the liquid column to designated depth. The gravel used, pea gravel and ¾''-minus gravel, tended to bridge while free falling down to the air-liquid interface. It was therefore decided follow a procedure of filling up the wellbore with hot water before adding gravel and this action eliminated the problems related to gravel bridging. [1]

Following the procedure of filling up borehole with hot water before adding bentonite to plug the producing zone led unfortunately to an early bridging of bentonite for three wells. It was only then the effect of heat on hydration of bentonite was fully understood at the field level. This was the first occasion in which the bentonite had not fallen to its intended depth without incident. Prior use of hot water in the first ten wells was used after placing bentonite and before pouring gravel. Now, hot water was constantly being added to the well with no opportunity for downhole cooling to occur prior to the addition of bentonite.

The operational dilemma faced now was the need for hot water to assist in viscosity reduction for the gravels' sake, and the need for cool water to ensure effective placement of bentonite. The solution obtained was to allow the bentonite to free-fall as much as possible in the wellbore to reduce settling time and achieve a high confidence level of reaching its objective depth. Once there, and verified with a slickline tag, hot water could be trickled into the well while gravel was poured. The water then served to hydrate the bentonite and prevent gravel bridges. As a further means of optimization, the trickling of the hot water into the well was stopped prior to the end of the gravel stage. This served to cool the water before the introduction of bentonite. This modified placement technique proved to be efficient and as a result abandonment time was reduced. [1]

A list over the nineteen wells abandoned in the Coalinga field test can be seen in Figure (2.4). Costs saving by using of sodium bentonite compared to cement was estimated to 20-40% due to no need for pump trucks, coiled tubing and bulk units. [1]

WELL	WELL TYPE	CASE	TD	TOP PERF	INITIAL FLUID L.	TOP BOT. PLUG	"A" PT FLUID L.	TOP "A" PT PLUG	FRESH WATER FLUID L.	T/FRESH WATER PLUG	SURF. FLUID L.	TOP SURF. PLUG	ABAN TIME (hrs)	DOGGR APPROVAL
60-11A	PRODUCER	1	2680	2360	1297	2240	NA	NA	NA	NA	480	10	12.5	Yes
2-8-11A	PRODUCER	1	1660	1449	-	1196	NA	NA	NA	NA	504	9	15.5	Yes
3-7-11A	PRODUCER	1	1880	1166	482	1465	NA	NA	NA	NA	-	10	7	Yes
146-11A	PRODUCER	1	1800	1604	1400	1462	NA	NA	NA	NA	-	8	11	Yes
45-11A	PRODUCER	1	1600	1503	1460	1407	NA	NA	NA	NA	355	11	6.5	Yes
243-11A	PRODUCER	1	1800	1617	1455	1487	NA	NA	NA	NA	at surface	3	6	Yes
138-11A	PRODUCER	1	1622	1432	1270	1281	NA	NA	NA	NA	-	8	4.5	Yes
AMITY 9-3-1D	CYCLIC	1	973	447	355	342	NA	NA	NA	NA	at surface	11	4.5	Yes
8-4A-1D	CYCLIC	1	605	162	50	1	NA	NA	NA	NA	at surface	NA	4	Yes
2-8-25D	CYCLIC	1	1130	885	720	529	NA	NA	NA	NA	at surface	9	7	Yes
2-7-25D	CYCLIC	1	1150	1006	720	810	NA	NA	NA	NA	at surface	1	5	Yes
2-9-7C	CYCLIC	2	1820	1500	1320	1372	1091	1091	at surface	232	at surface	9	6.5	Yes
1-7-19C	CYCLIC	2	1900	1642	-	1554	1303	1303	at surface	352	at surface	11	7	Yes
4-8-7C	PRODUCER	2	1800	1673	700	1573	1237	1237	at surface	399	at surface	10	7	Yes
4-7-7C	PRODUCER	2	1810	1681	280	1558	1147	1147	at surface	355	-	10	19.5	Yes
4-7-17C	WATER INJ	3	3405	3278	380	3141	2322	2322	98	1041	-	1	27.5	Yes
3-6-17C	WATER INJ	3	3270	3152	350	2985	2316	2316	at surface	1117	at surface	13	7.5	Yes
ARICA 6-6-7C	PRODUCER	3	2095	1984	-	1850	1468	1468	106	507	at surface	8	10	Yes
ARICA 5-6-7C	PRODUCER	3	1965	1842	480	1763	1382	1382	at surface	567	-	8	28	Yes

*all depths in feet from ground level

FIGURE 2.4: COALINGA PILOT ABANDONMENT RESULTS [1]

In another SPE (Society of Petroleum Engineers) paper, ChevronTexaco Australia reported plugging of its first well outside USA with compressed bentonite nodules. The well was located at the barrow island oil field in Australia which is classified as nature reserve, and environmental factors are therefore especially important. The aim was to reduce the abandonment costs by 50% compared to using cement, Figure (2.5).

	Cement		Zonite	
	Time (hrs)	Cost ($000)	Time (hrs)	Cost ($000)
MIRU, well control	12	2.5	12	2.5
Running bridge plug	6	2.5	6	2.5
Deep cement plug	6	7.5	/	
Waiting on cement	6	2.5	/	
Pour Zonite	/		4	1
Shallow Zonite retainer	/		1	1
Shallow cement plug	6	7.5	/	
Waiting on cement	6	2.5	/	
Pour Zonite	/		4	1
Surface casing cement	6	5	6	2.5
Wellhead removal	6	2.5	6	2.5
Contingency	6	2.5	4	1
SUB TOTAL	60	35	44	14
Supervision	48	2.5	12	2.5
GRAND TOTAL	**60**	**37.5**	**39**	**16.5**

FIGURE 2.5: TIME AND COST ESTIMATES FOR CEMENT AND SODIUM BENTONITE (ZONITE) [3]

In order to avoid swelling problems, the selected wells for the case of Barrow Island, was circulated to freshwater before plugging started, a bridge plug was set 10 meters below the perforations to act as a fundament for the plug. A 210 ft. long compressed sodium bentonite plug was set at 2800 ft. TVD (True Vertical Depth) in about 5 hours by surface pouring. Plug was tagged and allowed to hydrate for 28 days before it was pressure tested up to 500 psi (34 bars). The abandonment was a success and it was decided to monitor the pressure in the well for months to prove long term stability of the plug.

In addition to the cost saving benefits of using bentonite, other benefits related to health, safety and environment such as small operational footprint, no cementing chemicals or additives, no well site spills and better integrity due to plasticity of the mentioned plug.

3. FLUID TRANSPORT IN POROUS MEDIA

This chapter attempts to give a brief presentation of the concepts related to the flow through porous medium domain. Special attention has been given certain aspects of transport in porous media this is due to the laboratory work leading up to this thesis. For further details about the various definitions and figures used in this chapter, the reader is referred to Appendix A-1.

There are two types of flow possible when two or more fluids in motion occupy a porous medium [4]. These are:

- Miscible displacement
  In this case the two fluids are completely soluble in each other and the interfacial tension between the two fluids is zero. In other words, a distinct fluid-fluid interface does not exist.

- Immiscible displacement
  In this case we have a simultaneous flow of two or more fluids or phases, e.g., oil, water and gas, in the porous medium domain. The interfacial tension between the fluids is non-zero, and a distinct fluid-fluid interface separates the fluids within each pore [5].

When two immiscible fluids are in contact, a discontinuity in pressure or interfacial tension exists between the two fluids, which depend upon the curvature of the interface separating the fluids. This curvature is a result of the stronger adhesive force of the wetting fluid: an axisymmetric meniscus develops, convex towards the wetting fluid, and the angle of the meniscus contact to the solid's surface is the wetting (contact) angle, θ. The pressure difference along the discontinuity described is called the capillary pressure. In other words, capillary pressure is per definition the difference between pressure in the non-wetting phase and that found in the wetting phase. That is, the pressure excess in the non-wetting fluid is the capillary pressure, and this quantity is a function of saturation and is affected by among others temperature.

As hydrocarbons migrate into a reservoir trap, the non-wetting fluids (oil or gas) enter the pore space initially occupied by the wetting fluid (water). For the non-wetting phase to displace the wetting phase, some driving force, or pressure differential is required to overcome the threshold capillary pressure, also known as entry pressure. This force is equivalent to the minimum injection pressure. In the case of oil, the droplets initially retarted by the threshold pressure P_c – amalgamate with other arriving droplets into progressively longer filaments, until their increased buoyancy allows them to displace the water and eventually move to the top of the reservoir Figure (3.1). Gas has due to its very low density and viscosity, has much less problem with overcoming the threshold pressure

and migrates easily ahead of oil. The displacement process in this manner is thus a matter of drainage and imbibition of the different phases.

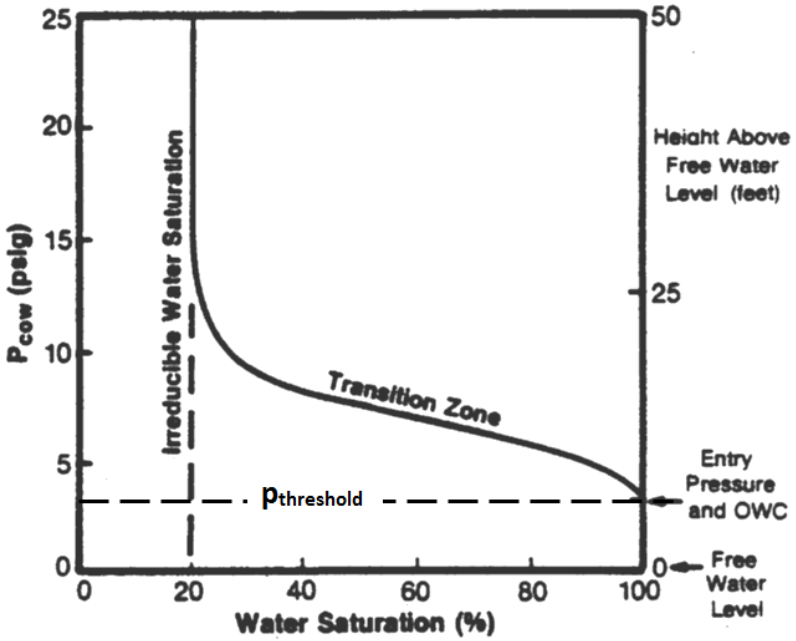

FIGURE 3.1: CONVENTIONAL CAPILLARY PRESSURE CURVE VS. WATER SATURATION CHARACTERISTIC CURVE AFTER VAN GENUCHTEN–MUALEM. MODIFIED FROM [6]

According to Leverett [7], the dynamic behavior of a system in which two fluids are flowing simultaneously is best described in terms of its "effective permeability" to either phase. Relative permeability is a concept used to relate the absolute permeability, 100% saturation of one fluid, of a porous system, to the effective permeability of a particular fluid in the system, when this particular fluid only occupies a fraction of the total pore volume. Since the effective permeability is always less than the absolute permeability, the relative permeability lies between 0 and 1, and the sum of relative permeabilities for all phases in the same medium is less than the absolute permeability. The relationship between relative permeability and wettability for a two phase flow (oil and water) and (gas and water) is shown in Figure (3.2)

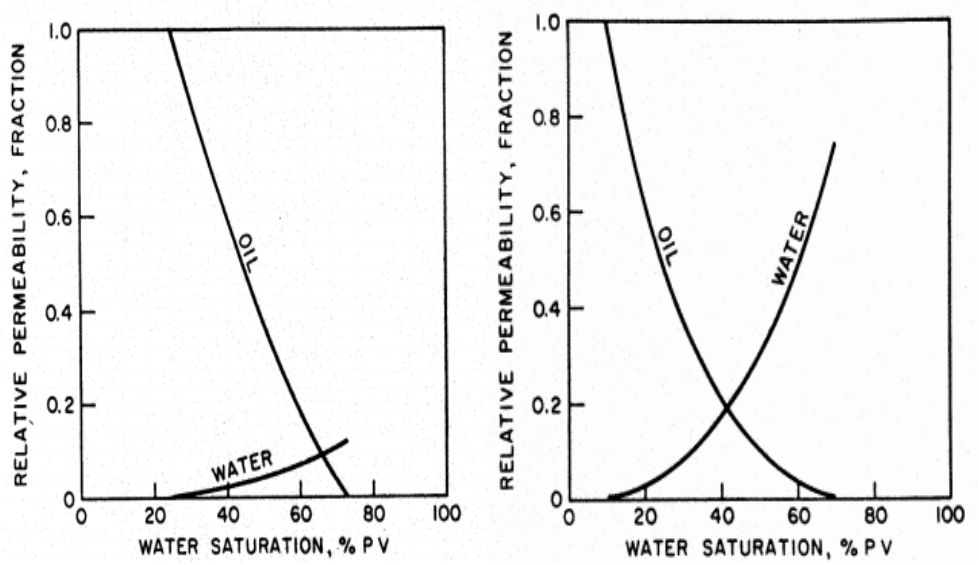

FIGURE 3.2: CHARACTERISTICS OF TYPICAL RELATIVE PERMEABILITY FOR A TWO PHASE FLOW, WHERE WATER IS THE WETTING PHASE(LEFT) AND OIL IS THE WETTING PHASE(RIGHT) [8]

4. POROELASTICITY

Subsurface rocks are, by their nature, filled with cracks and pores that are saturated with one or several fluids which play a major influence on the mechanical behavior of a rock mass. If such a rock were under compression, pore fluid pressure would cause the state of stress to move closer to the failure surface in a Mohr circle. In addition pore fluid pressures give rise to macroscopic elastic deformation of the rock. The mechanical deformation of a rock is therefore coupled to the pore fluid pressure. Pore fluids flow through the rock in response to gradients in the pore pressure, but can also flow due to changes in the macroscopic stresses due to natural causes such as tectonic forces, and man-made causes such as the drilling of boreholes, etc. Hence, the mechanical behavior and hydrological behavior of rocks are fully coupled, although most analyses of rock mechanics problems, and subsurface flow problems, ignore this coupling [9]. The assumption of a completely rigid porous rock mass is the corner rock in the majority of the work conducted on subsurface flow problems in hydrology, petroleum engineering and geophysics, is further stated by the authors. Similarly, most rock mechanics analyses either ignore pore fluid effects or assume that the pore pressures can be found independently of the mechanical deformation. Although such assumptions are often acceptable, there are many situations in which the coupling between deformation and pore fluid pressure and fluid flow must be accounted for. For example, effects of pore pressure play an important role in the deformation around a borehole [10], hydraulic fracturing of boreholes, and slip along active faults [11].

The general theory that accounts for this coupled hydromechanical behavior is called *poroelasticity***.** The theory was chiefly put forth by Biot [12], and developed further by, among others Detournay and Cheng [13].

In the next sub chapters, a theory of poroelasticity for hydrostatic loading is presented, chapter 4.1 and 4.2. Although this theory is limited to account only the isotropic loading, the hydrostatic case can be developed in a fully nonlinear form. Despite the development of several nonlinear theories of nonhydrostatic poroelasticity, most poroelastic analyses utilize the linearized “Biot” theory. This theory, which accounts for deviatoric stresses as well as hydrostatic stresses and pore fluid pressures, is presented in sub chapter 4.3. According to Jaeger et al [9], Rock mass deformation is also influenced by thermal effects. In fact, the theory of thermoelasticity can be developed along lines that are entirely analogous to poroelasticity, with the temperature playing the role of the pore pressure, etc. [14]. One difference between the two theories stems from the fact that in most situations thermomechanical coupling is unilateral, in the sense that the temperature field has an effect on the mechanical deformation, but the stresses and strains have a negligible effect on the temperature [15]. On the other hand, the coupling in poroelasticity between mechanical deformation and pore pressures generally cannot be ignored [16 & 17).

Accounting for the thermoelastical influences on the deformation of a rock is beyond the scope of this thesis.

Throughout this chapter, additional expressions have been gone through this in an effort to better illustrate the effect the various element in the theory of poroelasticity has on the different properties of rock.

4.1 HYDROSTATIC POROELASTICITY

Theories for the poroelastic behavior of rocks can be developed on the basis of two conceptual models of porous rock: a solid material containing an interconnected collection of voids or pores [18 & 19] or an aggregation of grains in partial contact with each other at various points [20 & 21]. Anagnostopoulos [22] reported that the latter model is more appropriate for soils, whereas the former has proven to be more fruitful for studying rocks. There is no clear demarcation between these two types of geological media, and the behavior of poorly consolidated sedimentary rocks is in many ways similar to that of some soils. However, a theory of poroelasticity that applies to most rock-like materials can be constructed by starting with the *idealization* of a rock as a connected porous mineral phase. These pores may be interconnected, or may exist as isolated vugs; the latter do not contribute to the fluid flow processes, and for the present purposes can be ignored. [9]

Due to the nature of this thesis, the theory of poroelasticity has been narrowed to the special case of hydrostatic loading. To develop this theory, consider a porous rock, as shown in Figure (4.1a). The macroscopic ‘’bulk” volume of the rock is V_b, the volume occupied by the pore space is V_p, and the volume occupied by the solid mineral component is V_s where:

$$V_b = V_s + V_p \tag{4.1}$$

The mineral phase of the rock is often referred to in poroelasticity as the “matrix or solid”. The relative amounts of void space and solid component can be quantified either by the porosity, ϕ, which is defined by

$$\phi = \frac{V_p}{V_b} \tag{4.2}$$

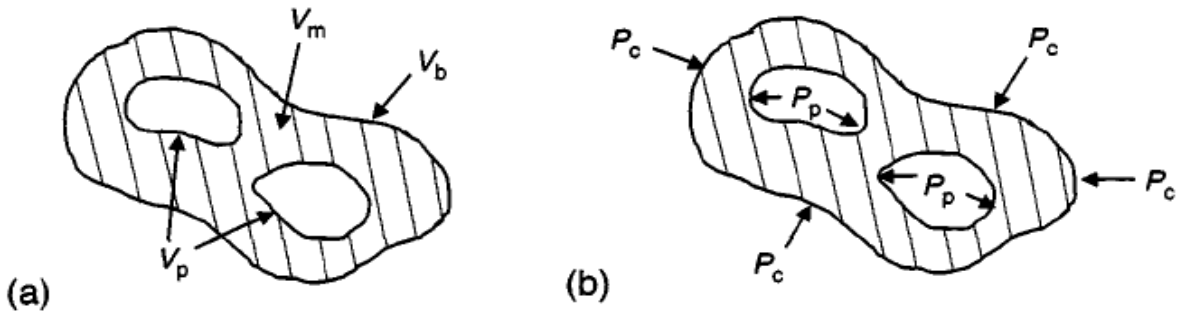

FIGURE 4.1: GENERIC POROUS ROCK SHOWING A) THE BULK VOLUME, PORE VOLUME, MINERAL/MATRIX VOLUME, AND B) THE PORE PRESSURE AND CONFINING PRESSURE [9]

Or by the void ratio, *e*, defined as

$$e = \frac{V_p}{V_s} = \frac{\phi}{1-\phi} \tag{4.3}$$

The porosity is restricted, by definition, to the range $0 \leq \phi < 1$**,** whereas the void ratio can take on any positive value.

Now imagine that a purely normal traction of magnitude p_c is externally applied onto this piece of porous rock, where the subscript *c* denotes "confining" pressure, and the internal pore walls are subjected to a pore pressure of magnitude p_p, exerted by the pore fluid, Figure (4.1b). As a pore fluid cannot sustain a shear stress under static conditions, no shear traction can be transmitted to the pore walls. There are two independent pressures that may act on the rock and two independent volumes (taken here to be V_b and V_p), so four compressibilities can be defined [23]:

$$c_{bc} = \frac{-1}{V_b^i}\left(\frac{\partial V_b}{\partial p_c}\right)_{p_p} = \frac{1}{K_{fr}}\ ,\ c_{bp} = \frac{-1}{V_b^i}\left(\frac{\partial V_b}{\partial p_p}\right)_{p_c} = \frac{\alpha}{K_{fr}} \tag{4.4}$$

$$c_{pc} = \frac{-1}{V_p^i}\left(\frac{\partial V_p}{\partial p_c}\right)_{p_p} = \frac{1}{K_p}\ ,\ c_{pp} = \frac{-1}{V_p^i}\left(\frac{\partial V_p}{\partial p_p}\right)_{p_c} \tag{4.5}$$

where the superscript *i* denotes the initial, unstressed state and K_p (defined as $K_p = \frac{\phi}{\alpha} K_{fr}$) and K_{fr} are the bulk modulus for the pore volumetric strain and frame modulus respectively. One can look at c_{bc} and c_{pc} as "compression" as they pack the matrix and decrease the bulk volume thus are positive stress by definition, while c_{bp} and c_{pp} are "decompression or expansion" as they oppose the confining stresses and contributes to increase the bulk volume and therefore negative per definition. The symbol α represents a dimensionless effective stress coefficient which will be defined in the next section. Increments in the bulk and pore strain can be expressed in terms of the porous rock compressibilities as follows:

$$\Delta\varepsilon_b = -\frac{\Delta V_b}{V_b^i} = c_{bc}\Delta p_c - c_{bp}\Delta p_p \qquad (4.6a)$$

Alternatively, we can write equation (4.6a) as follows:

$$-\frac{\Delta V_b}{V_b^{\,i}} = \frac{1}{(1-\phi)K_s}\left(\sigma_p - \phi p_f\right) \qquad (4.6b)$$

Where p_f is the pore fluid pressure, K_s is the solid bulk modulus, σ_p is the confining stress or pressure.

$$\Delta\varepsilon_p = \frac{-\Delta V_p}{V_p^i} = c_{pc}\Delta p_c - c_{pp}\Delta p_p \qquad (4.7a)$$

Alternatively, the above equation can be written in an alternative way in order to put it in context:

$$-\frac{\Delta V_p}{V_p^{\,i}} = \frac{1}{\phi}\left(\frac{1}{K_{fr}} - \frac{1}{K_s}\right)\sigma_p - \frac{1}{\phi}\left(\frac{1}{K_{fr}} - \frac{1+\phi}{K_s}\right)p_f \quad , \quad K_{fr} = K_s(1-\frac{\phi}{\phi_c}) \qquad (4.7b)$$

Where K_{fr} denotes the framework bulk modulus and ϕ_c is the critical porosity, which is the maximum porosity above which the grains in the solid material will no longer be in contact with each other and the frame moduli will vanish. Hence, K_{fr}, is by definition always smaller than K_s.

Here a decrease in the volume is considered to be a positive strain. The bulk strain expressed in equation (4.6) is equivalent to the macroscopic volumetric strain defined as:

$$\varepsilon_{vol} = \varepsilon_x + \varepsilon_y + \varepsilon_z \qquad (4.8)$$

As shown in Figure (4.2), the four porous rock compressibilities expressed in equations (4.4) and (4.5) are typically stress-dependent: decreasing with increasing stress and leveling off to constant values at confining pressures that are on the order of 50 MPa (1 MPa = 145 psi).

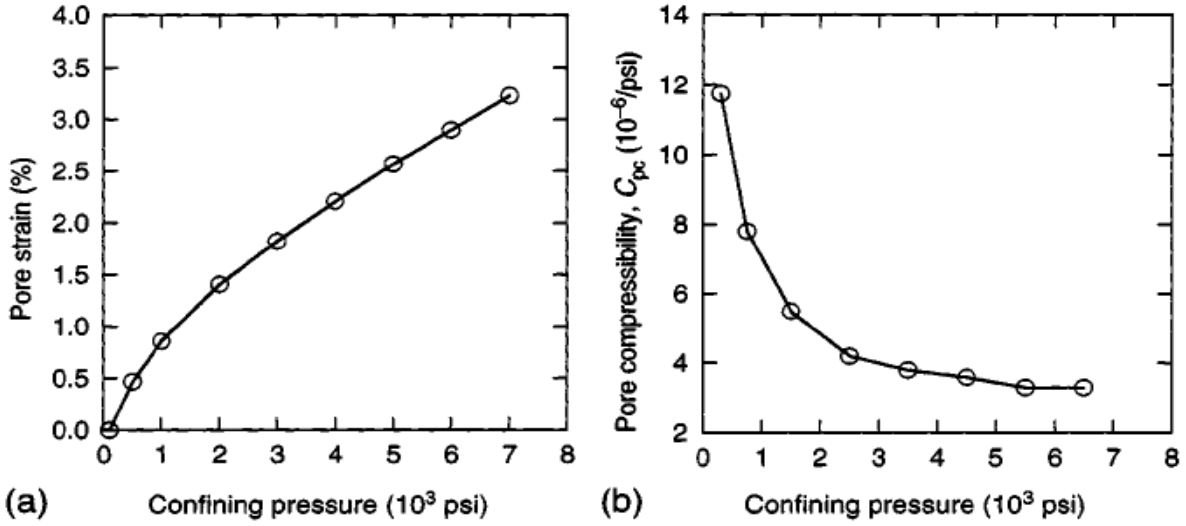

FIGURE 4.2: PORE STRAIN (A) AND PORE COMPRESSIBILITY (B) OF A FRIO SANDSTONE FROM EAST TEXAS, MEASURED AT ZERO PORE PRESSURE [24]

The figure shows the pore strain vs. confining stress for a Frio sandstone from East Texas, measured with the pore pressure held constant at 0 MPa. At low pressures, the curve is quite nonlinear, but becomes linear at pressures above 40 MPa (5800 psi). Figure (4.2b), shows the decreasing influence of higher confining pressures on compressibility c_{pc}.

In the following derivation, all applied pressures and their resulting strains will be *incremental* changes superimposed on an already-existing state of stress and strain. The loading state consisting of a uniform hydrostatic stress (i.e., normal traction) of magnitude Δp_c applied over the entire outer surface of the porous rock and uniform hydrostatic pressure of magnitude Δp_p applied over the entire interior pore surface, will be denoted by $\{\Delta p_c, \Delta p_p\}$**.** If a stress increment $\{\Delta p, \Delta p\}$ is applied to the surface of the body, meaning $\Delta p_p = \Delta p_c = \Delta p$ the resulting incremental stress state in the rock is that of uniform hydrostatic stress of magnitude Δp throughout the matrix [19]. This can be verified by noting that uniform hydrostatic stress of magnitude Δp satisfies the stress equilibrium equations, because the divergence of a spatially uniform tensor is identically zero, and also satisfies the boundary conditions on both the outer and inner surfaces of the matrix. This stress state leads to a uniform isotropic dilatation of magnitude

$$\varepsilon_m = \frac{\Delta p}{K_m} = c_m \cdot \Delta p \qquad (4.9)$$

where c_m and K_m are the compressibility and bulk modulus of the rock matrix material respectively. But this state of stress and strain within the matrix is exactly the same as that which would occur if the pores were hypothetically filled up with matrix material, and the boundary conditions on the outer surface were left unchanged. In this latter case, the total bulk strain is equal to:

$$\varepsilon_b = c_m \cdot \Delta p \tag{4.10}$$

so the bulk volume change is given by

$$\Delta V_b = -c_m \cdot V_b^i \cdot \Delta p \tag{4.11}$$

Now consider the stress increment {Δp, 0}, which corresponds to a change in the confining pressure, while pore pressure is held constant. By definition, this will give rise to a change in the bulk volume given by

$$\Delta V_b = -c_{bp} \cdot V_b^i \cdot \Delta p \tag{4.12}$$

Similarly, a stress increment of {0, Δp}, would give rise to a bulk volume change of

$$\Delta V_b = -c_{bc} \cdot V_b^i \cdot \Delta p \tag{4.13}$$

For the infinitesimal changes under consideration, the principle of superposition is valid, so the stress increment {0, Δp}, which means constant confining pressure with variable pore pressure, can be separated into the difference of the two increments {Δp, Δp}, and**,** {Δp, 0}, as illustrated in Figure (4.3). The strains resulting from the stress increment {0, Δp} will therefore be equal to the difference between the strains that result from the stress increments {Δp, Δp} and {Δp, 0}. Using the notation $\Delta V_b(\Delta p_c,\ \Delta p_p)$ to refer to the bulk volume change resulting from the stress increment $\{\Delta p_c,\ \Delta p_p\}$, we have

$$\Delta V_b(0,\ \Delta p_p) = \Delta V_b(\Delta p,\ \Delta p) - \Delta V_b(\Delta p,\ 0) \tag{4.14}$$

$$c_{bp} \cdot V_b^i \cdot \Delta p = -c_m \cdot V_b^i \cdot \Delta p + c_{bc} \cdot V_b^i \cdot \Delta p \tag{4.15}$$

Hece,

$$c_{bp} = c_{bc} - c_m \tag{4.16}$$

The first term to the left is the bulk compressibility when confining pressure is held constant while pore pressure variable, the second term is for the case where the pressure variations for pore and confining pressure are equal, the last term to right is for the case where pore pressure is held constant and confining pressure variable. The following analogous relation between the two pore compressibilities can be derived in a similar manner:

$$c_{pp} = c_{pc} - c_m \tag{4.17}$$

By applying the Maxwell-Betti reciprocal theorem, Appendix (A-3), to the two sets of loads {Δp, 0) and (0, Δp}, the pore compressibilities and the bulk compressibilities can be related to each other. This relationship deepens our understanding of the poroelastic theory, especially when considering hydraulic fracturing, as we will get back to later.

The work that would be done by the first set of loads acting through the displacements due to the second set is given by:

$$W^{12} = -\Delta p\left[\Delta V_b\left(0,\Delta p\right)\right] = -\Delta p\left[c_{bp}V_b^i\Delta p\right] = -c_{bp}\cdot V_b^i\cdot\left(\Delta p\right)^2 \quad (4.18)$$

where the minus sign accounts for the fact that the confining pressure acts in the –n direction, where n is the outward unit normal vector to the external surface,

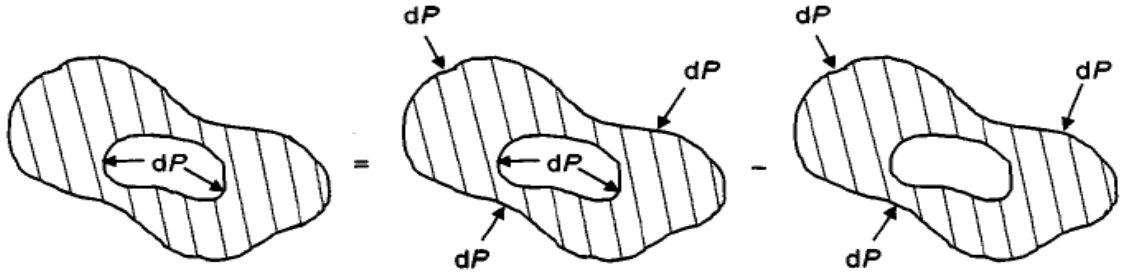

FIGURE 4.3: ILLUSTRATION OF THE SUPERPOSITION CONCEPT USED IN DERIVING RELATIONSHIPS BETWEEN THE VARIOUS POROUS ROCK COMPRESSIBILITIES. [9]

whereas the bulk volume would increase if the displacement were in the +n direction. Similarly,

$$W^{21} = \Delta p\left[\Delta V_p\left(\Delta p,0\right)\right] = \Delta p\left[-c_{pc}\cdot V_p^i\cdot\Delta p\right] = -c_{pc}\cdot V_p^i\cdot\left(\Delta p\right)^2 \quad (4.19)$$

No minus sign is needed in the defining equation for W^{21}, because the pore pressure acts in the same direction as that of increasing pore volume. The reciprocal theorem implies that $W^{12} = W^{21}$ and so comparison of equations (4.18) and (4.19) reveals that ($c_{bp}V_b^i = c_{pc}V_p^i$). But $V_p^i = \phi^i V_b^i$, and so

$$c_{bp} = \phi^i c_{pc} \quad (4.20)$$

This relation requires for its validity only the assumption of elastic behavior; it does not require that the matrix be either homogeneous or isotropic [9]. Equations (4.16), (4.17) and (4.20) provide three relations between the four compressibilities (c_{bc}, c_{bp}, c_{pc} and c_{pp}) with ϕ^i and c_m as the only other parameters explicitly involved. In terms of ($c_{bc,}$ c_m and ϕ^i) the other three compressibilities are:

$$c_{bp} = c_{bc} - c_m \quad (4.21)$$

$$c_{pc} = \frac{\left(c_{bc} - c_m\right)}{\phi^i} \quad (4.22)$$

$$c_{pp} = \frac{\left(c_{bc} - \left(1+\phi^i\right)c_m\right)}{\phi^i} \tag{4.23}$$

The approximate validity of Equations (4.21-4.23) has been demonstrated for several consolidated sandstones [23]. It follows from (4.21-4.23) that bulk compressibility as a volumetrically weighted average of the pore and matrix compressibilities no longer have validity, as has occasionally been supposed [25].

Physically, the stress dependence of the compressibilities is due to the closure of cracks, seating of grain contacts, or other processes that involve the closure of thin, crack-like voids, and pore pressure has essentially an equal, but, opposite effect on the deformation of a thin void as does the confining pressure. Hence, porous rock compressibilities, varying with P_c and P_p, depend only on the *differential pressure* defined as $\Delta p = p_c - p_p$. The dependence of the compressibilities on the differential stress is also a necessary condition in order for the volumetric strain to be independent of the path taken in stress space [9]. Indeed, applying the Euler condition for exactness of a differential to the bulk strain increment gives:

$$\frac{\partial^2 \varepsilon_b}{\partial p_p \partial p_c} = \frac{\partial}{\partial p_p}\left(\frac{\partial \varepsilon_b}{\partial p_c}\right) = \frac{\partial c_{bc}}{\partial p_p} \tag{4.24}$$

$$\frac{\partial^2 \varepsilon_b}{\partial p_c \partial p_p} = \frac{\partial}{\partial p_c}\left(\frac{\partial \varepsilon_b}{\partial p_p}\right) = \frac{-\partial c_{bc}}{\partial p_c} = \frac{-\partial\left(c_{bc} - c_m\right)}{\partial p_c} = \frac{-\partial c_{bc}}{\partial p_c} \tag{4.25}$$

As c_m can be taken to be a constant, due to marginal changes in compressibilities of rock forming minerals [26], we can equate the two above equations and show that c_{bc} satisfies the partial differential equation $\frac{\partial c_{bc}}{\partial p_c} = -\frac{\partial c_{bc}}{\partial p_p}$ the general solution to which is $c_{bc}\left(p_c, p_p\right) = f\left(p_c - p_p\right)$, where *f* is any function that depends on the two pressures only through the combination $(p_c - p_p)$. Equations (4.21 - 4.23), then show that the other three porous rock compressibilities also *depend only* on the *differential pressure*.

Some key simplifications have been considered in treatment of hydrostatic poroelasticity [27]. One of which the assumption that the volumetric strain in the matrix is negligible compared to the pore strain bringing us to equations that can be derived from Equations (4.21 - 4.23), by setting c_m equal to zero. The two pore compressibilities are then *equal* to each other, as are the two bulk compressibilities. The assumption loses its validity as we move from soils and unconsolidated sands to more consolidated sandstones and hard rocks [28].

The assumption that the rock forming mineral phase effectively behaves like an isotropic elastic medium can be tested experimentally through so-called “unjacketed tests,” in which the rock is pressurized by a fluid which is allowed to seep into its pores, resulting in equal

pore pressure and confining pressure [9]. If p_p equals p_c, then equation (4.6) and (4.7) give a bulk strain as follow:

$$\varepsilon_b = c_{bc} p_c - c_{bp} p_c = p_c \left(c_{bc} - c_{bp} \right) = c_m \cdot p_c \tag{4.26}$$

In an unjacketed test, the stress-dependence disappears, and the rock deforms as a linear elastic medium with compressibility c_m [29].

The overall strain of a fluid-filled porous elastic solid is not governed by the Terzaghi effective stress law. It has been shown [30], in the context of anisotropic linear elasticity, that the overall strain may be resolved into a component which is the average strain of the solid matrix and a component due to change in relative pore geometry, and that the latter is determined by the Terzaghi effective stress. A theory of hydrostatic poroelasticity in terms of ϕ and Vm could therefore be developed [30]. Using the identities Vm = Vb - Vp and ϕ = Vp/Vb, along with equations (4.21- 4.23), it follows that the porosity and matrix volume are governed by:

$$\Delta\phi = -\left[\left(1 - \phi^i \right) c_{bc} - c_m \right] \left(p_c - p_p \right) \tag{4.27}$$

$$\varepsilon_m = \frac{c_m}{\left(1 - \phi^i \right)} \left(p_c - \phi^i p_p \right) \tag{4.28}$$

One interpretation of equation (4.28) is that the average stress, $\overline{\sigma}_m$, in the mineral phase is given by:

$$\overline{\sigma}_m = \frac{p_c - \phi^i p_p}{1 - \phi^i} \tag{4.29}$$

This result is actually true in general and does not require that the matrix be isotropic, homogeneous, or elastic [31].

4.2 Undrained Compression

In the previous section, equations were developed and discussed and it is important to note that these equations were only appropriate for processes in which the pore pressure and confining pressure vary independently; which is the case when we produce from the reservoir leading to a reduction in pore pressure.

Now we will take on other processes where the two pressures, pore and confining, are not independent. For example, during drilling, the *in situ* stresses will be altered in the vicinity of the borehole. This will create changes in the pore volume within a certain region

surrounding the borehole, which will initially lead to a change in the pore pressure. If the rock is highly permeable, pore fluid will almost instantly flow in such a manner as to reestablish pore pressure equilibrium with the adjacent regions of rock. For a rock that is relatively impermeable, such as shale, the time required for pore pressure equilibrium to be reestablished may be very large, so for a certain period of time, the pore fluid must be considered as being "trapped" inside the stressed region near the borehole [9].

When a fluid-saturated porous rock undergoes deformation, it is in an undrained manner to start with and gradually, after the pore pressure has had sufficient time to re-equilibrate itself, in a drained manner. An analysis of the limiting case of completely undrained compression can be conducted by beginning with the expressions for the bulk and pore strains given by Equations (4.6) and (4.7). If the pore space is completely saturated with a fluid that is "trapped," then the pore strain is also equal to the strain undergone by the pore fluid, that is:

$$\varepsilon_p = \varepsilon_f = - c_f p_p \tag{4.30}$$

If the confining pressure is changed, then Equations (4.30), (4.7) and (4.6) form a set of three unknowns {ε_b, ε_p, p_p}. Solution of these equations yields the following expression for the *undrained bulk compressibility*:

$$c_{bu} = \left(\frac{\varepsilon_b}{p_c} \right)_{undrained} = c_{bc} - \frac{c_{bp}\, c_{pc}}{c_{pp} + c_f} \tag{4.31}$$

Considering the overall bulk compressibility of a porous rock system, the undrained bulk compressibility is *less* than the drained bulk compressibility, due to the additional stiffness that the trapped pore fluid imparts to the system. This expression for undrained bulk compressibility is independent of any assumption concerning the microstructure and stress-strain behavior of the matrix. If the matrix is assumed to be elastic, then the use of equation (4.20) allows equation (4.31) to be written as:

$$c_{bu} = \left(\frac{\varepsilon_b}{p_c} \right)_{undrained} = \frac{\phi^i c_{bc} \left(c_f - c_\phi \right) + c_m \left(c_{bc} - c_m \right)}{\phi^i \left(c_f - c_\phi \right) + \left(c_{bc} - c_m \right)} \tag{4.32}$$

If the rock matrix is homogenous, then $c_\phi = c_m$, and the undrained bulk compressibility would be given by [20]:

$$c_{bu} = \left(\frac{\varepsilon_b}{p_c} \right)_{undrained} = \frac{\phi^i c_{bc} \left(c_f - c_m \right) + c_m \left(c_{bc} - c_m \right)}{\phi^i \left(c_f - c_m \right) + \left(c_{bc} - c_m \right)} \tag{4.33a}$$

As seen from above, the undrained bulk compressibility is an increasing function of the fluid compressibility, *all* other parameters being constant. The variation of c_{bu} with c_f, for the Fort

Union sandstone is shown in Figure (4.4) [32]. The sandstone had a porosity of 0.085, a matrix compressibility of c_m = 0.286 x 10^{-4}/MPa, a drained bulk compressibility of c_{bc} = 1.31 x 10^{-4}/MPa, and a pore compressibility of c_{pp} = 11.8 x 10^{-4}/MPa. If the pores were filled with air at atmospheric pressure, which has a compressibility of c_f = 9.87/MPa, then the undrained bulk compressibility would equal (to three significant figures) the drained value, 1.3 1 x 10^{-4}/MPa. If the rock was saturated with water, which has a compressibility of c_f = 5.0 x 10^{-4}/MPa, the undrained bulk compressibility would be 0.573 x 10^{-4}/MPa. A hypothetical "incompressible" pore fluid, on

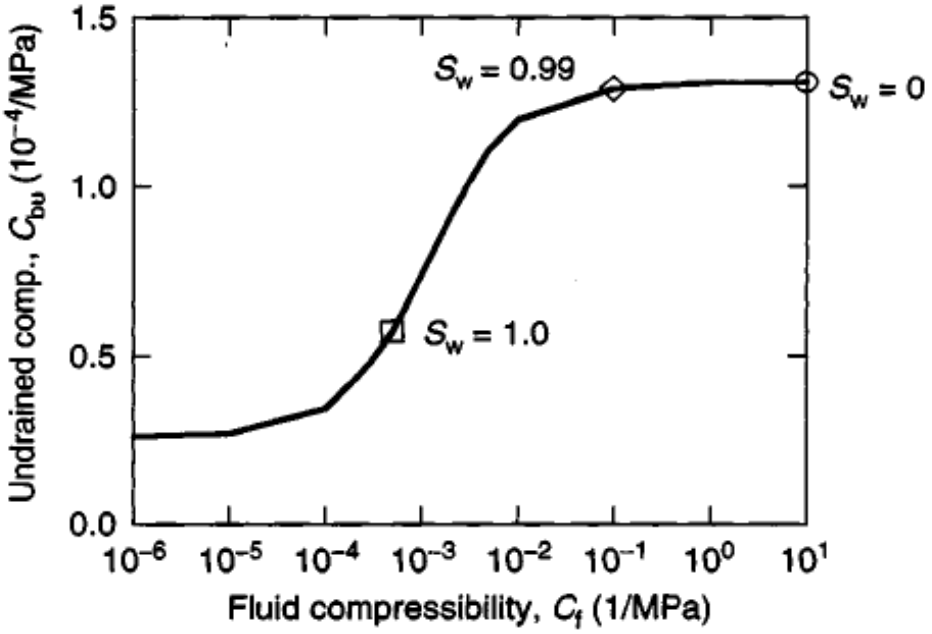

FIGURE 4.4: UNDRAINED BULK COMPRESSIBILITY OF FORT UNION SANDSTONE, AS A FUNCTION OF THE PORE FLUID COMPRESSIBILITY [32 & 33]. IF THE PORE FLUID IS A MIXTURE OF WATER AND AIR AT ATMOSPHERIC PRESSURE, THE SYMBOLS SHOW THE THREE CASES OF 0%, 99% AND 100% WATER SATURATION.

A hypothetical "incompressible" pore fluid, on the other hand, would lead to an undrained compressibility of 0.261 x 10^{-4}/MPa. Hence, the assumption that water is incompressible, which is acceptable in many engineering situations, would yield a grossly incorrect value for the undrained bulk compressibility [33].

Parallel to the definition of undrained compressibility expressed in equation (4.33a), undrained pore compressibility can also be found from equations (4.30), (4.7) and (4.6):

$$c_{pu} = \left(\frac{\partial \varepsilon_b}{dp_c} \right)_{undrained} = \frac{c_{pc} c_f}{c_{pp} - c_f} = \frac{c_{pc}}{1 + \frac{c_{pp}}{c_f}} \qquad (4.33b)$$

As seen from the equation above, the presence of trapped pore fluid therefore causes the compressibility of the pore space with respect to the confining pressure to decrease, which means that the overall bulk compressibility of the system is lower than otherwise.

4.3 Biot's Poroelastic Theory

In the previous section, we have touched several aspects of Biot's theory of poroelasticity. In this section, the theory is presented as a whole in order to further elicit the dependence of the bulk material coefficients to the micromechanical ones. This is done at the cost of more measurements which in turn give us additional insight to the interaction among the constituents [35].

We assume a linear elastic behavior between the stresses applied and the strain or deformation it is met by in the material, which consequently has the assumption of being micro-homogeneous. Let us consider an isotropic, porous and permeable medium, consisting of two components: a solid and a fluid part. The displacement or deformation of the solid is denoted $\vec{u}_s$ while that of the fluid is denoted $\vec{u}_f$. For a volume element attached to the solid, the strains are given as the derivatives of the components of $\vec{u}_s$.

$$\varepsilon_{vol} = \nabla \cdot \vec{u}_s \tag{4.34}$$

For the fluid part, we will define a strain parameter ζ , which describes the volumetric deformation of the fluid relative to that of the solid:

$$\zeta = \phi \nabla \cdot \left(\vec{u}_s - \vec{u}_f \right) \tag{4.35}$$

The stress tensor $\ddot{\sigma}$ represents the total external stress on a volume element attached to the solid framework. The volume element compensates for this stress partly by stresses in the solid framework, and partly by a hydrostatic pressure in the fluid, pore pressure p_f. In accordance with the sign convention, all stresses—including the pore pressure—are positive in compression. Fluid mass changes in a volume element attached to the solid can be subdivided into two parts: the change of the pore volume (due to change in the external stresses and/or the pore pressure), and the compression/decompression of the fluid as the pore pressure changes. This means that we may write

$$\zeta = -\phi \left(\frac{\Delta V_p}{V_p} + \frac{p_f}{K_f} \right) \tag{4.36}$$

The present pore fluid will add extra terms to the strain energy of the material. Linear stress–strain relations for this two-phase system can be expressed in terms of the strain parameters ε_{vol} and ζ , the stress tensor elements and the pore pressure p_f [34]:

$$\sigma_x = \lambda\varepsilon_{vol} + 2G\varepsilon_x - C\zeta \quad (4.37)$$

$$\sigma_y = \lambda\varepsilon_{vol} + 2G\varepsilon_y - C\zeta \quad (4.38)$$

$$\sigma_z = \lambda\varepsilon_{vol} + 2G\varepsilon_z - C\zeta \quad (4.39)$$

$$\tau_{xy} = 2G\gamma_{xy} \quad (4.40)$$

$$\tau_{xz} = 2G\gamma_{xz} \quad (4.41)$$

$$\tau_{yz} = 2G\gamma_{yz} \quad (4.42)$$

$$p_f = C\varepsilon_{vol} - M\zeta \quad (4.43)$$

Written in a compact form, the following notation is introduced:

$$\sigma_{ij} = \lambda\varepsilon_{vol}\delta_{ij} + 2G\varepsilon_{ij} - C\,\zeta\,\delta_{ij} \quad (4.44)$$

Where δ_{ij} is known as the Kronecker symbol, λ and G are Lamé parameters of the porous material. C and M are additional elastic moduli required to describe a two-phase medium. Since we are especially interested in the case of an *undrained* hydrostatic, based on our experiments, (here meaning tri-axial) compression of the porous material special attention will be dedicated to this case in this section as well.

By letting ζ = 0 in equation (4.44) means that there is no fluid movement in the material, i.e. the material is *undrained*. Thus the λ in equation (4.44) is not the λ of the dry porous medium, but the λ of the fluid-filled medium when the fluid is trapped. To get some understanding of the physical meaning of M in equation (4.43), we may let ε_{vol} = 0 and substitute equation (4.35) into equation (4.34) we then find [35]:

$$p_f = M\phi\nabla\cdot\vec{u}_f \quad (4.45)$$

which shows that M ϕ is a measure of how much the pore pressure increases as the amount of fluid in a volume element is increased. If the solid was completely rigid, we would thus have M ϕ = K_f. Explicit expressions for C and M in terms of the solid and fluid moduli are given later. Summation of equations (4.37 - 4.39) gives:

$$\overline{\sigma} = K\varepsilon_{vol} - C\zeta \quad (4.46)$$

where $\overline{\sigma} = (\sigma_x + \sigma_y + \sigma_z)/3$. $K = \lambda + 2G/3$ is the bulk modulus of porous rock in undrained condition. In order to get a good understanding of the relationship between elastic moduli C,

M and K and the moduli of constituents of the rock a jacketed *drained* test is required: a porous medium is confined within an impermeable jacket, and subjected to an external hydrostatic pressure, p_c or σ_p, Figure (4.5a).

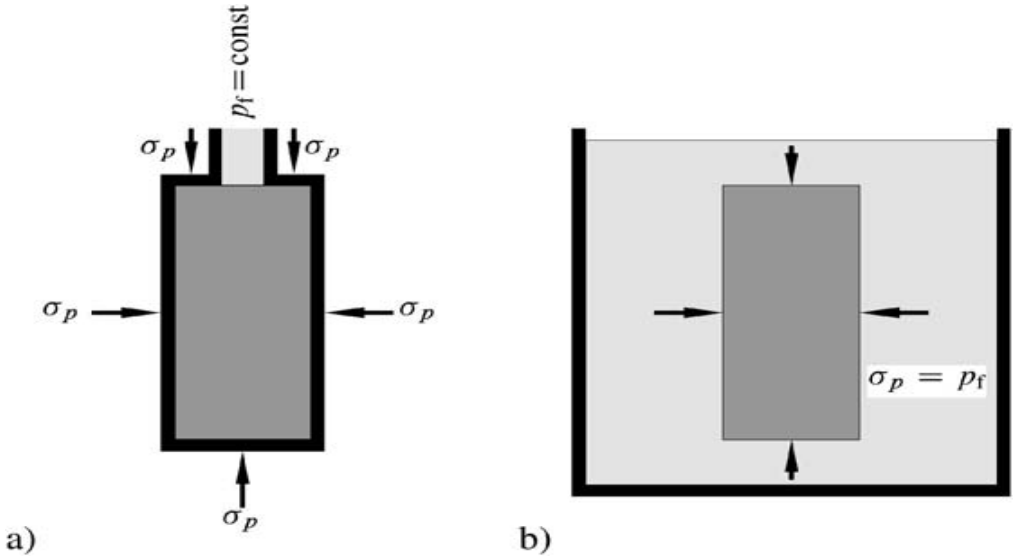

FIGURE 4.5: A) "JACKETED" AND B) "UNJACKETED" TEST SITUATIONS [35]

The pore fluid is allowed to escape during loading, so that the pore pressure is kept constant, and hence the stress is entirely carried by the solid framework. From equations (4.43) and (4.46), we then obtain:

$$\frac{\sigma_p}{\varepsilon_{vol}} = K - \frac{C^2}{M} \overset{def}{=} K_{fr} \tag{4.47}$$

Where K_{fr} is the frame modulus. We now proceed to the "unjacketed" test illustrated in Figure (4.5b). The rock sample under investigation is here embedded in a fluid in such a way that the hydrostatic (i.e. confining) pressure on the sample is equilibrated by the pressure in the pores [35], i.e. $p_f = \sigma_p$. Combining equations (4.43) and (4.46) we find:

$$\frac{\sigma_p}{\varepsilon_{vol}} = \frac{p_f}{\varepsilon_{vol}} = \frac{K_{fr}}{1 - \frac{C}{M}} \tag{4.48}$$

The loading $p_f = \sigma_p$ means that there is a uniform stress within the sample, which means that the framework deforms uniformly assumed of course microscopic homogeneity in rock constituent. Thus the volumetric strain of the total sample, the pore volume and the solid (grain) volume must be equal [35]:

$$\frac{\Delta V_{tot}}{V_{tot}} = \frac{\Delta V_p}{V_p} = \frac{\Delta V_s}{V_s} \tag{4.49}$$

From $p_f = \sigma_p = -K_s(\Delta V_s/V_s)$ where K_s is the bulk modulus of solid grain, (the relationship between K_s and K_{fr} is previously defined under equation (4.7) expressed in terms of porosity), we hence find:

$$\frac{\Delta V_s}{V_s} = \frac{\Delta V_p}{V_p} = \frac{\Delta V_{tot}}{V_{tot}} = -\varepsilon_{vol} = -\frac{p_f}{K_s} \tag{4.50}$$

The stress-strain response is therefore entirely given by the intrinsic elastic properties of the solid material. By comparing equations (4.48) and (4.50) we can relate K_s and K_{fr} in terms of C and M as follows:

$$K_s = \frac{K_{fr}}{1-\frac{C}{M}} \tag{4.51}$$

From equations (4.36) and (4.50) it follows that:

$$\zeta = \phi\left(\frac{1}{K_s} - \frac{1}{K_f}\right)p_f \tag{4.52}$$

On the other hand, the combination of equations (4.43) and (4.46) with $p_f = \sigma_p$ gives

$$\zeta = \frac{C-K}{MK-C^2}\,p_f \tag{4.53}$$

Combining equations (4.52) and (4.53) we obtain the relation:

$$\phi\left(\frac{1}{K_s} - \frac{1}{K_f}\right) = \frac{C-K}{MK-C^2} \tag{4.54}$$

Although this equation was derived for a specific loading, unjacketed test, it is generally valid. [35]

Having the equations (4.51) and (4.54) combined with the definition of K_{fr} in equation (4.47), allows us to express the elastic constants K, C and M in terms of the elastic moduli of the constituents of the rock (K_s and K_f), plus the porosity ϕ and the framework modulus K_{fr}. The results are:

$$K = K_{fr} + \frac{K_f}{\phi}\frac{\left(1-\frac{K_{fr}}{K_s}\right)^2}{1+\frac{K_f}{\phi K_s}\left(1-\phi-\frac{K_{fr}}{K_s}\right)} \tag{4.55}$$

$$M = \frac{K_f}{\phi}\frac{1}{1+\frac{K_f}{\phi K_s}\left(1-\phi-\frac{K_{fr}}{K_s}\right)} \tag{4.56}$$

$$C = \left(1 - \frac{K_{fr}}{K_s}\right) M = \frac{K_f}{\phi} \frac{\left(1 - \frac{K_{fr}}{K_s}\right)}{1 + \frac{K_f}{\phi K_s}\left(1 - \phi - \frac{K_{fr}}{K_s}\right)} \tag{4.57}$$

Equation (4.55) is called Biot-Gassmann equation and may alternatively be written as:

$$\frac{K}{K_s - K} = \frac{K_{fr}}{K_s - K_{fr}} + \frac{1}{\phi}\frac{K_f}{K_s - K_f} \tag{4.58}$$

The above relations do not give clear physical meaning to parameter and we therefore look into a couple of limit cases in order to get a better insight.

One case is a "hard" rock, where the frame is incompressible compared to the fluid it contains in its pores. As $K_s \gg K_f$ in general, we have for this "stiff frame" case:

$$K_{fr}, K_s \gg K_f \tag{4.59}$$

For porosities that are not too small (specifically $\phi \gg (K_f / K_s^2)(K_s - K_{fr})$), Equations (4.55-4.57) then reduce to:

$$\text{"Stiff frame"} \quad \begin{cases} K \approx K_{\mathrm{fr}} \\ C \approx \frac{K_{\mathrm{f}}}{\phi}\left(1 - \frac{K_{\mathrm{fr}}}{K_{\mathrm{s}}}\right) \\ M \approx \frac{K_{\mathrm{f}}}{\phi} \end{cases} \tag{4.60}$$

We notice that bulk modulus K is here identified as the bulk modulus of the rock framework, while the constant M is entirely given by the properties of the pore fluid and the pore system [35].

The opposite limit is that of a "weak frame". For this case we assume

$$K_{fr}, K_s \ll K_f \tag{4.61}$$

For porosities $\phi \gg (K_f / K_s)$, equations (4.55-4.57) reduce to:

$$\text{"Weak frame"} \quad \begin{cases} K \approx K_{\mathrm{fr}} + \frac{K_{\mathrm{f}}}{\phi} \\ C \approx M \approx \frac{K_{\mathrm{f}}}{\phi} \end{cases} \tag{4.62}$$

In this case, the bulk modulus K is influenced not only by the rock stiffness, but also by the fluid bulk modulus K_f. In the limiting case when $K_{fr} \rightarrow 0$ (suspension of the solid grains) $K = C = M \approx K_f/\phi$ are all given mainly by fluid properties.

4.4 EFFECTIVE STRESS CONCEPT

In the previous section we discussed the case of "jacketing" a rock sample while the pore fluid was allowed to escape, drained test, Figure (4.5a). The stress-strain response in the rock was given by equation (4.47), i.e.

$$\sigma_p = \varepsilon_{vol} K_{fr} \tag{4.63}$$

Doing the same test but in undrained case, the compression of the sample including the pore space, due to external hydrostatic load, will in this case cause an increase in the pore pressure, as previously mentioned. The sample compression and pore pressure can be calculated by requiring ζ = 0 in equations (4.43) and (4.46), i.e. no relative displacement between pore fluid and the solid during the test. Pore pressure is then given by equation (4.43):

$$p_f = C\varepsilon_{vol} \tag{4.64}$$

While the stress-strain characteristics are given by equation (4.46):

$$\sigma_p = K\varepsilon_{vol} \tag{4.65}$$

Using equations (4.47) and (4.64), we can write:

$$K = K_{fr} + \frac{C^2}{M} = K_{fr} + \frac{C}{M}\frac{p_f}{\varepsilon_{vol}} \tag{4.66}$$

By introducing this expression for K into equation (4.65) and reorganizing the equation, we obtain:

$$\sigma_p - \frac{C}{M} p_f = K_{fr}\varepsilon_{vol} \tag{4.67}$$

The above equation tells us that the deformation is proportional to the *effective stress* $\sigma_p^{'}$ defined as:

$$\sigma_p^{'} = \sigma_p - \alpha p_f \tag{4.68}$$

Rather than the total stress σ_p, and the corresponding modulus is K_{fr}, i.e. the same as for the drained test, equation (4.63). Physically this means that the solid framework carries the part $\sigma_p^{'}$ of the total external stress, σ_p, while the remaining part, αp_f, is carried by the pore fluid. The remaining pore pressure $(1 - \alpha)p_f$, is counteracted by internal stresses in the solid. [35]

The parameter α is called Biot's coefficient and is defined:

$$\alpha = \frac{C}{M} = 1 - \frac{K_{fr}}{K_s} \tag{4.69}$$

As mentioned before, K_{fr} is always smaller than K_s. Theoretically, the upper limit for K_{fr} is $(1 - \phi)K_s$, while the lower limit is of course zero, as in the case of unconsolidated or weak rocks. Thus Biot coefficient is restricted to the region $\phi < \alpha \leq 1$. In general the effective stress is defined by:

$$\sigma_{ij}^{'} = \sigma_{ij} - \delta_{ij}\alpha p_f \tag{4.70}$$

We see that only the normal effective stresses ($\sigma_{11} = \sigma_x$, $\sigma_{22} = \sigma_y$, $\sigma_{33} = \sigma_z$, while for the rest $\delta_{ij} = 0$) depend on the pore pressure.

One may note that for $p_f = 0$, Equation (4.43) and (4.69) give $\alpha = \zeta / \varepsilon_{vol}$. Then from equation (4.36), with $p_f = 0$, and the definition of ε_{vol} we obtain:

$$\alpha = \phi \frac{\Delta V_p / V_p}{\Delta V_{tot} / V_{tot}} = \frac{\Delta V_p}{\Delta V_{tot}} \tag{4.71}$$

Which shows that α is a measure of the change in pore volume relative to the change in bulk volume at *constant pore pressure*, such in the case of the drained test.

In addition to the bulk compressibility with respect to confining pressure at constant pore pressure, $1/K_{fr}$, we may define the bulk compressibility with respect to pore pressure at constant confining pressure, $1/K_{bp}$ by letting $\sigma_p = 0$ in equation (4.67) we may write:

$$K_{bp} = -\frac{p_f}{\varepsilon_{vol}} = K_{fr}\frac{M}{C} = \frac{K_{fr}}{\alpha} \tag{4.72}$$

$$\alpha = \frac{K_{fr}}{K_{bp}} \tag{4.73}$$

which shows that Biot coefficient α is the ratio of the bulk modulus at constant pore pressure to the bulk modulus at constant confining pressure. Equation (4.72) is equivalent to c_{bc} defined earlier in Equation (4.4). It is worth noting that using α, Equations (4.55 – 4.57) may be summarized in a simpler equation defined as:

$$\frac{1}{M} = \frac{\alpha}{C} = \frac{\alpha^2}{K - K_{fr}} = \frac{\phi}{K_f} + \frac{\alpha + \phi}{K_s} \tag{4.74}$$

It is worth emphasizing that, equations (4.6), (4.7) and (4.27) all give an effective stress coefficient different from Biot's α defined in equation (4.69). This underlines that the effective stress law will differ depending upon which physical quantity we are studying. There is thus no a priori reason to expect that for example the effective stress law for rock mechanical failure or permeability should be the same as that derived for basic elastic deformation, Equation (4.68) [35].

4.5 THE SKEMPTON COEFFICIENTS

Skempton coefficient, B, is an important parameter in poroelasticity as it relates the applied stress to the induced pore pressure increment under undrained condition. B-coefficient is defined as:

$$B = \frac{\Delta p_f}{\Delta \bar{\sigma}} = \frac{C}{K} = \frac{\frac{K_f}{\phi}\left(1 - \frac{K_{fr}}{K_s}\right)}{\frac{K_f}{\phi}\left(1 - \frac{K_{fr}}{K_s}\right) + K_{fr}\left(1 - \frac{K_f}{K_s}\right)} \tag{4.75a}$$

or in terms of the compressibilities defined in equations (4.4) and (4.5):

$$B = \left(\frac{\partial p_p}{dp_c}\right) = \frac{c_{pc}}{c_{pp} + c_f} = \frac{c_{pp} + c_m}{c_{pp} + c_f} \tag{4.75b}$$

It is clear from the formula that B ≤ 1. Parameters A and B, are originally defined according to [36]:

$$\Delta p_f = B\left[\Delta\sigma_3 + A\left(\Delta\sigma_1 - \Delta\sigma_3\right)\right] \tag{4.76}$$

The form of this equation was chosen to be appropriate for triaxial tests. In such a test, the change in mean stress may be written:

$$\Delta\bar{\sigma} = \frac{1}{3}\left(\Delta\sigma_1 + 2\Delta\sigma_3\right) = \Delta\sigma_3 + \frac{1}{3}\left(\Delta\sigma_1 - \Delta\sigma_3\right) \tag{4.77}$$

which shows that B in equation (4.76) is the same as in equation (4.75). Neglecting K_f relative to K_s in equation (4.75) and introducing Biot's effective stress constant α, we get:

$$B = \frac{K_f}{K_f + \frac{\phi}{\alpha} K_{fr}} \tag{4.78}$$

In the weak frame limit, where K_{fr} can be neglected relative to K_s, we have:

$$B = \frac{K_f}{K_f + \phi K_{fr}} \tag{4.79}$$

As seen from the equations above, B decreases with increasing porosity and decreasing fluid bulk modulus. [35]

5. Failure Mechanics and Hydraulic Fracturing

The classical theories of continuum mechanics have for the most part been constructed so as to be in accord with experimental observations of the behavior of metals and other man-made engineering materials. These theories therefore describe the various types of behavior observed in metals, such as linear elastic, nonlinear elastic, plastic, brittle failure, etc. Although these concepts and models can be applied to rocks, in most cases the analogous behavior of rock is much more complex, undoubtedly because of its heterogeneous and porous nature. [9]

When a piece of rock is subject to sufficiently large stresses, a failure of some kind will occur and the rock changes its shape permanently, and possibly falling apart. The condition is accompanied with a reduced ability to carry loads. Rock failure is an important phenomenon also for petroleum related rock mechanics, as it is the origin of severe problems such as borehole instability and solids production. [9]

5.1 Rock Strength Concept

The stress level at which a rock typically fails is commonly called the *strength* of the rock. Obviously, as *stress level* is not a uniquely defined parameter, neither is strength. Rock strength is therefore a meaningful parameter only when the stress geometry—that is: the type of test, in a laboratory setting—is also specified. In order to illustrate the complexity of rock failure, and to introduce some basic concepts, we will have a look at a couple of the most important tests used to measure rock strength, the *uniaxial* and *triaxial* tests.

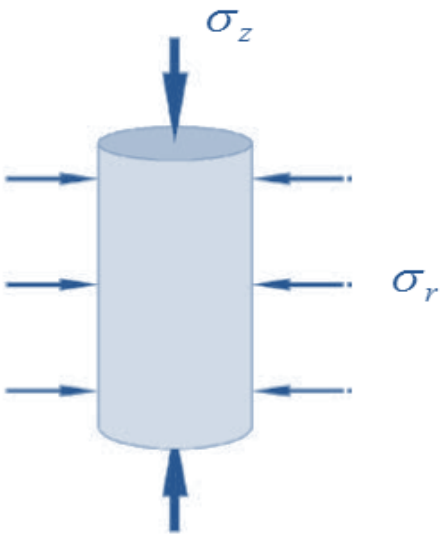

Figure 5.1: Typical specimen for uniaxial stress versus deformation in a uniaxial compression test. Typical diameter is 38 mm. [modified from 35]

Figure (5.1) illustrates a typical test specimen, a cylinder with length to diameter ratio 2:1. A pair of pistons applies (axial) stress to the end faces of the cylinder, while a confining oil bath provides a stress of possibly different magnitude to the circumference. It is normally *assumed* that the stress state within the specimen is homogeneous. If the confining stress is zero, we have a uniaxial stress test (also called unconfined compression test). When the test is performed with a non-zero confining pressure, a so-called triaxial test is performed.

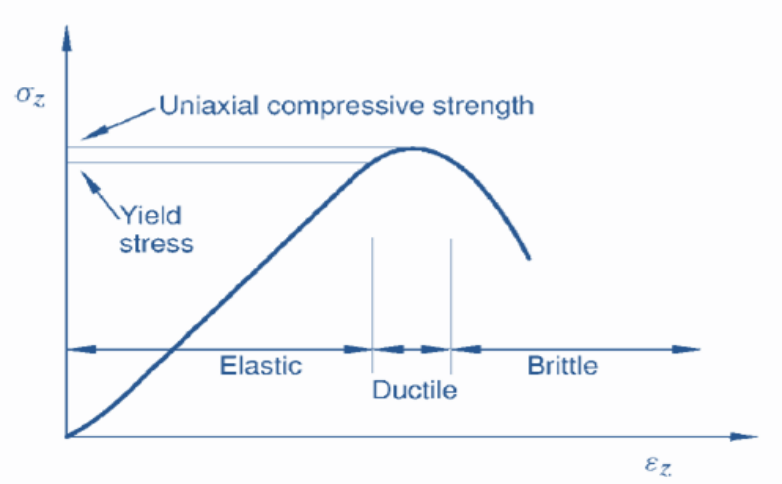

FIGURE 5.2: PRINCIPLE SKETCH OF STRESS VERSUS DEFORMATION IN A UNIAXIAL COMPRESSION TEST. IN PRACTICE, THE DUCTILE REGION MAY BE VERY SMALL [35]

Figure (5.2) shows a typical result from a uniaxial test. The applied axial stress (denoted σ_z) is plotted as a function of the axial strain (ε_z) of the sample. Several important concepts are defined in the figure above:

Elastic region: The rock deforms elastically. If the stress is released, the specimen will return to its original state.

Yield point: The point beyond which permanent changes will occur. The sample will no longer return to its original state upon stress relief.

*Uniaxial compressive strength***:** The peak stress.

Ductile region: A region in which the sample undergoes permanent deformation without losing the ability to support load.

Brittle region: A region in which the specimen's ability to withstand stress decreases rapidly as deformation is increased.

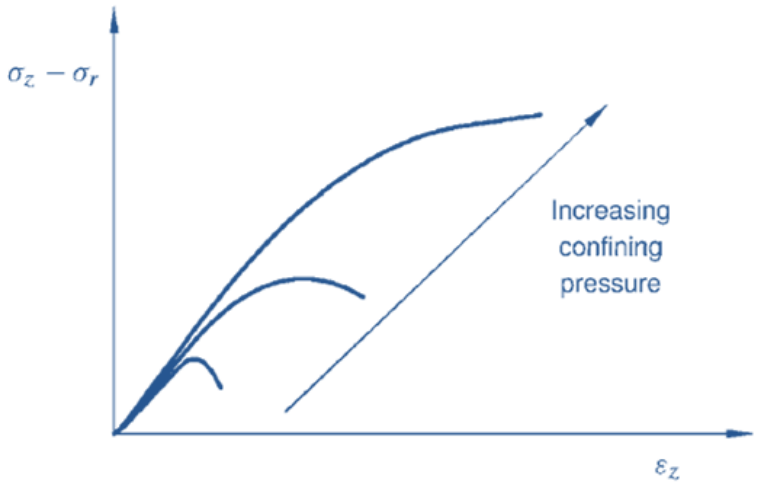

FIGURE 5.3: TRIAXIAL TESTING: TYPICAL INFLUENCE OF THE CONFINING PRESSURE ON THE SHAPE OF THE DIFFERENTIAL STRESS (AXIAL STRESS MINUS CONFINING PRESSURE) VERSUS AXIAL STRAIN CURVES. [35]

A triaxial test is performed by increasing the axial and confining loads simultaneously, until a prescribed hydrostatic stress level is reached. Then, the confining pressure is kept constant while the axial load is increased until failure occurs. The axial loading is normally applied such that it gives a constant axial deformation rate.

For a triaxial test, it is customary to plot the difference between the axial stress and the confining pressure (σ_r) versus the axial deformation. In such a test, the intermediate principle stress and minimum stress are set to be equal, $\sigma_2 = \sigma_3$, which again are represented by σ_r. From this test one obtains a curve that looks similar to Figure (5.2). However, the behavior may be quite different at the higher stress levels. Figure (5.3) illustrates results from triaxial tests with various confining pressures. It is seen that for the higher confining pressures, σ_r, the specimen's ability to support load is not lost, although its stiffness is clearly reduced. Keep in mind that higher value for the confining pressure in Figure (5.3) would imply larger differences between the axial stress σ_z and the confining pressure σ_r, as σ_z and σ_r are increased simultaneously [35].

So far, we have not given a precise definition of failure, mainly because it is rather difficult to give a general definition. Indeed, the destruction of a rock by load is partly dependent on the loading system and is not a true rock property. For the uniaxial test shown in Figure (5.2), a seemingly unambiguous definition of failure may be given, corresponding to the peak stress point on the curve. For the higher confining pressures in Figure (5.3), one may on the other hand define failure at some point where the slope of the stress–strain curves changes. This may not seem totally appropriate, however, since the specimen still supports increasing load after it has failed. Disregarding these problems, we shall in the following sections discuss failure criteria assuming that a consistent definition of failure exists.

The concept of rock failure is associated with the state of the solid framework. Thus, the stresses that cause failure are the *effective stresses* felt by the framework. The effective

stress concept was originally introduced in soil mechanics by Terzaghi in 1923 on an empirical basis. Terzaghi argued that

1. Increasing the external hydrostatic pressure produces the same volume change of the material as reducing the pore pressure with the same amount.

2. The shear strength depends only on the difference between the normal stress σ and the pore pressure p_f.

It should be noted however that the relation specifying the effective stress in a failure criterion is in general different form the relation expressed in equation (4.68), which specifies the effective stress for deformation of a linearly elastic material [35].

5.2 THE FAILURE SURFACE

From the considerations above, we see that a rock fails when the stress exceeds a certain limit, while it remains, more or less, intact as long as the stress is lower than this limit. We also see that this limit depends on the total stress state, not only the stress in one direction. A graphical representation of this in an abstract "stress space" turns out to be quite useful. Consider a test specimen of an isotropic material, subject to a certain stress state described by the three principal stresses σ_1', σ_2', σ_3'. We may represent the stress state graphically as a point in the *principal stress space*, that is, the space spanned by the $\sigma_1', \sigma_2', \sigma_3'$ axes. Imagine that the specimen is taken to failure by increasing the principal stresses in some manner, and that the point of failure is plotted in the principal stress space. If this procedure could be repeated an infinite number of times, following different stress paths, we would get an infinite number of failure points in the stress space. We assume that these points will form a continuous surface, which we call the *failure surface*. A schematic illustration of such a surface is shown in Figure (5.4).

The failure surface may be described by the equation:

$$f\left(\sigma_1', \sigma_2', \sigma_3'\right) = 0 \qquad (5.1)$$

In this simplified picture, the assumption is that the rock is intact at states inside the failure surface, while it fails for any stress state outside. This does not imply that any stress state outside the failure surface is inaccessible, since the rock may under suitable conditions be able to support increasing load even after failure, as previously mentioned.

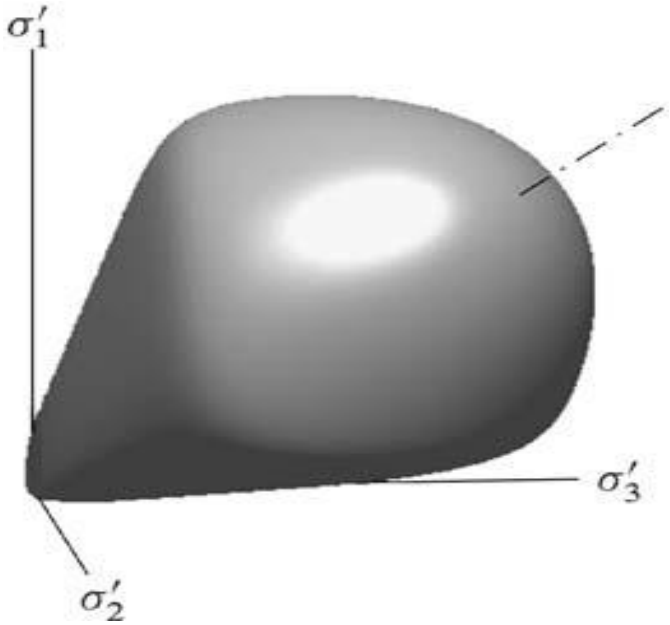

FIGURE 5.4: SCHEMATIC PICTURE OF A FAILURE SURFACE IN PRINCIPAL STRESS SPACE. THE DASH–DOT LINE REPRESENTS THE HYDROSTATIC AXIS. NOTE THAT THE CONVENTIONAL RELATION $\sigma_1' \geq \sigma_2' \geq \sigma_3'$ HAS BEEN ABANDONED IN THIS FIGURE, IN ORDER TO ILLUSTRATE THAT THE FAILURE SURFACE IS CLOSED: THE ROCK IS SUPPOSED TO FAIL AT SOME STRESS LEVEL, FOR ANY RATIOS BETWEEN THE PRINCIPAL STRESSES. [35]

5.3 EFFECT OF CONFINING STRESS

It is well known that if the confining stress applied to the sides of a cylindrical specimen during a triaxial compression test is increased; then axial stress required to cause failure will increase, and the rock will show a tendency toward greater ductility [9].

The effect that confining pressure has on the axial stress vs. axial strain curve is shown in Figure (5.5a) for a Rand quartzite. For each value of $\sigma_2 = \sigma_3$ the stress-strain curve initially exhibits a nearly linear elastic portion, with a slope that is nearly independent of the confining stress. But both the yield stress and the failure stress increase as the confining stress increases. Finally, there is a small descending portion of the curve, ending in brittle fracture.

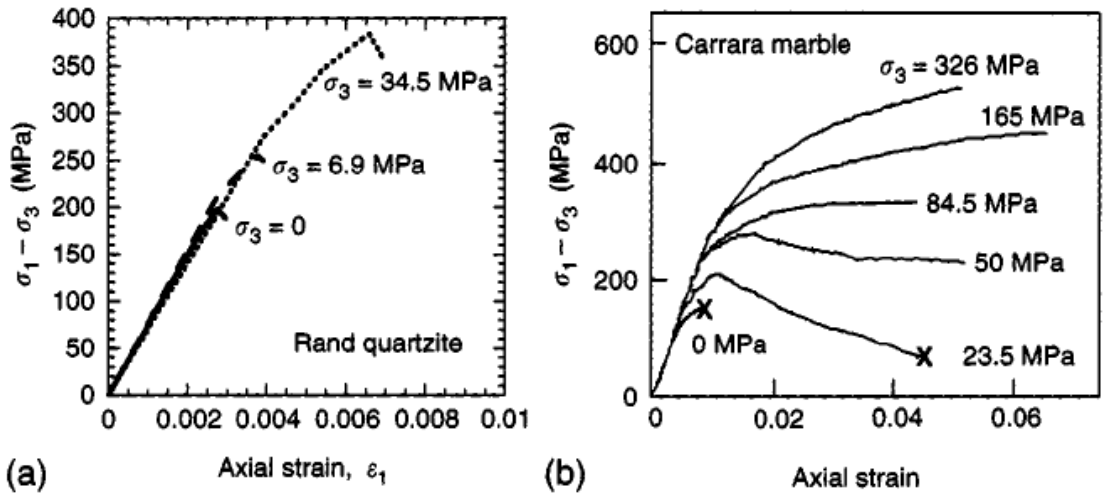

FIGURE 5.5: STRESS-STRAIN CURVES FOR *DIFFERENT* ROCKS AT VARIOUS CONFINING PRESSURES. CROSSES INDICATE ABRUPT BRITTLE FAILURE [9]

A different type of behavior is exhibited by other rocks, notably carbonates and some sediments. Figure (5.5b) shows the data collected on a Carrara marble [9]. For sufficiently low confining stresses, exemplified by the curve labeled σ_3 = 0 MPa, brittle fracture occurs as for the quartzite described above. But at higher confining stresses, such as the curve labeled 50 MPa, the rock can undergo a strain as large as 7 percent, with no substantial loss in its ability to support a load (i.e., no decrease in the axial stress). In this case the rock is said to exhibit *ductile behavior***,** which can be loosely defined as "the capacity for substantial change in shape without gross fracturing" [37].

The curve for σ_3 = 23.5 MPa can be said to show a transitional type of behavior, in that quite substantial inelastic strain occurs, but the rock eventually fails by brittle fracture. Hence, there is a somewhat ill-defined value of the confining stress at which we can say there occurs a transition between brittle and ductile behavior.
At higher confining stresses, such as 165 MPa or above in Figure (5.5b), the axial stress σ_1 continues to increase with strain after the yield point has been passed. Such behavior is known as *work hardening* in metallurgy, and more simply as *hardening* in rock mechanics. Following this nomenclature, the behavior shown in the descending portion of the stress-strain curve, such as that exhibited in Figure (5.5b) at a confining stress of 23.5 MPa, is often referred to as *softening*.

5.4 EFFECT OF PORE FLUIDS

The foregoing discussion of rock failure has ignored the fact that rocks are typically porous to some extent, and the pore space of a rock will *in situ* be filled with fluids under pressure. The pore fluid is usually water, but may be oil, gas, or rock melt. The pore fluid may affect the

failure of the rock in two ways: due to the purely mechanical effect of pore pressure, or due to chemical interactions between the rock and the fluid [9].

With regards to the mechanical effect of pore fluid pressure, it seems plausible that pore pressure, which acts "outward" from the pore space, would in some sense act like a tensile stress affecting only the normal stresses, while the shear stresses that are due to differences in the principal stresses will remain unaffected [9]. Moreover, in an isotropic rock, this effect should be the same in any three mutually orthogonal directions. Reasoning along these lines, it is proposed [38], that the failure of a soil could be controlled by the effective stress σ_i', which would be the principal stresses, reckoned positive if compressive, *minus* the pore pressure, that is,

$$\sigma_1' = \sigma_1 - \alpha p_f \ , \ \sigma_2' = \sigma_2 - \alpha p_f \ , \ \sigma_3' = \sigma_3 - \alpha p_f \qquad (5.2)$$

Since Biot's effective stress constant α, was given under the assumption that the rock is linearly elastic, it is not directly applicable for a rock at failure. Most *experiments* on rocks, however, support the conclusion that the effective stress law (5.2) holds, which is to say that the effective stress coefficient for failure is unity [9 & 13].

In the context of a Mohr diagram, replacing the stresses σ_i with the effective stresses σ_i' has the effect of *translating* all the stress circles to the left by the amount αp. The Mohr's circle will therefore be shifted closer to the failure line. Hence, an *in situ* state of stress that is "safe" in the absence of a pore pressure may well cause the rock to fail if the pore pressure is increased by a sufficient amount Figure (5.6). This fact accounts for the increased occurrence of landslides in the aftermath of heavy rainfall.

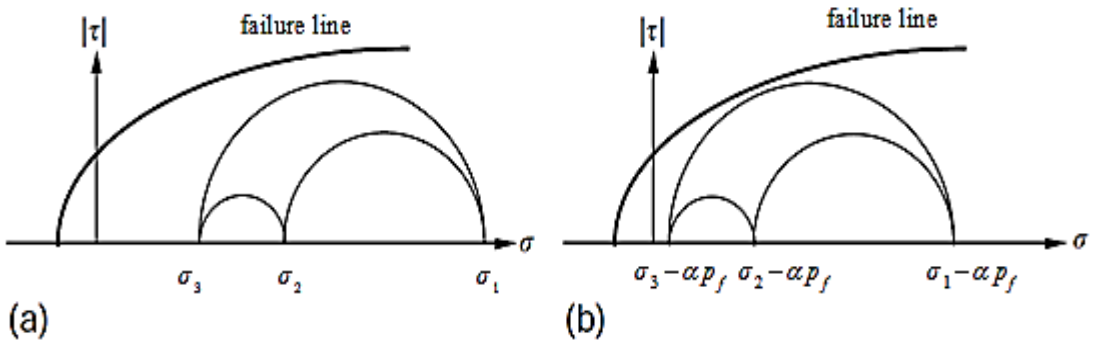

FIGURE 5.6: A STRESS STATE THAT LIES BELOW THE FAILURE CURVE. (B) APPLICATION OF A PORE PRESSURE CAUSES THE EFFECTIVE STRESS STATE TO MOVE CLOSER TO THE FAILURE CURVE. [9]

Thus, according to the effective stress concept, the criterion for failure becomes:

$$\sigma_3' = \sigma_3 - \alpha p_f = -T_0 \qquad (5.3)$$

where T_0 represents the tensile strength. This result is consistent with the concept that tensile failure is caused by the stress concentrations at the edges of thin cracks oriented normal to the direction of the least compressive principal stress. [9].

Following, we will go more in detail concerning the conditions around Equation (5.3).

5.5 HYDRAULIC FRACTURING

Hydraulic fracturing in rocks takes place when the fluid pressure within the rock exceeds the smallest principal stress plus the tensile strength of the rock. It leads to tensile failure or splitting of the rock. A hydraulic fracture may be initiated by natural, geological processes in the earth whereby the fluid pressure increases and/or the smallest principal stress decreases. Man-made hydraulic fractures in petroleum activities are normally initiated by increasing the fluid pressure in the borehole to the point where the smallest principal stress at the borehole becomes tensile. Continued pumping at an elevated pressure causes the formation to split and the fracture will grow in the direction of least resistance. Some distance away from the borehole the fracture will always propagate in the direction perpendicular to the smallest principal stress in that specific formation. [35]

As the least principal stress often is in a horizontal direction, the resulting fractures will be vertical. If we consider a vertical open hole, the picture will be as indicated in Figure (5.7). As the figure shows, two symmetric fracture wings develop perpendicularly to the least principal stress.

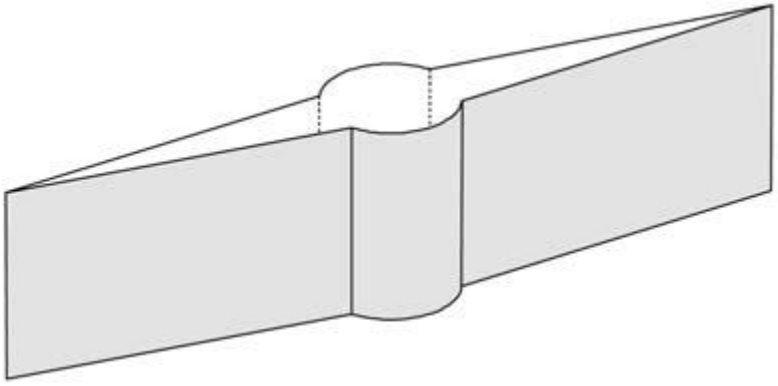

FIGURE 5.7: VERTICAL FRACTURE AROUND A VERTICAL WELL [35]

As hydraulic fracturing is directly linked to tensile failure of the formation [35], we will investigate the conditions for such a failure.

From a macroscopic point of view, fracturing is related to tensile failure. Generally, when considering a test specimen of solid material, tensile failure will occur when the traction exceeds the tensile strength T_0.

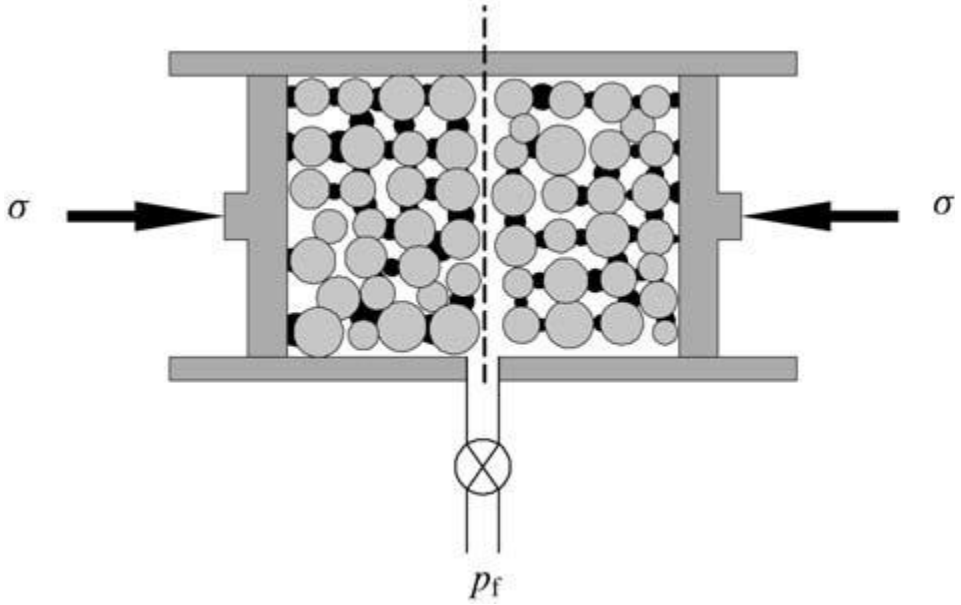

FIGURE 5.8: HYDRAULIC FRACTURING OF A POROUS AND PERMEABLE ROCK [35]

Following the usual convention that stresses are positive in compression, this condition reads:

$$\sigma < -T_0 \tag{5.4}$$

For porous materials the total stress should be replaced by the effective stress, and the condition will then be:

$$\sigma - p_f < -T_0 \tag{5.5}$$

where p_f is the pressure in the pores. For reasons mentioned in chapter 5.4, the relevant effective stress coefficient, α, here is equal to 1.

For porous materials it is however worthwhile to consider the condition above more in details. Assume that we have a plug of porous and permeable material in a triaxial cell as sketched in Figure (5.8). The plug is subjected to an external stress σ. The pore pressure p_f can be varied. A confining pressure may be applied, but this will however not affect the argumentation.

Consider first that the grains are cemented to each other and that the plug is glued to the pistons. Along the dashed lines the bonds are however broken, thus forming a closed fracture. The force tending to close this fracture will obviously be given by the difference between the applied pressure σ and the pore pressure p_f in the fracture. The condition for opening of the fracture will thus be [35]:

$$\sigma - p_f < 0 \tag{5.6}$$

This condition can of course be reached *either* by increasing the internal pressure p_f *or* by reducing the external stress σ. In a short plug like the one indicated in Figure (5.8) the internal pressure p_f will be constant throughout. But if we consider a long plug with much

smaller permeability, the same way of reasoning makes it clear that the pressure p_f in Equation (5.6) is the pressure in the fracture, not the average pressure in the plug [35].

6. LABORATORY INVESTIGATION

The experimental investigation carried out for this master thesis consists of small scale laboratory tests. The chief purpose of the laboratory investigation is to gain a more comprehensive understanding of the different mechanics involved in the use of bentonite mud as a sealing material for plugging of a well. Minor purposes have been to investigate some of the frequent claims in the industry concerning the sealing properties of barite after it has settled down (sagging).

The primary perspective on the sealing behavior of bentonite mud has developed during laboratory investigation and several additional experiments on the same material and other similar by nature materials were conducted to confirm the validity of this development.

6.1 TEST EQUIPMENT AND EXPERIMENTAL SETUPS

The two main setups followed for the different tests are described in details below.

6.1.1 THE MAIN EXPERIMENTAL SETUP

Different equipment have been used to produced and verify the results obtained. The primary test equipment consists of a transparent PVC pipe has been used throughout the laboratory investigation. This pipe has total length of 40 cm, with an outer diameter of 5 cm and an inner effective diameter of 4.1 cm.

Here is a list of the equipment used for the main experimental setup:

- A pipe made of polyvenyletylen (PVC) as illustrated in Figure (6.1)
- A water pump (Ruska) as shown Figure (6.2)

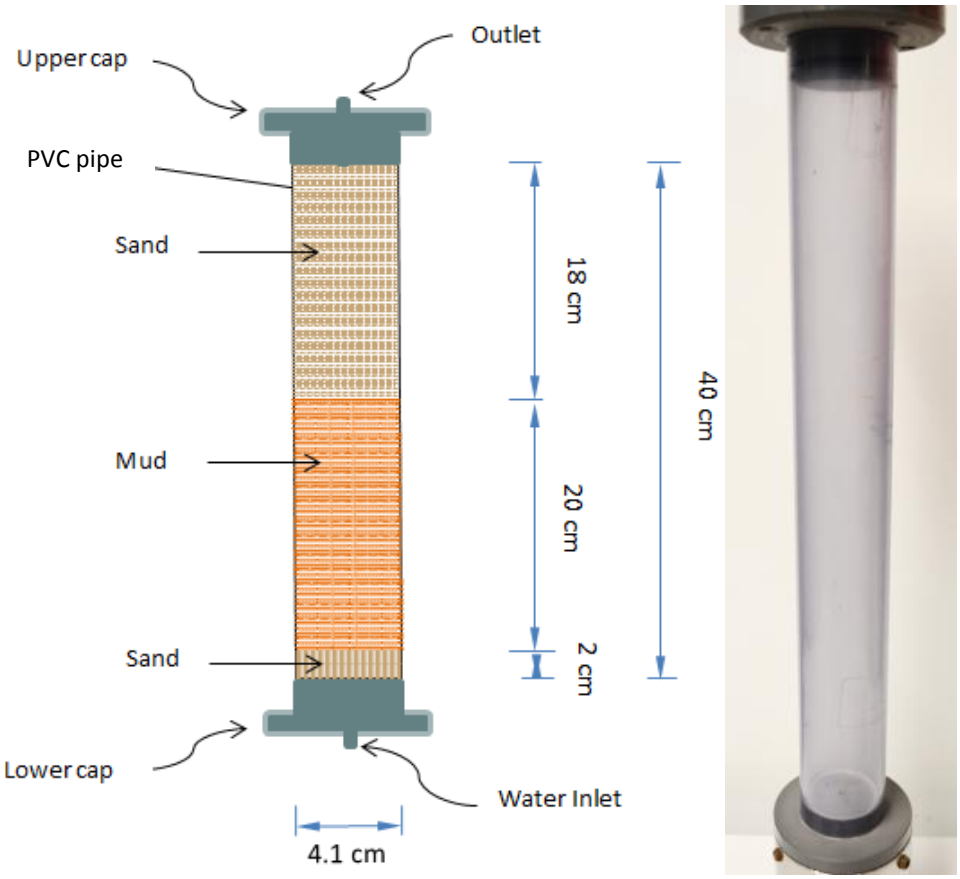

FIGURE 6.1: EXPERIMENTAL SETUP FOR THE PIPE CONTAINING BENTONITE MUD AND SAND. DURING NORMAL PROCEDURE, THE HOLE IN THE OUTLET CAP WAS KEPT OPEN THE WHOLE TIME.

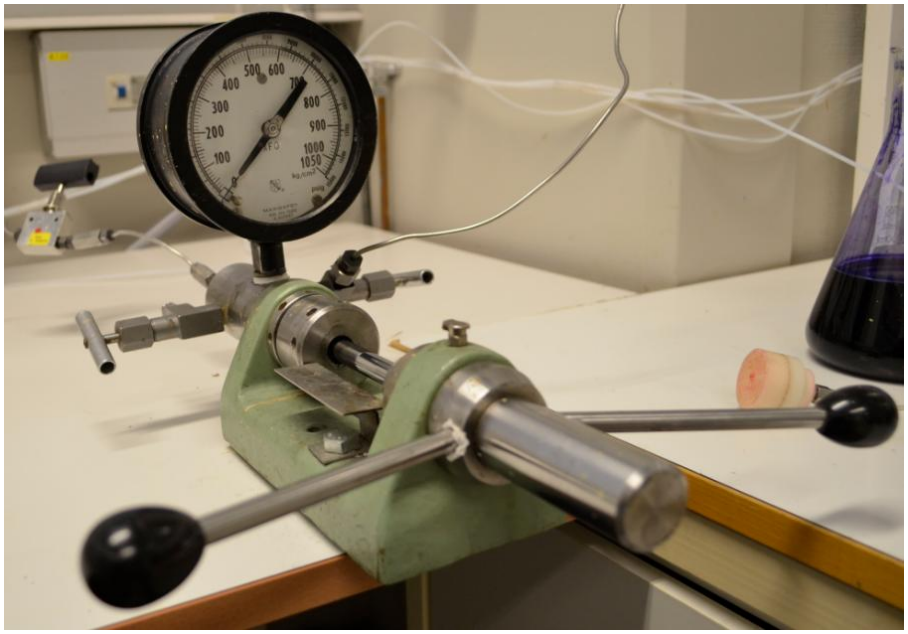

FIGURE 6.2: RUSKA PUMP USED TO INJECT COLORED WATER INTO PIPE FILLED WITH BENTONITE AND SAND

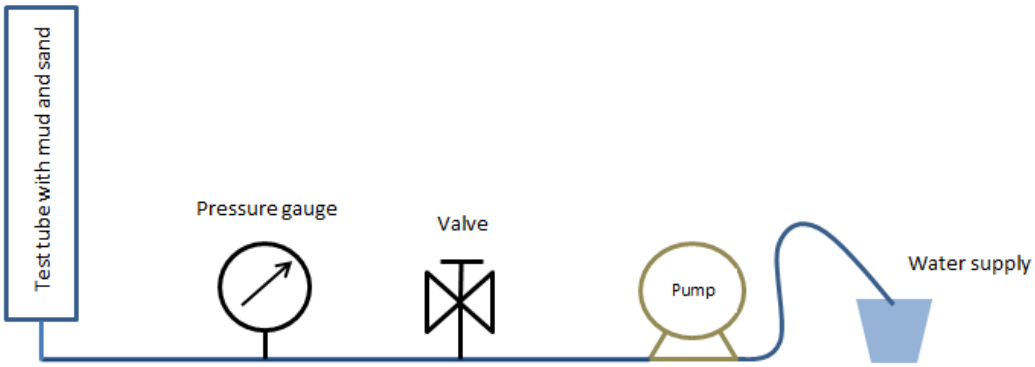

FIGURE 6.3: SCHEMATIC ILLUSTRATION OF THE MAIN EXPERIMENTAL SETUP

Usual setup for most of the test preformed is shown in Figure (6.3). Water, colored blue, was used to feed the pump. The coloring of water was done in order to better distinguish the path it takes in its way migrating upward through the mud column in the PVC pipe. This turned to be quite useful when the mud column was exchanged with Laponite transparent gel column, as we will show later.

The pump used in the setup above, “Ruska pump”, had a quite limited capacity for water uptake at each turn. Its load was approximately 10 ml of water, when all of this was injected into the pipe to the left in Figure (6.3), one had to close the valve and then start refilling the pump.

6.1.2 THE ALTERNATIVE EXPERIMENTAL SETUP

This alternative experiment has been conducted to give us a further verification of the results we got from the main experiments. The description of this setup is simply a portrait of the setup for the unique Oedometer that has been used.

Morten Ivar Kolstø (PhD student) designed the Oedometer cell shown in Figure (6.4). It is used for testing the elastic and acoustic properties of the sand and/or clay mixtures under uniaxial strain condition. The most important includes in this Oedometer compared to popularly used Oedometer cell is the possibility to measure both horizontal and vertical P-wave in combination with a vertical S wave.

We can divide the complete test apparatus into two setups: An internal and an external. The internal setup consists of: a) A main chamber, b) A piston and c) A Load frame. The main chamber and piston are made of stainless steel material. The sample holder is most prominent part of the main chamber. It has a diameter of 69.90 mm, a height of 40 mm and is located in the middle of the main chamber. The thickness of the outer ring measured from the wall of the sample holder to the outskirt of the main chamber is 50.00 mm to ensure negligible lateral strain during tests. The sample is loaded from the top to bottom.

There are two fluid flow channels connected to the base and of the sample holder and additional two connected to the piston part of the internal setup, where one of these two channels is an injection channel connected to Quisix pump and the other act as a drainage channel. In order to prevent the bentonite from escaping through the drainage channels, a 3 mm thick filter made of stainless steel and with a specific filtering capacity of 0.5 µm is placed above the lower drainage channels and below the upper drainage channels. For complete sealing at the base, a second paper filter with identical properties is placed beneath the steel filter. The areas outside the steel filter are filled with silica gel. It must be emphasized that the contact area for this particular sealing is small making it possible to apply desired stress ≈ 10 MPa during tests.

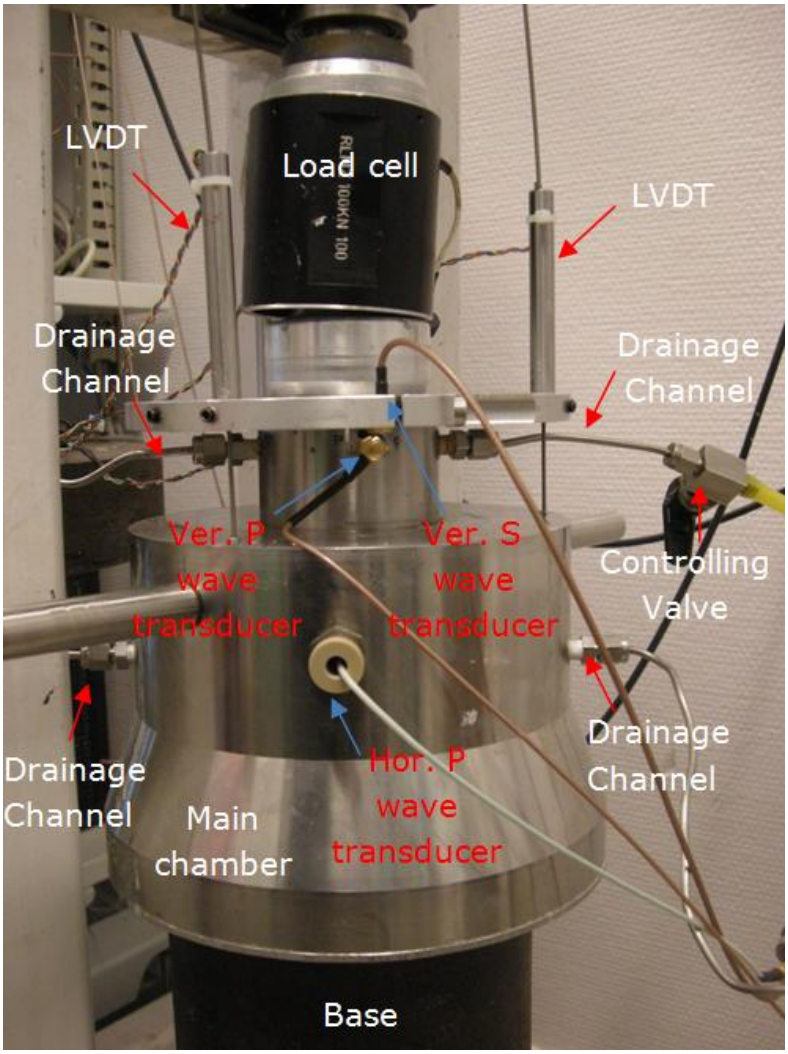

FIGURE 6.4: THE BASIC SETUP OF OEDOMETER CELL. WAVE TRANSDUCER WERE NOT NEEDED FOR OUR PURPOSE AND NEVER USED (WRITTEN IN RED). ONE OF THE TWO LOWER DRAINAGE CHANNELS WAS CONNECTED TO QUISIX PUMP AND USED TO INJECT WATER INTO SAMPLE HOLDER, WHILE THE OTHER BOTTOM DRAINAGE CHANNEL WAS CLOSED. THE TWO UPPER DRAINAGE CHANNELS WERE KEPT OPEN ALL THE TIME.

There are some acoustic devices mounted at the center of the sample holder base used to control different measurements, but since the acoustic part has not been utilized in our experiment, we will not go into the details of how this part works.

The piston used to exert load from the load frame onto the sample, is decorated with both the same type of filter and drainage system as at the base of the sample holder together with an identical acoustic device in the center, Figure (6.4) and (6.5).

Two O-ring are used for sealing. The first O-ring is mounted around the piston to prevent the slurry to penetrate beneath the filter accessing the drainage channels. To reduce the friction between the first O-ring and the sample holder wall down to minimum, the O-ring is gently lubricated with a thin oil film. Finally, to prevent any damage on the silicon sealing between the filter and the peek front piece during testing and pre-testing two stainless steel screws are used to mount the steel filter onto the piston.

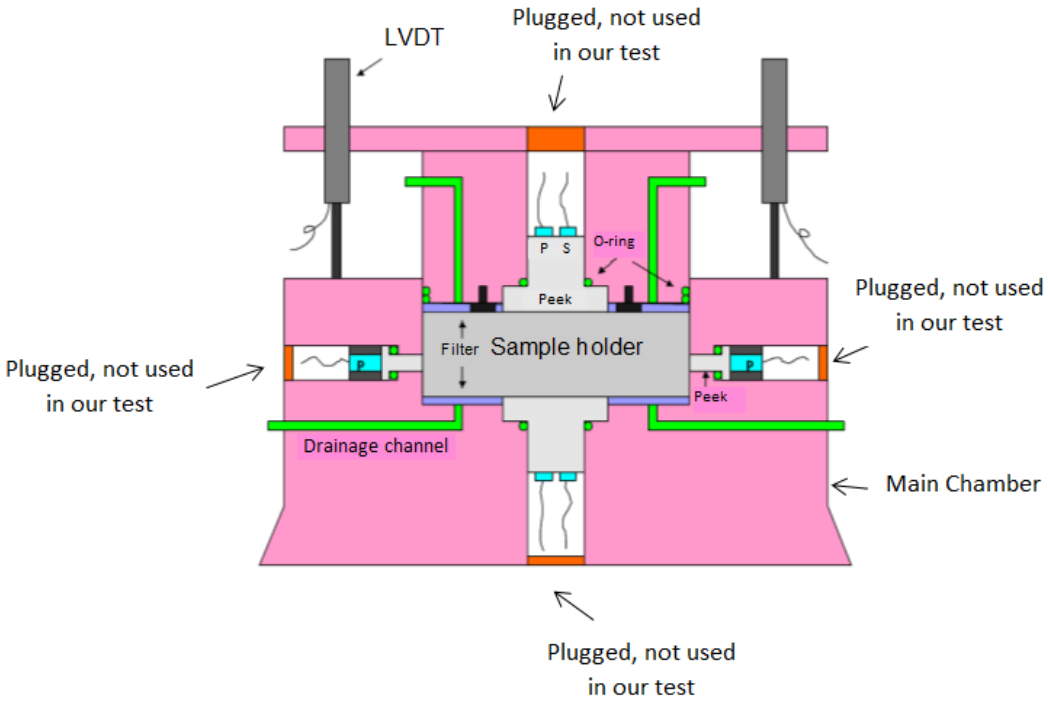

FIGURE 6.5: SCHEMATIC ILLUSTRATION OF THE MAIN CHAMBER

The load frame is used to create external stress on the sample. A set of about 25 kg dead weight are used in one end of the lever exerting stresses through a thick steel rod and a load cell mounted on top of the piston Figures (6.4) and (6.6). Since a lever is used, the stress level will vary during a loading due to the compaction of the sample. Consequently, the system needs to be calibrated to be able to control the stress change with the lever position for the particular dead weight. This calibration was conducted prior to the test and estimates the conversion factor from volt to kN.

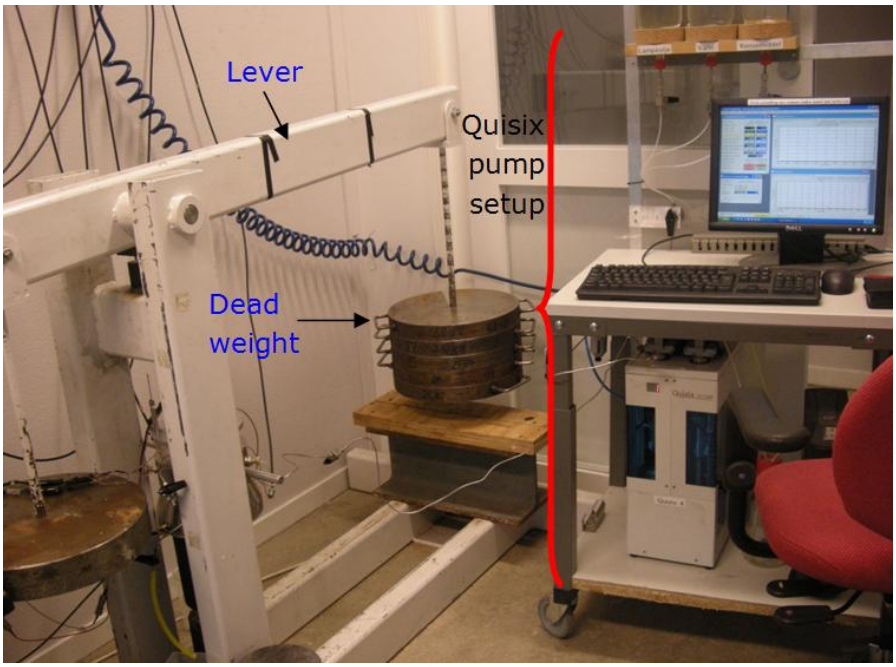

FIGURE 6.6: LOAD FRAME TO THE LEFT AND QUISIX PUMP AND ITS OPERATING COMPUTER TO THE RIGHT

The external setup in the Oedometer cell comprises: a) A Quisix pump; b) Device measuring the compaction of the sample during the test with a software and acquisition setup and c) Acoustic acquisition setup (not used). An automatic software controlled Quisix pump is used to gain the desired water pressure applied onto the sample, Figure (6.7). It comprises two pumps that maintained the desired programmed pore pressure adjusting alternatively by receiving or delivering the pore fluid. This system can measure both delivered and received pressure.

A device called Linear Variable Differential Transformers (LVDT) measures the change in length of the sample with high level of precision. Three LVDTs are used to monitor the compaction in different parts of sample surface. Calibration tests were performed to find out the range of measurable length change with higher precision and conversion factor from volt to length. The measurable range of length change estimated is about 10-12mm. An acquisition station monitors and acquires the uniaxial compaction and applied stress data. Amplifier quantifies the length change and stress according to calibration data provided to the software Figure (6.7). Since the applied water pressure and stress-compaction data were recorded in time, the time in all PCs were synchronized to ±2 seconds.

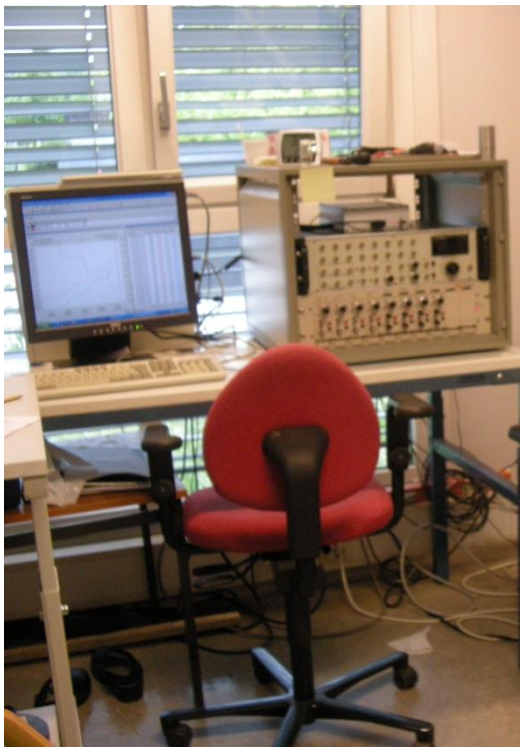

FIGURE 6.7: COMPACTION AND STRESS DATA ACQUISITION SETUP FOR OEDOMETER TEST.

6.2 TEST MATERIALS

Different materials have been used during the laboratory investigation. These are the following:

1- Two types of bentonite were used in combination with barite and HEC. The specifics of this combination were provided to me by my supervisor after some preliminary test done by others ahead of this thesis. The first type of bentonite used here was bentonite pellets marketed as Mikolit B and supplied by Rotek. The data sheet for these pellets is to be found in the Appendix (B). The second type of bentonite used here was bentonite powder (organically modified smectite) with rheological additive 128 provided from Norbar Minerals AS.

   The main ingredients of the mud were 250 gram bentonite pellets, 100 grams powdered bentonite, 400 grams barite, 5 grams HEC 10 polymer, which adds extra viscosity to the water based mud, and 1.5 liters of water, Figure (6.8).

2- Laponite gel: Laponite is a synthetic material that closely resembles natural clay minerals both in structure and composition. The material is delivered as a white powder. To produce the clay like get, the powder is mixed with water while continuously stirring. Necessary protection should be used when handling the material since it is very corrosive. One of the major advantages of Laponite is that the gel is transparent. This property of the gel makes it very useful material to see

the process as the fluid under pressure migrates upward through the gel. The used mixture of water and Laponite contains 6% by weight Laponite to water. According to the manufacturer, Appendix C, the gel produced from this mixture has shear strength of approximately 1 kPa. Figure (6.8)

FIGURE 6.8: SAMPLE OF BENTONITE PELLETS AND LAPONITE POWDER TOP, BENTONITE MUD (LOWER LEFT) AND LAPONITE GEL (LOWER RIGHT)

The procedure for the making of bentonite mud used for the experiments is as follows:

1. Mix 250 grams of bentonite pellets with 500 ml of water. The pellets were then left in water to hydrate for a minimum of 72 hours. This in order to get as much swelling of bentonite as possible.

FIGURE 6.9: HYDRATED BENTONITE PELLETS AFTER 72 HOURS (LEFT). THE RESULT OF MIXING DESCRIBED IN POINT 2 AND POINT 1 (RIGHT)

2. Mix 400 grams of barite, 100 grams of powder bentonite, 5 grams HEC and 1 liter of water in a blender till the powder is fully dissolved in water. Using of a mixer, the blend is mixed with the swollen bentonite pellets. The density of the final mix was around 1800 kg/m^3. The procedure for making of Laponite gel was quite straight forward. Mixing of 6 weight % in a volume of water while continuously stirring until all the powder has dissolved in water and we get the clear gel, Figure (6.8).

6.3 EXPERIMENTS PROCEDURES

During the testing period, the experimental procedure for the main experiment was frequently refined to ensure reliable results and count for any source of error. The main procedure that was used though is the one which the setup has been described in Figure (6.3). For the case of the alternative experiment, the procedure followed there remained unchanged throughout the experimenting period. The two procedures are described below.

6.3.1 THE MAIN PROCEDURE

Recall the PVC pipe described in Figure (6.1). The inlet for water coming from the pump is located in the lower end of the pipe. Since the caps used for the pipe had no filter to distribute the injected water as seen from Figure (6.10), it was necessary to make some sort of filter that distributes the pressurized water coming from pump in all directions. For this purpose, a thin layer of fine sand was used in the lower/injection end of the pipe.

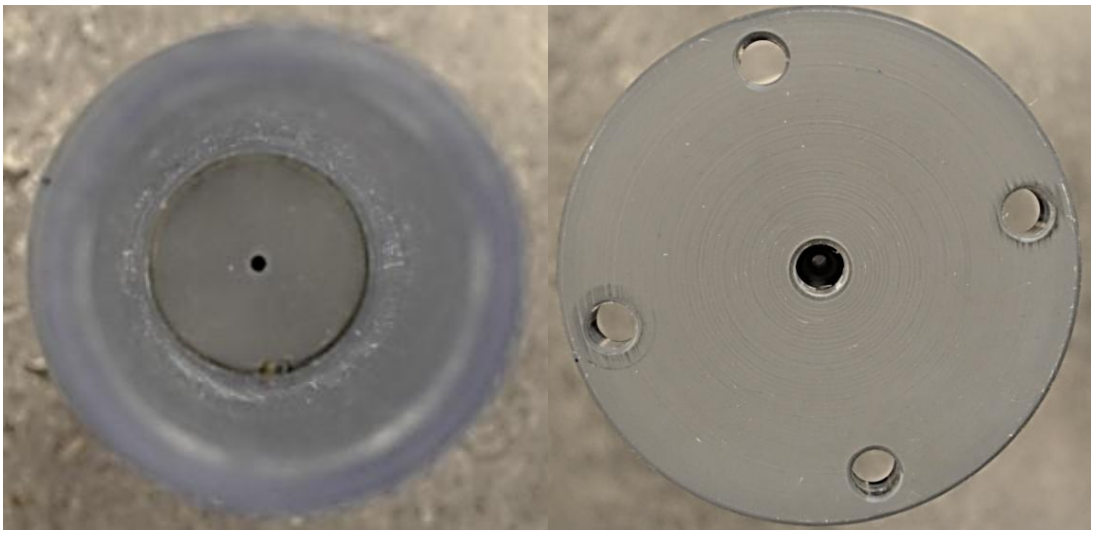

FIGURE 6.10: TOP VIEW (LEFT) AND BOTTOM VIEW (RIGHT) OF THE CAPS USED FOR THE PVC PIPE WITH THE INJECTION INLET IN THE CENTER OF THE CAP

In order to avoid blowing out the content of the PVC pipe due to the increased pressure inside it, the upper and lower caps were bolted together by four iron rods. The holes in the caps made for this purpose is particularly seen in Figure (6.10 right). During normal procedure, the hole in the upper/outlet cap was kept open for atmospheric pressure, which means the pressure in the sand column was equal to atmospheric pressure.

Prior to commencement of each test, the pipe was wiped clean; the lower cap is attached firmly. Fine sand was then poured into the pipe to make a thin layer right above the inlet hole in the lower cap working as a filter distributing the injected water. This layer is then pressed firmly in order to make a compacted filter and have a horizontally flat contact with mud column. The inside of the pipe is then wiped clean of any sand particles sticking to the inner walls of the pipe, this in order to have a clean mud to pipe contact and minimize any uncertainty factors. Mud is then put in place inside the pipe simply by the means of a spoon as it is quite thick and not easy to be poured in place. Any trapped air pockets and bubbles are then burst by carefully fiddling about with a thin iron rod and until the mud column is as bubble free as possible. The inside of the pipe is then wiped clean of mud above the specified mud level, which again is as horizontal and flat as possible. The sand column is then built up by pouring of sand in intervals onto the mud column until it reaches its prescribed level. At the end of each interval, the sand is pressed hard in order to make it as compacted as possible and thus minimize any movement of mud column that are due to compaction of the above sand column. The sand column work is sort of a plug that is there to prohibit mud from escaping the pressing water from below, making the conditions just right for the experiment. The upper cap is then put on pipe and bolted firmly to the lower cap by four rods, as mentioned earlier. The pipe is now ready for the experiment and is assembled into the system as shown in Figure (6.11).

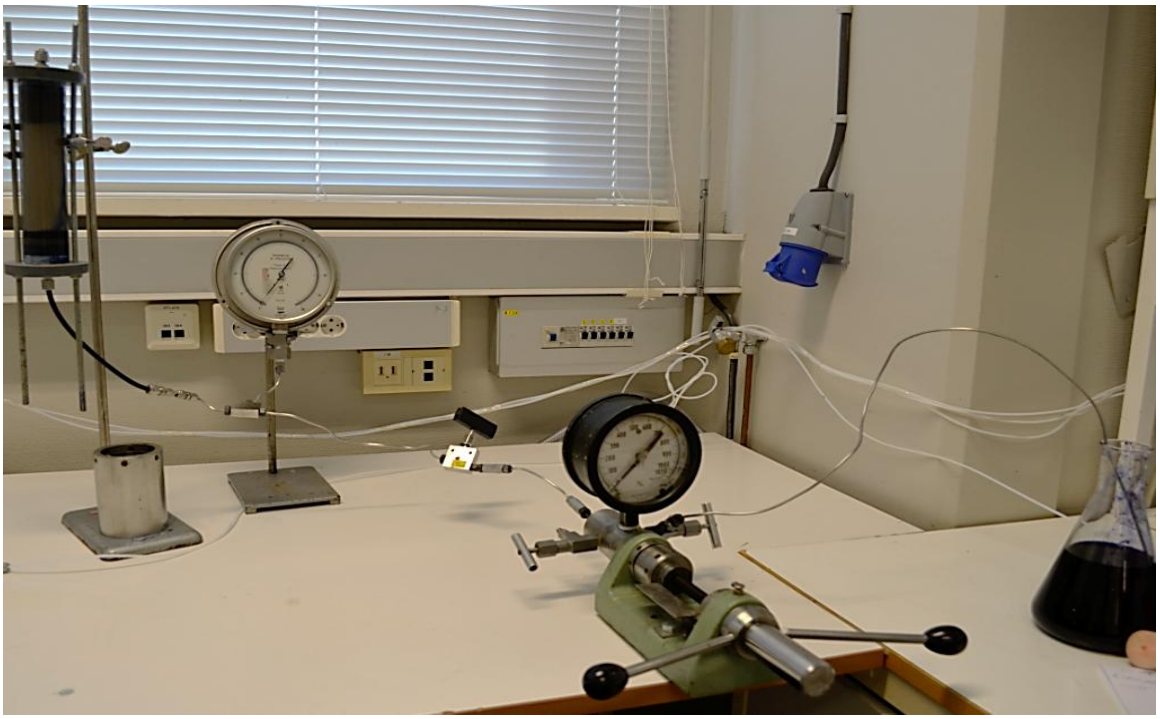

FIGURE 6.11: THE MAIN EXPERIMENTAL SETUP. COLORED WATER, BLUE, IS FEED TO THE PUMP, WHICH INJECTS IT INTO THE PIPE FAR TO THE LEFT WHILE CONTINUOUSLY MONITORING THE PRESSURE IN THE MUD COLUMN WITH A PRESSURE METER (LEFT TO THE CENTER IN THE PICTURE)

In order to accurately know the amount of injected water, the pump was fed with maximum water it could take and the volume was measured to be 10.5 ml. The total number of full turns (360°) of the pump handle is 16 and for every turn the volume of water injected was measured to be 0.332 ml. The exact amount of injected water was simply a task of counting the number of turns of the pump handle.

The tests were executed according to the set up described in Figure (6.11). Here is how the tests were run and the data were gathered as follows:

1- Water was pumped into the pipe until a startup pressure of 5 bars was reached and pumping then stopped.
2- For a period of 60 seconds, the pressure was maintained at startup. During this period, any decrease in pressure below this level, mainly due to mud compaction, was then met by injection of water until the pressure was re-established at 5 bars.
3- The amount of water injected to keep up with the pressure reductions during these 60 seconds was then recorded.
4- Water was slowly pumped into the pipe until the pressure was increased by one bar and the pumping was then stopped.
5- Step 2, 3 and 4 were then repeated for every bar in the pressure range of interest [5 - 15] bars.

The data were registered in tables and later charted in figures, which will be taken up in the next chapters.

6.3.2 THE ALTERNATIVE PROCEDURE

This procedure was used for the case were hydrated bentonite has been compacted in an Oedometer. Bentonite in this case was poured into sample holder and filled to a height of 30 mm. Given sample holder diameter of 69.9 mm, this would imply a total initial sample volume of
115.123 x 10^3 mm^3. The piston, part of a lever connected to a dead weight, was then placed on top of this and a constant net piston force on the sample of about 35 bars was applied. Bentonite was then slowly drained from its water, escaping through the four drainage channels shown in Figure (6.4), and its original volume was therefore decreasing. When the lever leveled with the ground after some days, the compaction then stopped, and we needed to refill sample holder again to its original height of 30 mm. The original piston force was re-applied on the sample. This was done in order to give our final bentonite sample as much height as possible. The added volume to sample due to refilling process (3 in total) was in total of 190 x 10^3 mm^3 added to the original sample volume. Counting this added volume into the overall volume to be compacted (190 x 10^3 mm^3 + 115.123 x 10^3 mm^3 = 305.123 x 10^3 mm^3) and we get 0.305123 cubic meters.

The procedure conditions and execution of the experiment was done as follows:

1- Initial piston force on applied hydrated bentonite sample was 35 bars.

2- Pump (injecting blue colored water) is connect to one of the lower drainage channels, herby named injection channel, while the other channel is kept closed to prevent water from escaping through it rather than through mud. Pump injected water at constant rate into the sample holder and the pressure, during the course of one minute, is then increased to 5 bars. The total working force applied on the sample is now 35 bars + 5 bars = 40 bars. This force is maintained constant for about 8 minutes. During these 8 minutes, we observe the upper drainage channels, kept open during the whole time, to see if any leakage is occurring.

3- After 8 minutes were over, the pump is then set up to increase injection pressure from previous point by 5 bars, hence increasing the net applied stress onto the sample by (40 + 5) bars.

4- When injection pressure was close to piston force of 35 bars, the piston force was then increase by 20 bars by placement of extra dead weight. This process was repeated every time injection water pressure was approached piston force. The maximum force piston could deliver through dead weight was about 10 MPa, or 100 bars. This would restrict our injection pressure to below 100 bars.

5- Point 2 and 3 were repeated until leakage from the lower drainage channels was observed.

During the whole time, volume changes of the hydrated bentonite sample were being registered.

7. Results and Discussion

During the tests executed, injection above 15 bars often resulted in mud being so compressed that it destroyed the filter at the interface and invaded the sand column along specific weak plane(s), as shown in Figure (7.0). These weak planes came about due to anisotropic compaction of sand along these planes. The reason for that is the heterogenic nature of sand which distributes the compressing pressure unevenly in every direction. To coup with this problem, sand was pre-wetted before placement in the pipe and the outlet of the pipe setup was closed. The pressure inside the sand column is no longer atmospheric, and the wet sand will have less anisotropic compaction in addition to reducing the pressure drop previously experience at the mud-sand interface. After this, the chain of events previously occurring far beyond 15 bars, were now more likely to happen around 15 bars.

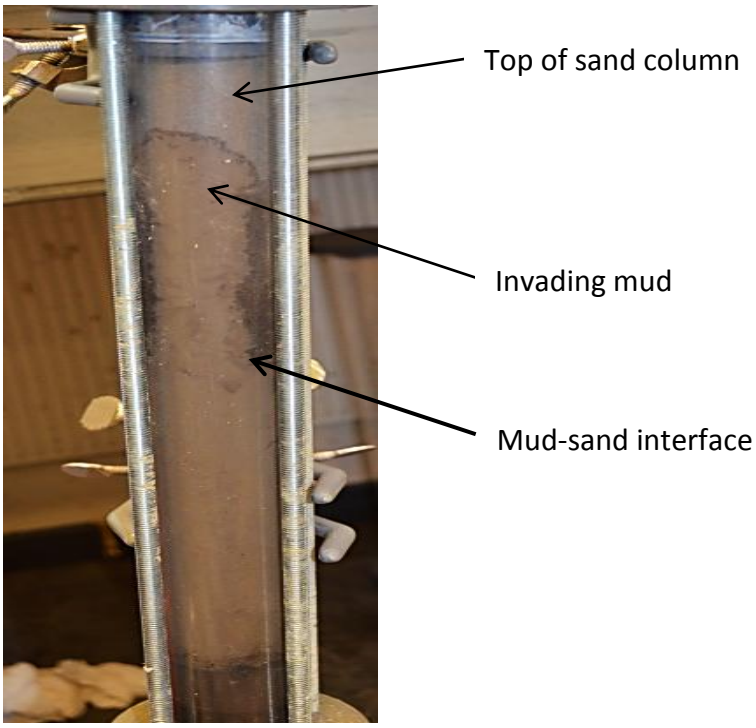

Figure 7.0: Mud invading sand column at pressures above 15 bars. Note, pressure in the sand column is atmospheric

The data collected for every test were converted into graphs represented in Figures (7.4), (7.7), (7.9) and (7.10).

The first thing that happens when water is pressed into the pipe is that the mud column gets compressed (drained), pushed against *and* into the sand column above it. Noticeable decrease in mud column is observed at the same time as water is forming a reservoir of its own as shown in the Figure (7.1).

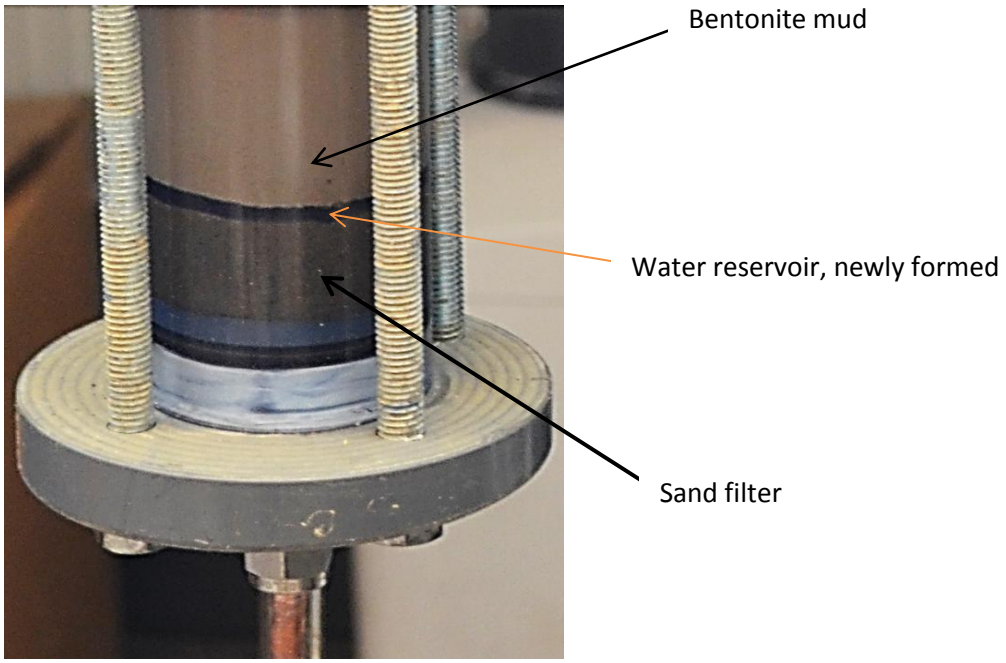

FIGURE 7.1: FORMING OF WATER ZONE. HERE AT 6.5 [BARS]

By now we assume, based on lack of visual evidence, that the additional volume of injected blue water and hence the increased pressure, is not going through the mud but rather build up the water reservoir and further compress or drain the mud column, Figures (7.1) and (7.2).

As we continue this procedure and building up the pressure inside the pipe to higher levels, the water zone increases no more in volume and we see beams of blue water trying to escape the pressurized water reservoir into the mud column, Figure (7.2).

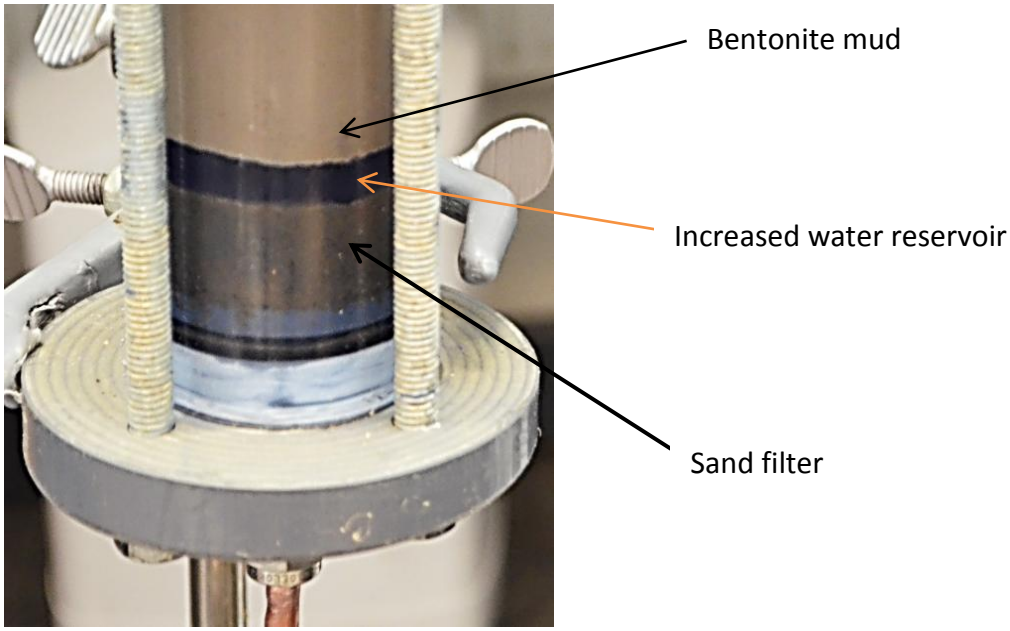

FIGURE 7.2: INCREMENTAL WATER VOLUME AT INCREASED PRESSURES. HERE AT 13 [BARS]

As we clearly see from Figure (7.3) the water beams are not going all the way up across the mud column, at least not that we can see of. It was natural that we tried to experiment with similar but transparent materials, which is the case with Laponite.

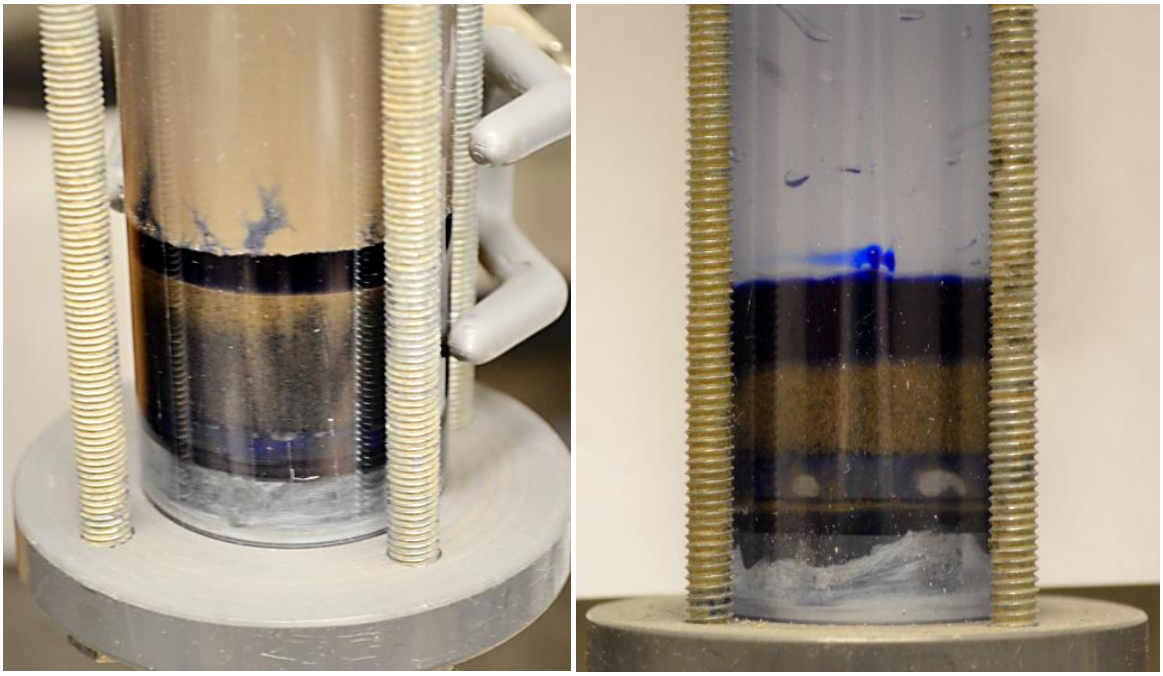

FIGURE 7.3: BLUE WATER BEAMS ESCAPING THE WATER ZONE INTO MUD COLUMN AT HIGH PRESSURES (LEFT), SIMILAR BEHAVIOR WAS FOUND FOR THE CASE OF LAPONITE GEL, BUT AT HIGHER PRESSURES

In the coming sections, we will go through the group of tests executed on bentonite based mud according to the main experiment procedure described in the previous chapter.

7.1 THE UNCLAMPED PIPE TEST

For this test, the clamps were not attached to the pipe and the expansion unrestrained. We start by finding out the magnitude of the expansion experienced when maximum pressure in our pressure range of interest is applied. Calculating the tangential stress on the PVC pipe for maximum pressure applied in this test yields:

$$\sigma_{\text{tang.},pipe} = \frac{p_{water,\max}\left(D_o - t\right)}{2t} = \frac{15\text{ bar}\cdot\left(5\cdot10^{-2} - 4.5\cdot10^{-3}\right)m}{2\cdot\ 4.5\ \cdot10^{-3}m} = 7.58\ MPa$$

where $p_{water,\ max}$ is the maximum pressure introduced into the pipe, D_o is the pipe's outer diameter and *t* is its thickness. When the pressure inside the pipe is at its largest, $p_{water,\ max}$, this induces a radial expansion in the pipe which is calculated as follows:

$$\varepsilon_r = \frac{\sigma_{\text{tang.},tube}}{E_{PVC}}\upsilon_{PVC} = \frac{7.58\cdot10^6}{2500\cdot10^6}0.38 = 0.003$$

where E_{PVC} is the elasticity modulus (Young's modulus) of the PVC pipe, υ_{PVC} is Poisson's ratio for the pipe. The value used for elasticity modulus of PVC pipe is average as the pipe made for the purpose of our test was quite unique. Using the definition of strain ε_r, we can get the radial deformation induced due to the stresses inside the pipe as follows:

$$\varepsilon_r = \frac{\Delta D}{D_{PVC}} \Rightarrow \Delta D = D_{PVC} \cdot \varepsilon_r = 41 \text{ mm} \cdot 0.003 \approx 0.125 \text{ mm}$$

This clearly shows that we get a pipe expansion of 0.125 mm when we reach a pressure of 15 bars inside the pipe. The expansion might be little, but its effect has some significant to it. Since the pressure in the sand column in this test is atmospheric, it is thus assumed that the expansion experienced by pipe is equal to the one in the mud column.

What it could be observed while the test was ongoing was that mud was not going into the sand column for increased pressures. The question that remained was what was actually going on between at the interfaces of mud and sand columns. It was decided that closer look for that area was needed and the pipe was therefore carefully disassembled from the system and the contents were removed gradually starting from the top, where sand column is located. At the interface of the two columns, a thin film, around 3 mm thick, compromising of fine sand grains and mud was found. This film turned out to be a filter created due to mud being pushed against sand.

The filter was effectively prohibiting mud form crossing over to sand column and contributing to seal some of the pressure inside the mud column. What the filter was not sealing was the drainage (compaction) of mud column and the escaping water crossing over to sand column. When the same test was run for lower pressures, the thickness of this filter was found to be smaller; indicating that the filter gets thicker and becomes a more effective sealant as the mud is being pushed harder due to increased pressure, as seen from charted results of this test in Figure (7.4).

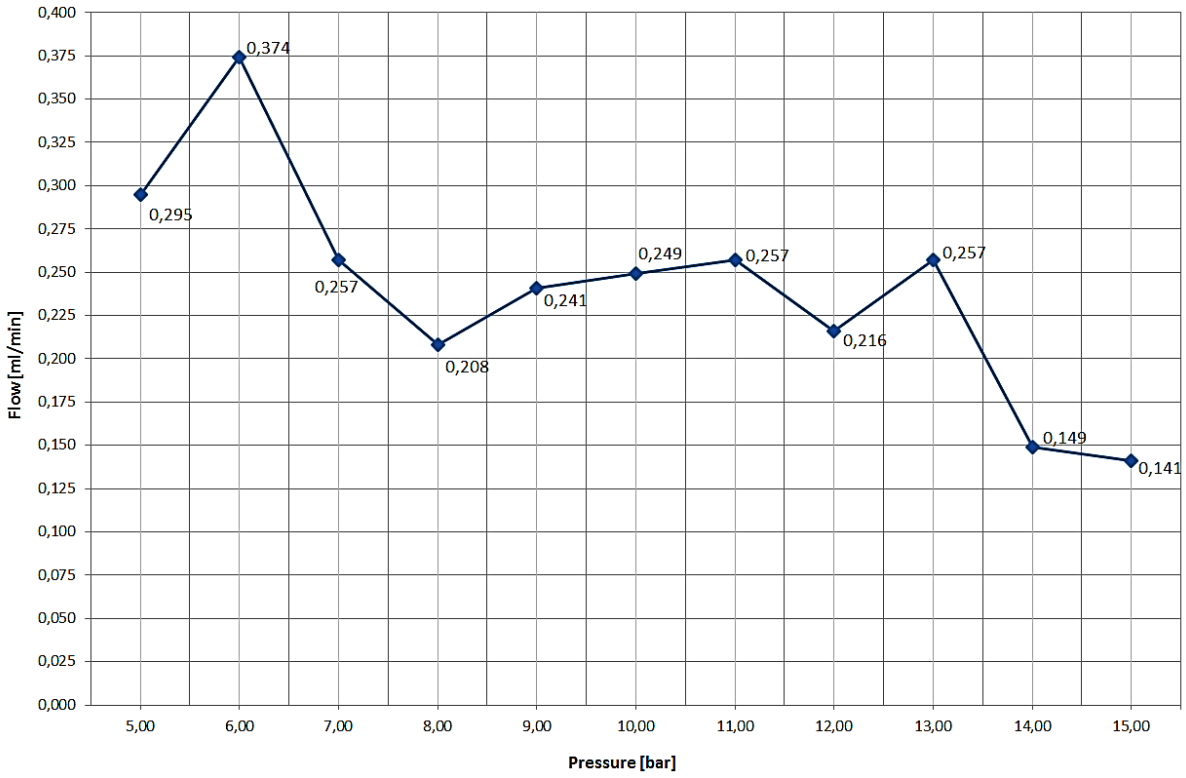

FIGURE 7.4: INJECTION FLOW FOR DIFFERENT PRESSURE RANGES FOR MUD IN A PIPE WITH UNRESTRAINED EXPANSION. NOTE THE MAGNITUDE OF THE DECREASING TREND OF FLOW FROM START TO END.

In addition to the decreasing trend of the flow as one move up the pressure scale in Figure (7.4), frequency of the sharp drops and high peaks witness an unstable compaction and expansion catalyzing formation of weak planes in the column and reducing the shear strength between mud and pipe wall.

These detected weaknesses are instantly employed by the pressurized water reservoir which eventually bleed upward creating beams or channels of blue water extending from the water zone and up between the mud column and inner wall of the pipe ending into the sand column, Figure (7.5). It has to be stated that at this stage it was still unknown whether these beams of blue water were extending inside of the mud or if they were only a thin film moving outside of the mud column.

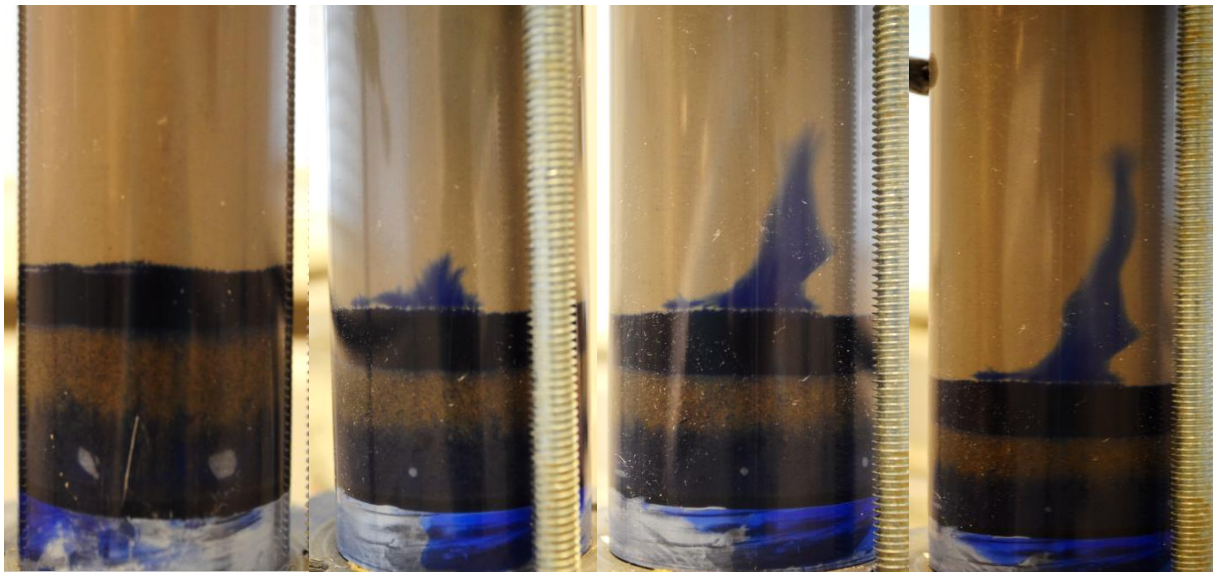

FIGURE 7.5: PROGRESSION OF WATER BEAMS ALONG INNER PIPE WALL AT INCREASING INJECTION PRESSURES

7.2 THE CLAMPED PIPE TEST

In the process of limiting the effect of expansion on creation and propagation of the channels shown in Figure (7.5), two simple hose clamps, Figure (7.6), were used to stop the PVC pipe from expanding. When the test was run the effect of clamps became clearer as we increased the pressure, Figure (7.7).

FIGURE 7.6: HOSE CLAMPS USED TO RESTRAIN THE PVC PIPE EXPANSION

The results of the test run in this case are charted in Figure (7.7). We notice the decreasing trend the flow has as we increase the pressure, just like the one found in the case of unclamped pipe. For the sake of comparison between clamped and unclamped pipe, the effect of expansion restraining is seen in lower flow rates for lower pressures and a decreased overall disturbance in flow rates changes.

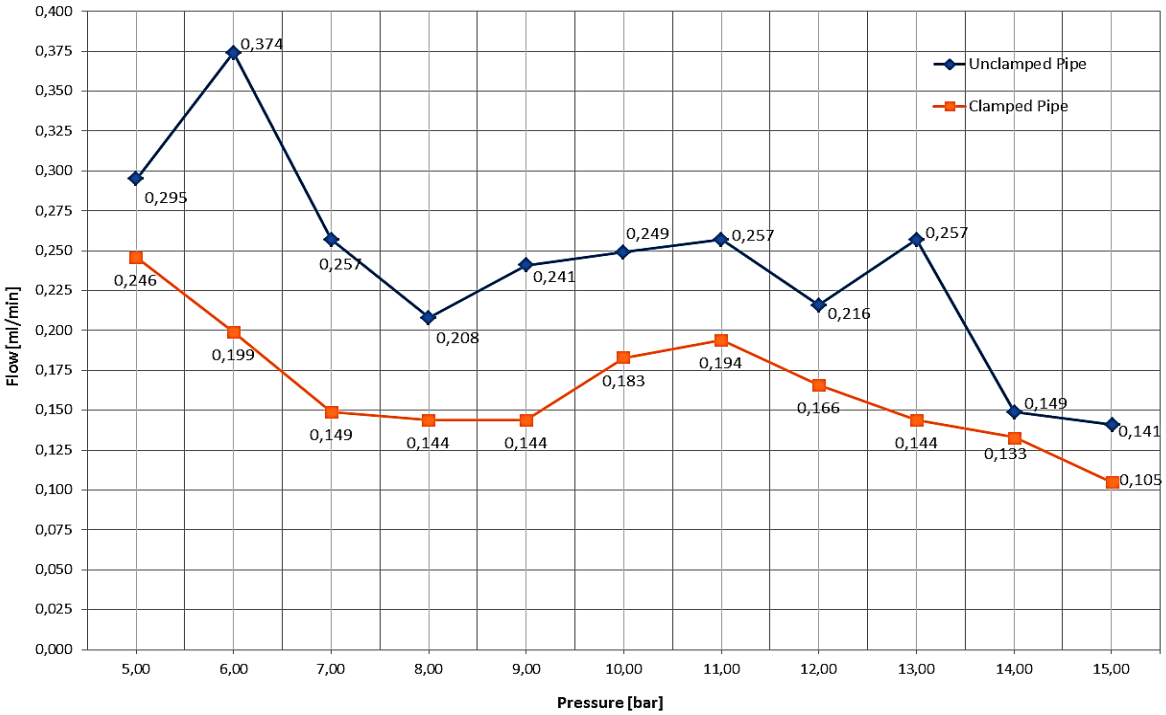

FIGURE 7.7: INJECTION FLOW FOR DIFFERENT PRESSURE RANGES FOR THE CASE OF MUD IN THE PIPE WITH RESTRAINED AND UNRESTRAINED EXPANSION. NOTICE THE DIFFERENCE IN MAGNITUDE OF FLOW AND THE OVERALL STABLE FLUCTUATION IN FLOW RATE FOR CLAMPED PIPE COMPARED TO UNCLAMPED PIPE.

So far we have accounted for the effect of mud expansion on the creation and propagation of the previously mentioned channels. In the next tests, we will try to account for the effect compaction have on these channels.

7.3 DRAINED MUD TEST WITH NO CLAMPS ATTACHED

The draining setup for this case is shown in Figure (7.8). As we see from the figure mud is placed into a pipe and have some sand on both ends before placing a plug on both ends. The sand catches the water escaping the mud and, as seen from figure, is getting saturated with water as we compress the plugs harder against each other. For about one hour, a compressing pressure of 60 bars was applied on the plugs.

Afterwards, the sand in this pipe was replaced with dry sand to detect any drainage from the mud column when the test is run, and the pipe was then assembled into the setup described in Figure (6.3) and (6.11).

The results obtained from this test are charted in Figure (7.9). One can observe that in the case of drained mud, light blue line, we have general decreasing trend for injection flow throughout the test, a trend that is observed for the other lines as well. However, there is a difference related to the light blue line, for it has a more rapid decrease than the other two lines.

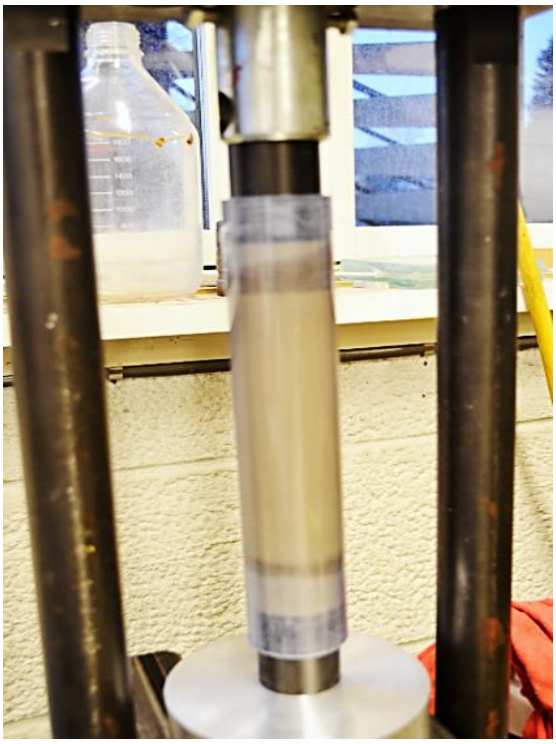

FIGURE 7.8: THE MUD INSIDE PIPE IN A MECHANICAL COMPRESSOR. NOTICE THE WATER DRAINING FROM BENTONITE MUD AND INTO SAND FILTER AT BOTH ENDS OF THE PIPE.

This means that it compresses more for the same pressure range, which is in according with the poroelastic theory (chapter 4), since water would impart extra stiffness to the material, and without it this extra stiffness is lost.

In the next experiment we will test the significance of attaching a clamp to the pipe containing mechanically drained mud.

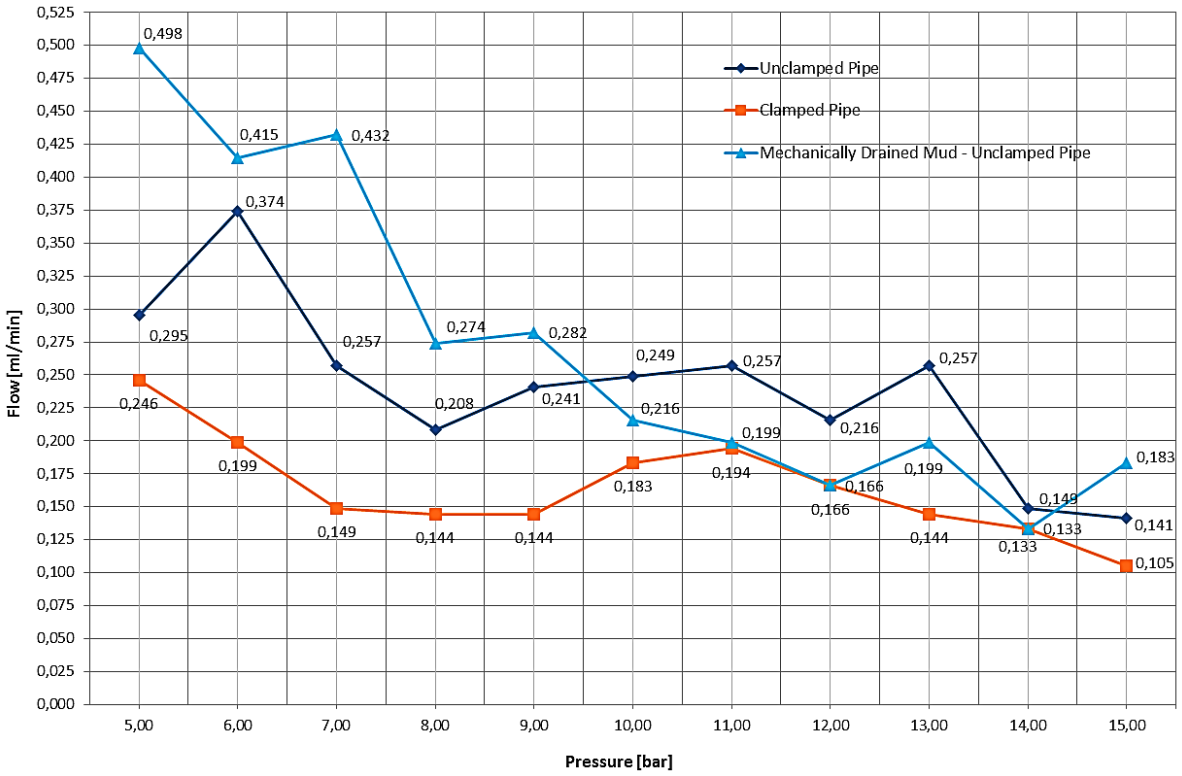

FIGURE 7.9: INJECTION FLOW FOR DIFFERENT PRESSURE RANGES FOR THE CASE OF MECHANICALLY DRAINED MUD WITH UNRESTRAINED EXPANSION [LIGHT BLUE LINE]. NOTICE THE HUGE DIFFERENCE IN FLOW RATES AT START AND END OF PRESSURE SCALE.

7.4 DRAINED MUD TEST WITH ATTACHED CLAMPS

If we make a comparison of drained mud for the cases of restrained and unrestrained pipe expansion; light blue and light green lines in Figure (7.10), we see that the light green line is translated downward compared with the light blue line, suggesting smaller flow rates for the former case. The decreasing trend though is more prominent for the light blue line as its expansion is unrestrained, while that of the light green light is less conspicuous pointing to less compaction and less expansion due to the smaller water content and the restrains attached.

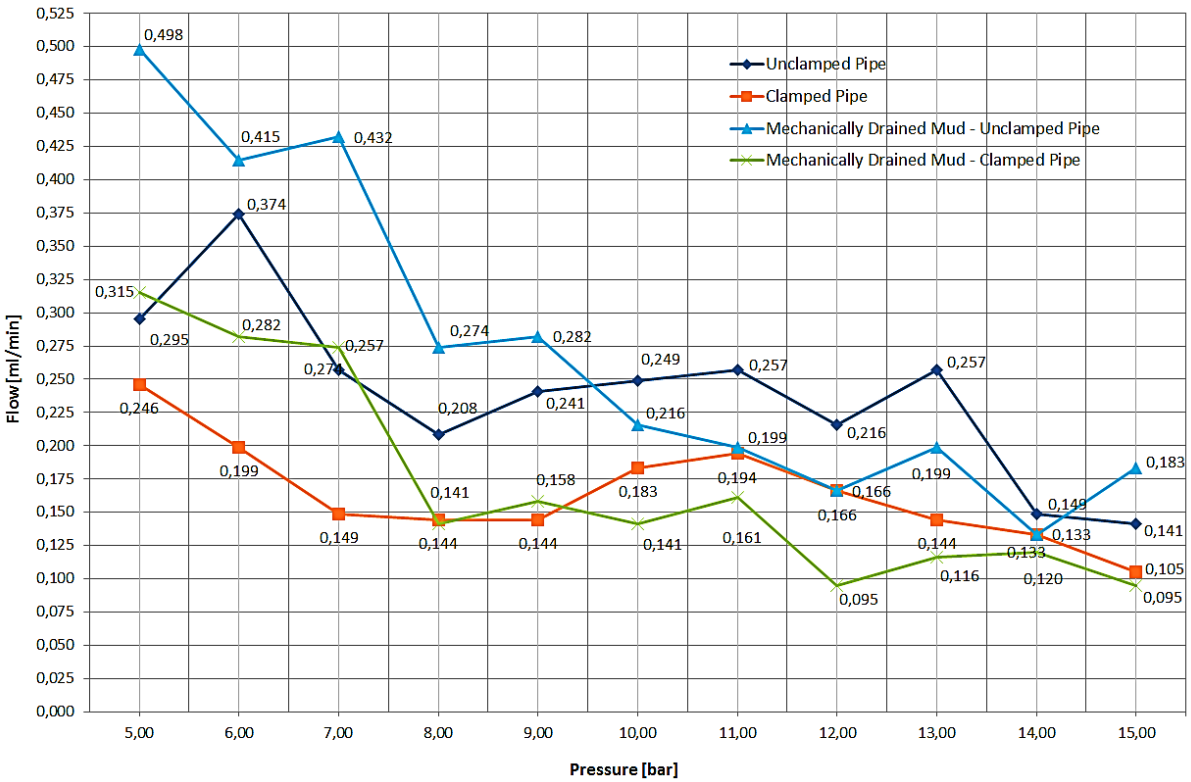

FIGURE 7.10: INJECTION FLOW FOR DIFFERENT PRESSURE RANGES FOR THE CASE OF MECHANICALLY DRAINED MUD WITH RESTRAINED EXPANSION [LIGHT GREEN LINE]. THE SMOOTH AND SUBTLE CHANGES IN FLOW RATES FOR THE LIGHT GREEN LINE REMIND US OF THE ORANGE LINE.

The compression of the drained mud where the clamps are used is obviously less than the same mud with no clamps attached. Comparison of the two groups of tests; dark blue-orange and light blue-green, the effect of clamps is clearly seen as a reduction of compression for both cases. This is in good accordance with equation (4.31) described previously as:

$$c_{bu} = \left(\frac{\varepsilon_b}{p_c} \right)_{undrained} = c_{bc} - \frac{c_{bp}\, c_{pc}}{c_{pp} + c_f}$$

As we see from the last term in the equation above, the pore fluid compressibility, c_f, has an increasing effect on the bulk compressibility of the system. This implies larger resistance against deformation for the case of *undrained* mud compared to drained mud.

In all of these tests and in particular in the test of drained mud with restrained pipe expansion, we eventually reach a point where the mud compression lowers the shear strength between mud column and pipe wall and we start observing the distinctive beams shown in Figures (7.3) and (7.5).

The transporting mechanism for water *through* the mud, however, was still unknown at that stage, mainly because our knowledge was limited to our observations. In other words, these observations did not provide us with what was happening inside of the mud after the development of the blue water beams. We needed desperately to observe what was going on inside of the mud to confirm our theories. This will be discussed in the next section.

7.5 Experimenting on Laponite Gel

To help us get a better understanding of transporting mechanism of fluids through the mud, and since our mud exhibits properties of a Bingham fluid, we started exploring the use of other transparent Bingham fluids. For further study of properties for Bingham and other fluids, the reader is referred to Appendix (A-2). Two materials were taken into consideration; gelatin and Laponite (in gel form). As Laponite constitute a more valid candidate to represent bentonite, both in terms of structure and composition, touched upon previously in chapter six, it has been given our prime attention.

Here, what interests us is to see the nature of fluid propagation inside the gel, and not the pressures at which this propagation is happening, since we already have this information for our bentonite mud.

The exact same tests conducted on bentonite mud were performed on Laponite gel. The only difference was that the outlet on located on the upper cap of the PVC pipe, as described in Figure (6.1), was closed. This means that the pressure in the sand column will no longer be atmospheric. The reason for closing the outlet is that when preliminary tests were performed on Laponite gel, the water pushed the gel through the sand column and out through the outlet and no filters developed at the gel-sand interface.

To ensure that gel column is static and not being pushed into sand column, the sand was pre-wetted with water and outlet was closed, as described earlier. Then water was pumped into the pipe and soon afterwards, the gel started exhibiting similar behavior to bentonite mud.

The Laponite gel was still being compressed due to its elastic nature, and we had a free water zone here as well. For the same volume of mud and Laponite gel, we had a larger free water zone for the case of Laponite gel, indicating that the material is more elastic than our bentonite mud; nevertheless, beams of blue water soon started developing, as shown in Figures (7.11) and (7.12).

Observing Figure (7.11), the beam, to begin with, is making its way upward between gel and inner wall of the pipe. Around the center of the figure, the beam then shifts its path and start propagating radially into the gel. Now, if the gel was not transparent, we would not be able to see this shift in direction, which is exactly the case in our bentonite mud. Any extra injection of water at this point will contribute to strengthen this propagation further into the gel; this is shown in Figure (7.12).

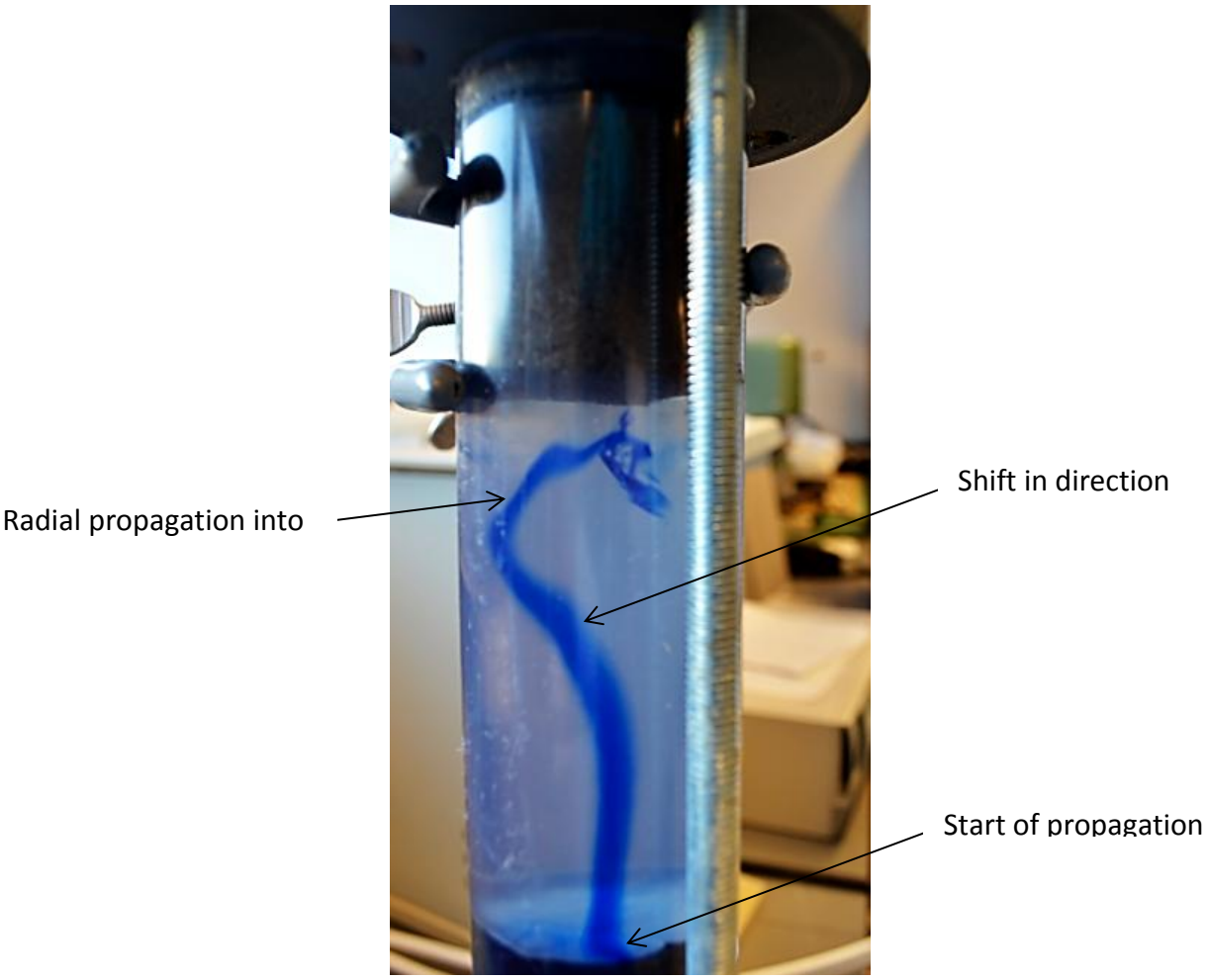

FIGURE 7.11: PROPAGATION OF WATER BEAM IN LAPONITE GEL. IT STARTS VERTICALLY RIGHT UPWARD LIMITING ITSELF TO A THIN FILM MOVING IN THE AREA BETWEEN GEL AND INNER PIPE WALL, THEN CHANGES THE COURSE AND PROPAGATES RADIALLY INTO GEL.

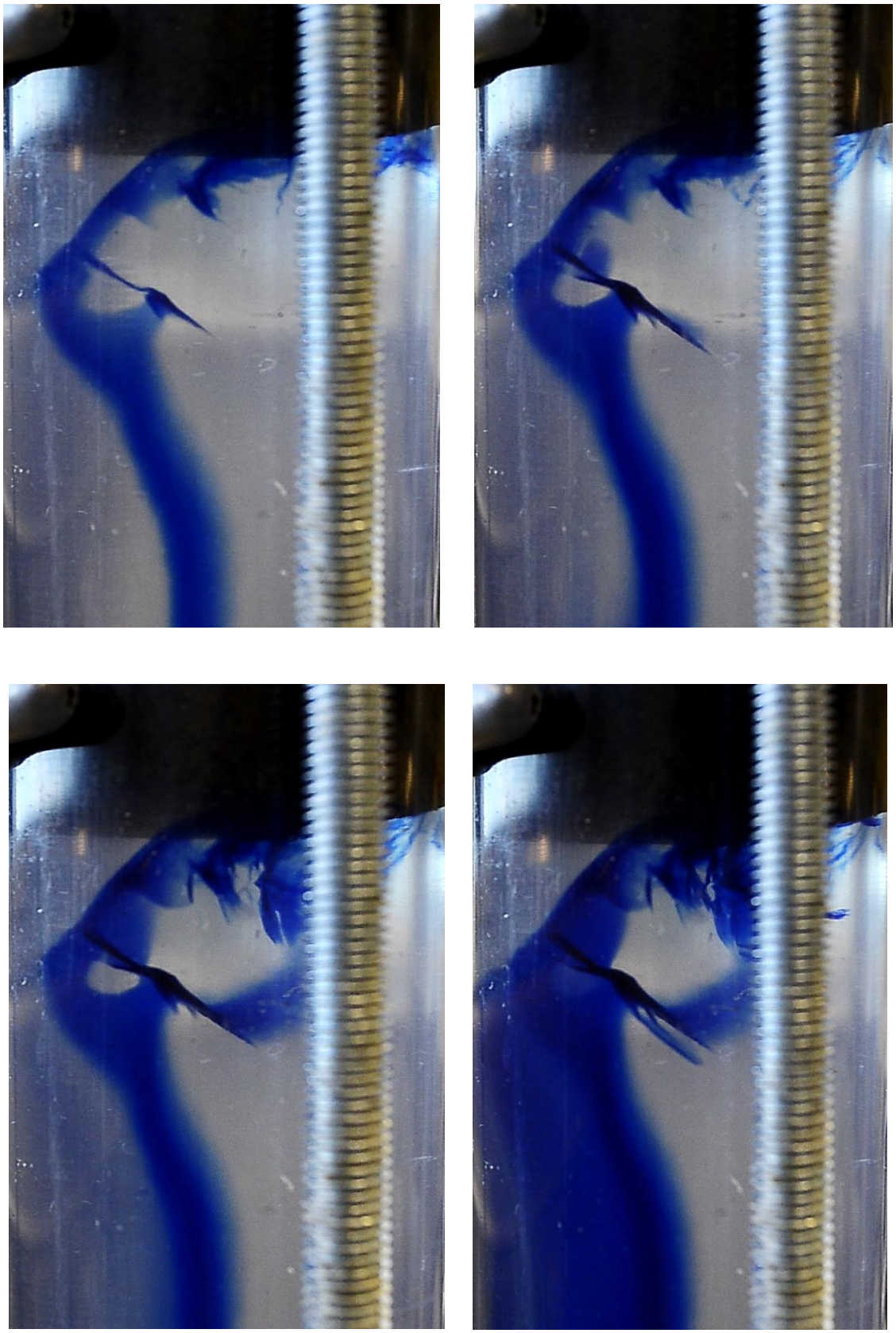

FIGURE 7.12: WATER PROPAGATING INTO GEL AT INCREASING PRESSURES FROM FIGURE (7.11). PROGRESSION STARTS FROM TOP LEFT TO BOTTOM RIGHT. NOTICE THE DIFFERENT PLANES WATER IS PROPAGATING THROUGH THE GEL AT.

7.6 EXPERIMENTING ON BARITE

Two sets of experiments were done using barite instead of bentonite mud. In the first set, dry powdered barite was put in the pipe in similar manner to bentonite mud. Blue water was injected and powdered barite start getting partially wet. At relatively low pressures of around 5 bars, beams of blue water were observed escaping between the partially wet barite column and inner wall of the pipe continuing upward toward the sand column. After using clamps to limit the effect of pipe expansion on the creation of these beams, the results remained comparatively unchanged as the beams were observed around 5 bars for the case of clamped pipe as well.

Barite in the second set of experiment was mixed with water in a mixer. The water with the dissolved barite was then poured into the pipe according to the arrangement described in Figure (6.1) where water mixed with barite was placed on top of the sand filter and let for some days so barite particles could settle to the bottom (barite sagging). After some days barite had settled to the bottom on top of sand filter forming its own column. The water on top of this barite column was then removed and sand was poured onto the barite column. After injection of water and around 5 bars of pressure inside the pipe, the distinctive blue water beams were then observed escaping between the sagged barite column and inner wall of the pipe. As for the first set of barite experiment, use of clamps did not have any noticeable effect on the pressure at which these blue water beams start occurring.

These set of tests are an indication to the fact that sagged barite do not constitute an impermeable plug in the face of pressing water, as the water easily follows up the already established route of the water inside the sagged (wet) barite, especially at the outer peripheries between the barite column and pipe.

FIGURE 7.13: WATER, BLUE, TRANSPORTING THROUGH SAGGED BARITE IN PVC PIPE. NOTICE THAT WATER IS NOT INITIALLY TRANSPORTING BETWEEN BARITE COLUMN AND INNER PIPE WALL, BUT RATHER RIGHT THROUGH IT.

7.7 EXPERIMENTING ON HYDRATED AND COMPACTED BENTONITE

The primary aim of this experiment was to investigate use of hydrated bentonite for well plugging purposes. The sample of hydrated bentonite was put into the special Oedometer Figure (6.4), and compression force was applied for about two weeks. During this period the original volume of sample was compacted and water allowed to be drained out of it through four different channels, as previously described.

After two weeks, and due to time limitations, the Oedometer was connected, through one of its bottom drainage channels, to a constant pressure/flow rate-delivery pump injecting blue colored water. The injected water would then first go through a steel filter located underneath bentonite sample inside sample holder, Figure (6.5). In such a way, the water will be distributed evenly to face bentonite sample placed on top of filter. The hydrated and compacted (drained) bentonite sample at the start of injection process and end of pure compaction period (2 weeks, no water was injected into sample holder, the sample was allowed to drain in this period) had a height of 13.61 mm, suggesting a net compacted sample volume of 52.228×10^3 mm^3. Keep in mind that the overall sample volume to be compacted, including the extra added volume when the lever was leveled with ground, was 305.123×10^3 mm^3(converting this volume into height by diving it with sample holder area, we get a total pre-drained sample height of 79.511 mm!) The sample had clearly been compacted by a factor of 83% of its original volume (water). Figure (7.14) shows the final compacted sample volume (disk) at end of testing.

FIGURE 7.14: THE SAMPLE, AT THE END OF TESTING. THE UPPER LEFT PICTURE SHOWS THE SAMPLE AS IT WAS IN THE HOLDER, THE DAMAGES SEEN ON THE PICTURE UPPER RIGHT COMES SOLELY FROM THE OPERATION OF GETTING THE SAMPLE OUT OF ITS HOLDER. NOTICE THE BRIGHT GREEN COLOR. NO TRACES OF BLUE WATER GOING THROUGH IT, AS CONFIRMED BY NO WATER PRODUCTION FROM THE DRAINAGE CHANNELS DURING THE WHOLE INJECTION PERIOD (32 HOURS).

The pump was set to constant delivery of pressure for periods of time of our interest. This time varied from 8 minutes to a maximum of 15 minutes, due to the tight time schedule at hand. The cumulative water injected into sample holder and the corresponding injection pressures for the entire period is shown in Figures (7.15) and (7.16).

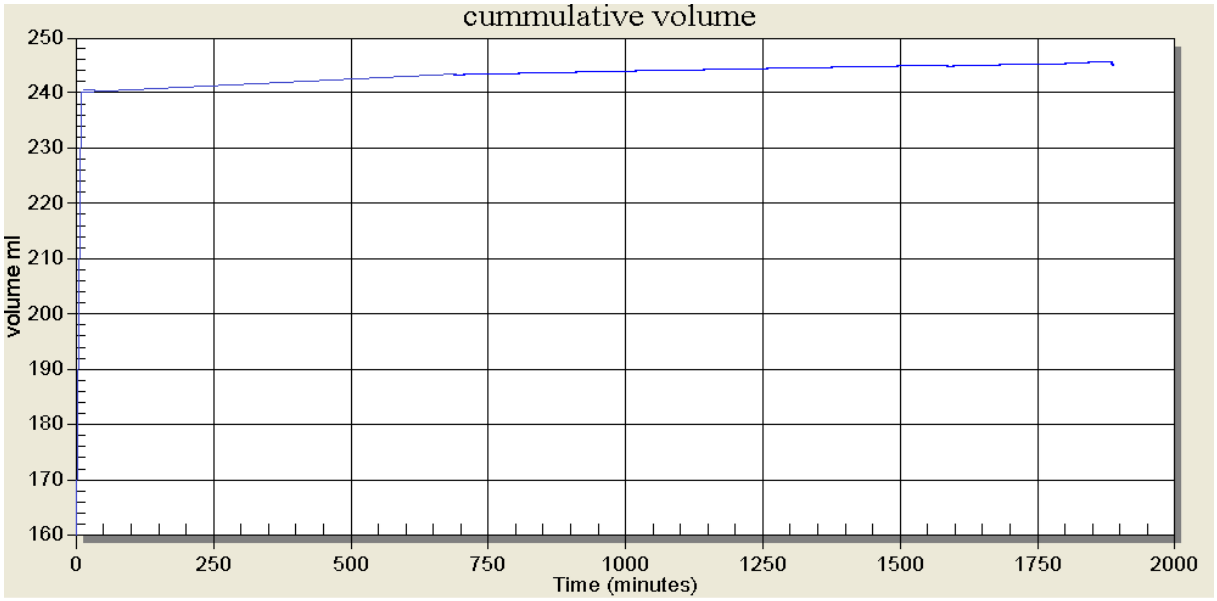

FIGURE 7.15: THE CUMULATIVE WATER INJECTED FOR THE DURATION OF THE TEST, 32 HOURS. DURING THE FIRST FEW MINUTES, PUMP WAS STARTED AND WATER RUN THROUGH PIPE TO REMOVE AIR FROM PIPING PRIOR TO INJECTION INTO SAMPLE HOLDER. THE INJECTION PROCESS STARTS FROM 240 ML AND ONWARD.

After cleaning of connection piping between pump and Oedometer, water, starting from 240 ml in the figure, was injected into sample holder from below. The piston, located on top of sample holder, was always delivering a positive net force greater than injection pressure. From Figure (7.15) we notice the gradual increase in the cumulative injected water, reaching up to a maximum of 7 ml. In terms of height of water level pushing compacted bentonite sample inside the sample holder:

$$h_w = \frac{7\ ml \cdot 1000 \frac{mm^3}{ml}}{\pi \left(\frac{69.9}{2}\right)^2 mm^2} = 1.824\ mm$$

The free water zone is thus 1.824 mm thick. This thickness is though less than that of the steel filters (3 mm) located on top and bottom of bentonite. This implies that during these 32 hours, water never had its own free zone, as compared to Figures (7.1) and (7.2). More time and testing for longer range of time are needed in order to make a final interpretation. However, the preliminary result we have so far suggests the followings:

- The compacted sample of hydrated bentonite under a piston force effectively 100 bars (applied on top of sample) and a net water injection pressure of 97 bars (coming from under sample) did prevent water from passing by it in every manner: channeling and or fracturing.

- The compacted “disk” bentonite shown in Figure (7.14), was quite elastic, suggesting that the axial stresses applied on it were being sufficiently transmitted radially and prevented water from forming beams similar to those shown in Figure (7.5).

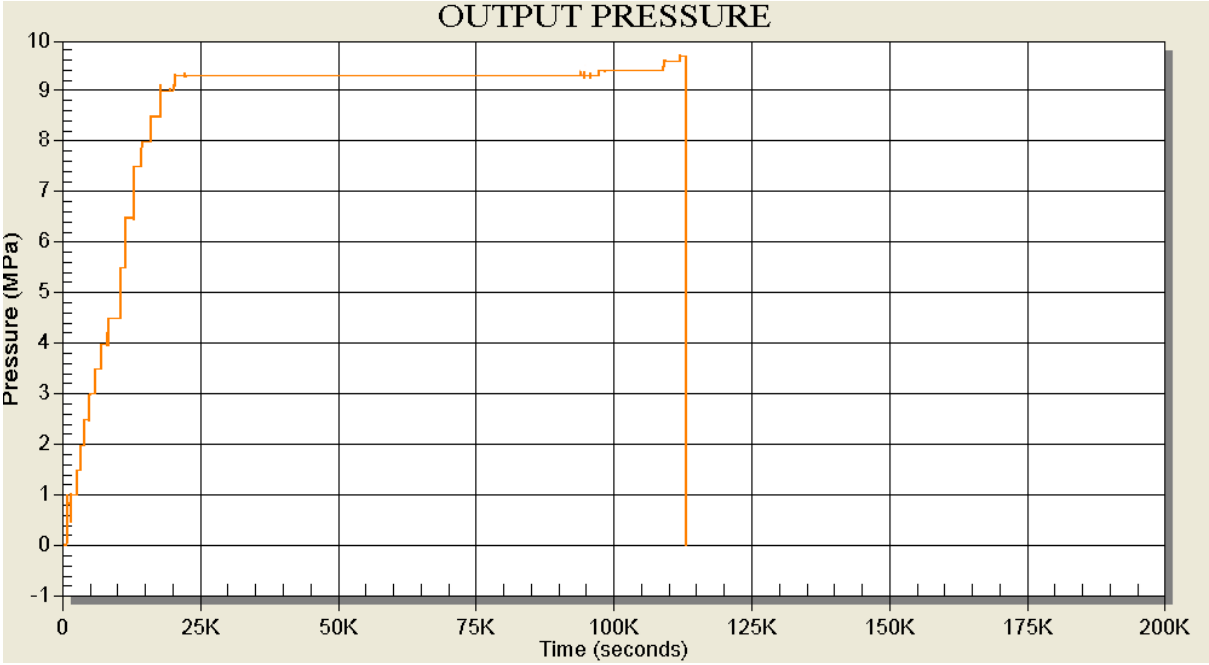

FIGURE 7.16: OUTPUT PRESSURE FROM THE PUMP DELIVERING CONSTANT PRESSURE. THE STEPPING EFFECT OBSERVED IS THE PROCESS WHERE INJECTION PRESSURE AND NET PISTON FORCE WERE EQUALIZING AND THEN MORE DEAD WEIGHT WAS BEING PLACED ON LEVER THUS INCREASING NET PISTON FORCE. AFTER THIS WAS DONE, INJECTION PRESSURE FROM PUMP WAS THEN INCREASED AND SAME PROCESS REPEATED ALL THE WAY UNTIL 10 MPA. THE LINE HEADING STRAIGHT DOWN AT END OF INJECTION WAS WHEN THE PUMP WAS STOPPED AND TEST TERMINATED.

Now we will go through some of the figures, trying to explain how the test was conducted and how the sample reacted to various conditions.

Figure (7.17) shows the compaction of the very fast filling of the sample holder. We notice the three Linear Variable Differential Transformers (LVDT), monitor the compaction in different parts of sample surface. Here we can consider the Z1 in the figure as a good average for the compaction of the sample during the time period.

The sample in Figure (7.17) is being compacted by a constant piston force of 35 bars. Notice the “tales-”part of the lines flattening out at the end, not because the sample cannot be compacted any more, but because the lever carrying the dead weights is touching the ground. This prompts a refilling process where the additional hydrated bentonite is poured on top of “compressed” bentonite in sample holder. The process of compaction is yet again assumed. The flattening tales in Figure (7.17) would have an abrupt decline (de-compaction), eventually stopping somewhere x-axis. The compaction is then repeated, now with a similar graph as previously, but with the different lines having much flatter “head-”part indicating slower compaction. Unfortunately, due to a data crash for the computer receiving compaction data, valuable information has been lost, and some key figures are not available.

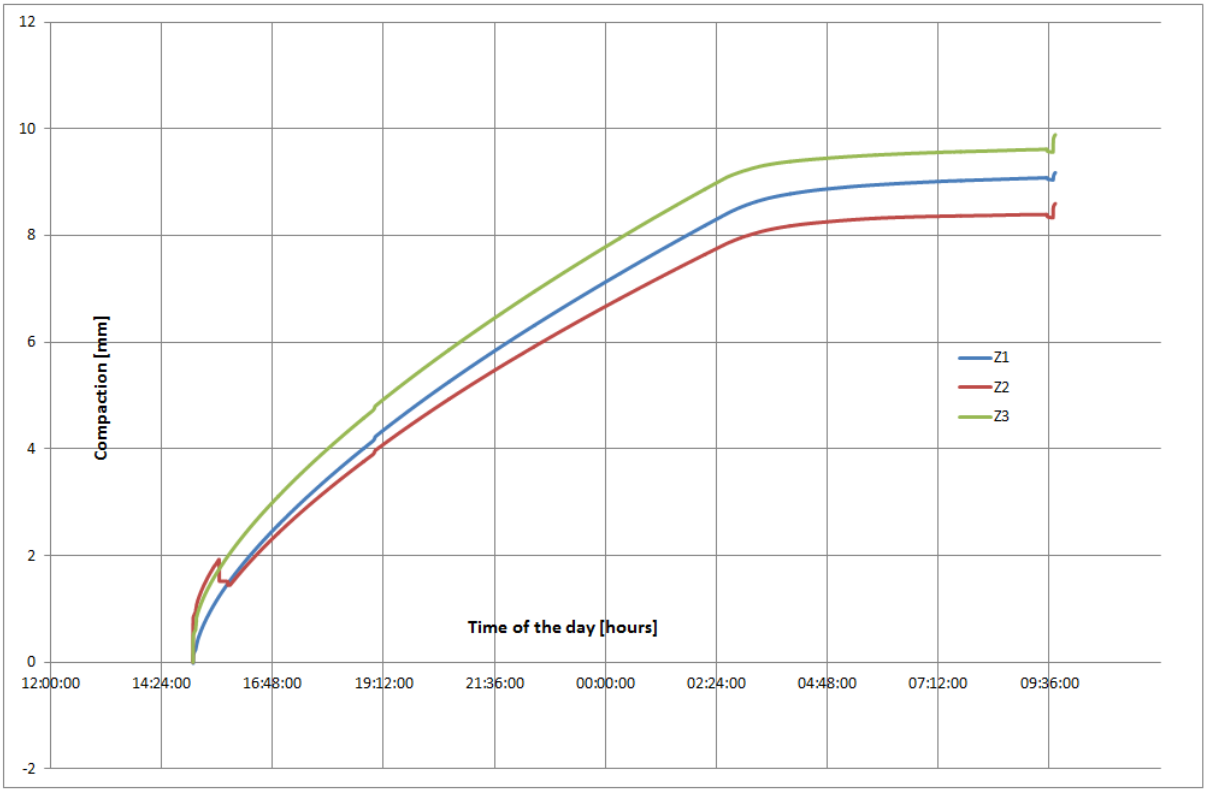

FIGURE 7.17: FIGURE SHOWS COMPACTION OF FOR THE VERY FIRST HOURS OF BENTONITE COMPACTION. THE VERTICAL AXIS HAS BEEN CALIBRATED TO SHOW ACTUAL COMPACTION IN [MM]. THE THREE DIFFERENT LINES ARE COMBINED TO GIVE AN OVERALL AVERAGE OF THE COMPACTION UNDERGONE BY SAMPLE IN THREE DIFFERENT DIRECTIONS. COMPACTION HERE HAS BEEN CONVERTED TO INDICATE POSITIVE VALUES. NOTE, THE FIGURE IS FOR THE CASE OF PURE COMPACTION, NO WATER HAS BEEN INJECTED SO FAR.

We now jump forward to the situation where the bentonite sample is subjected to water pressure from below. The piston force on top is still there and has not changed, yet. Figure (7.18) shows the last stages of the compaction/injection process on our bentonite sample. The very first different thing with this figure, compared to Figure (7.17), is that compaction data are taken directly from the monitoring software and not calibrated.

As we inject water into sample holder, logically, the overall volume inside of sample holder will increase accordingly. This increase in volume is translated by LVDT devices as de-compaction of bentonite sample. Figure (7.18) shows this effect clearly at the end of Z1, Z2 and Z3. The effect is seen as decrease in negative values. As injection pressure approaches the magnitude of piston force we increase the latter by applying more dead weights. The effect of applying extra piston force on bentonite sample while water injection pressure is kept constant is that the sample will undergo a compaction process, Figure (7.17), and in case of Figure (7.18) an increase in negative values.

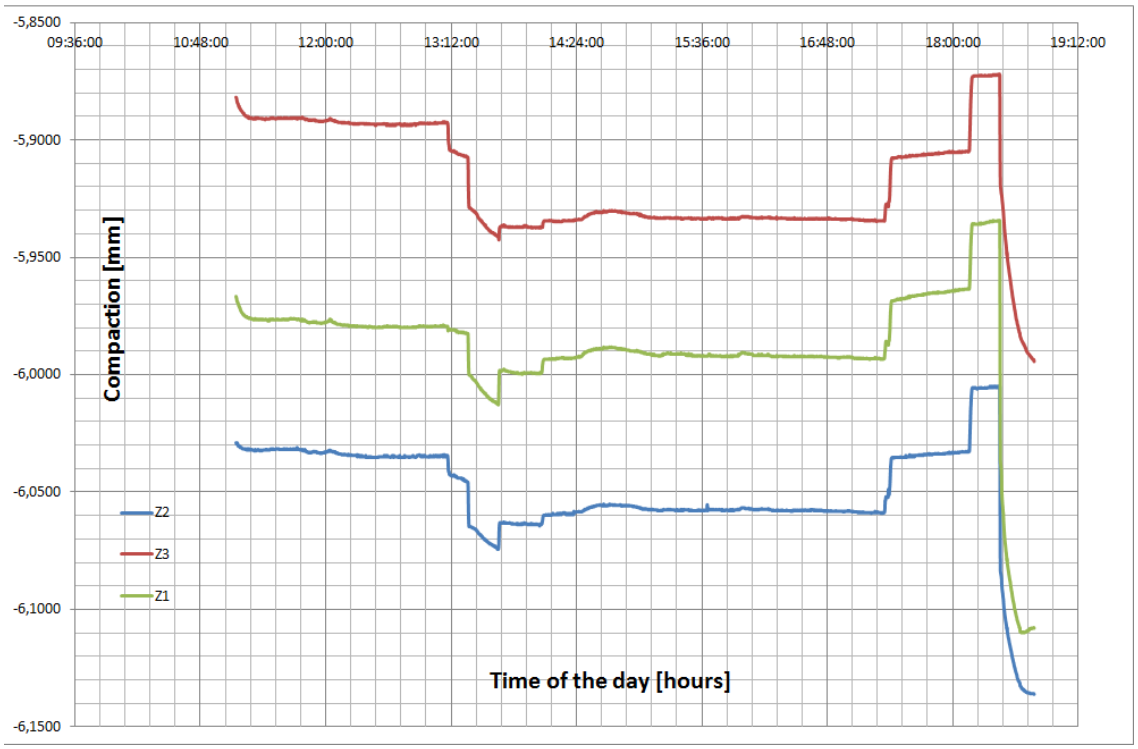

FIGURE 7.18: REACTION OF COMPACTED BENTONITE SAMPLE CAUGHT IN BETWEEN PISTON FORCE STRESS ON ONE SIDE AND INJECTION PRESSURES ON THE OTHER. COMPACTION IS NEGATIVE. NOTICE THE DECLINING TREND AT START OF THE LINES DUE TO INCREASE IN PISTON FORCE. THE COMPACTION LEVELS OUT AND FURTHER INCREASE IN PISTON FORCE IS APPLIED; INDUCING FURTHER COMPACTION. THE SMALL DECREES IN NEGATIVE VALUES IN THE MIDDLE OF THE FIGURE ARE DUE TO INCREASE OF INJECTION PRESSURE.

7.8 THEORY APPLICATION

The theory describing the mechanism of fluid transport through porous media, at the early stages of experimenting, attributed fluid displacement in mud to its permeability. Extensive preliminary trial and error testing was done to find some validity to this theory. Consequently, the testing setup and materials have been in constant improvement in order to make the outcome more reliable. Improvement like the use of a “Ruska” pump where the injected volume of water could more accurately be determined and the use of colored water to detect any channeling alongside the pipe wall contributed to mature our understanding of the process involved.

After careful investigation of mud in countless of tests, there were found no blue traces inside it, this proved under the circumstances that water is not going into mud taking the way of its inter-connected pores.

Bentonite mud under pressure from the water reservoir was undergoing a process of drainage. The mud was getting more and more compacted. The injection flow of water and the creation and buildup of water reservoir was a clear indication of the compaction.

Observations of the behavior of Bentonite mud for pressures above 15-20 bars made the mud invade the sand columns above, as shown in Figure (7.0).

Disproving the initial theory led to another series of trial and error testing, this time using an auxiliary material, Laponite gel, to show the possible mechanism of water displacement inside the mud after the creation of blue water beams. For Laponite gel, the bubbles of air (pores filled with air) inside gel were getting smaller as water reservoir was being provoked and gel compressed leading to beams of blue water similar to those induced in the case of bentonite mud. The blue water beams continued between the gel column and inner pipe wall reaching up to the sand column. Carrying on with injection process, other blue water beams with base in the original "vertical" beams started propagating radially into the gel column as shown in Figure (7.11) and (7.12). The beams were spreading into gel in an explosive manner that did not resemble pore-to-pore theory; it reminded more of a hydraulic fracturing.

The mechanical deformation of the material, in our case gel/bentonite mud, is coupled to the pore fluid (air in case of gel) pressure. This is the very essence of the poroelastic theory described throughout chapter 4 and the reason behind the hydraulic fracturing in our gel which in turn represents a window to what happens in our bentonite mud. The water reservoir applies a pressure to elastic gel that in turn transmits this pressure to reduce the volume of the pores thus compressing the gas (air) and increasing pore pressure. The magnitude ratio of the applied stress on the mud to the stress transmitted to the pores is depicted by Terzaghi's effective stress and Equation (4.68). Equation (4.68) defined as ($\sigma_p' = \sigma_p - \alpha p_f$) tell us that the stress applied, σ_p, onto the mud is carried by the mud's framework by an amount of σ_p', while the pore content is carrying a stress amount of αp_f. Biot's effective stress coefficient α, Equation (4.69), enables us to take into account the nature of the bulk modulus at work in our case.

As the stress amount carried by the pore fluid, αp_f, is increasing, the effective stress carried by mud framework σ_p' is decreasing representing a translation of all stress circles, in the context of a Mohr diagram, to the left and closer to the failure line, Figure (5.6). Eventually, the effective stress will cross zero and become negative, meaning that the stresses carried by pore fluid are bigger than that carried by mud framework. At the same moment the effective stress is being negative, the criterion for the criterion for hydraulic fracturing described in Equation (5.3), is met and the pore fluid fractures the mud along its weak plane(s) and find its way out of the material, Figures (7.11-7.12).

The magnitude of stress that the mud framework can carry varies according to its compaction, i.e. pore water drainage, which in return contributes to makes the bentonite mud a more consolidated mass withstanding larger compressive pressures. A test to confirm this was done on a sample of hydrated bentonite in placed in Oedometer shown in figure (6.4). The manner in which compacted bentonite reacts to invading water, according to our preliminary experiment, that the sample becomes more and more resilient to stresses the

more compacted it gets. This is due to decrease in its bulk compressibility which may suggest that the effective stresses inside bentonite are less and less affected by total stresses applied onto bentonite. As the stresses inside bentonite (i.e. pore pressure) become less affected by total confining or compressive stresses, the effective stress expressed in equations (4.68) and (5.2) will remain positive for longer. We now that as long the effective stress is positive, criterion for hydraulic fracturing expressed in equations (5.3) and (5.5) will not be met and water will not penetrate bentonite sample. The solid framework of the drained bentonite carried larger portion of the total compressive stresses for longer times compared to the portion of stress carried by its draining pore fluid.

In conclusion, the different tests performed on bentonite mud confirm to great extent the effect of a single factor on the sealing properties of the mud. Mechanically, this factor is brought about by increasing the mud's resistance to uniform compression, also known as bulk modulus. This is done by draining as much water from the mud as possible. In the lab, the drainage process was done by placing mud between two filters in a sealed device and a compression force was then applied. In the field, the mechanical force could be achieved by placing a long enough column of sand and granular material on top of bentonite mud. This will ensure that net effective stress inside the mud defined in equation (4.68), will always remain positive and clear of the tensile strength criterion for hydraulic fracturing defined in equation (5.3). Physically, this means that the mechanical pressure induced by the force of sand and granular column on top of mud, will always be larger than the pressure of the formation fluids below the mud trying to pass through bentonite mud. Bentonite mud in this process is therefore transformed into a plug that only becomes more effective as it gets more compacted with time, given constant formation fluid pressure, as confirmed by Oedometer test for the case of hydrated bentonite.

7.9 Methods and Limitations

Throughout the various experiments, a great attention has been paid to find and adjust any source of errors during the testing period. Nevertheless, there were some factors that could not be compensated for. The first one is related to the way the pump was working. As indicated in the previous chapters, one of the facilitating reasons for creation of the blue water beams between the mud column and inner wall of the pipe was the reduction of shear strength between mud and inner wall of pipe due to movements; compression and expansion, of the mud. However, as the pump needed refill for injection of every 10 ml, this created a pulse effect in the pressure inside the pipe which contributed to slightly move the mud column up and down.

The second factor that contributed to is the roughness of the inner walls of the pipe. There were used several PVC pipes in turn for the different experiment, some of them were new with smooth inner walls, while the other have been used ones that had some roughness due

to sand contact. We assume that the roughness of the walls have an effect on the shear strength between mud and wall.

The third factor is found in the mud itself. Mud was made in relatively large amounts and held in a bucket. On a regular basis, there were several days between one test and another. The mud in the bucket would then become thicker as some of its water would evaporate over time. Mud containing less water, high viscosity, would naturally have larger resistance against compression, resulting in occurrence of blue water beams at higher pressure values compared to the case of freshly made, lower viscosity, mud.

Other source of errors that could be counted are related to pressure sensors used for the different tests, some of them less sensitive to low pressures; up to 5 bars, and had maximum pressure reading of 60 bars, while other were more sensitive, but had low maximum pressure readings of 10 bars. Additionally, the human error should be counted as a source of uncertainty, though each test has been repeated on average three times to confirm possible trends and results.

Sources of error related to Oedometer are that calibration of the LVDT monitors were done manually and the precision to three digits accuracy not applicable. One of the drainage channels had a small metal particle in it and could block the passage of escaping water, although this had been cleaned, it was not as good as the rest of the channels. At the very end of the testing, we had a very unfortunate incident of a data crash down for the computer receiving compaction data from the Oedometer; several days of data were lost. We did manage to save the data belonging to first days and last days, thus enabling us to know the exact sample size at start and in the end.

7.10 FURTHER WORK

Further work should be done to find a closer relation between sealing effectiveness of drained bentonite mud column and height of the sand plug above. Studies and tests should be carried out on mixing of nanoparticles; with a wide particle size distribution, into the bentonite mud and check for any effects it might have on the sealing properties of mud. This should be tried linked to the effectiveness of the thin filter formed at the interface of bentonite mud and sand. Theoretically, the nanoparticles would contribute to tighten the filter even more making it an effective sealant. It would be interesting to see if this filter could be made larger, forming its own column and how effective this column would be sealing for any pressing fluids from below. Here the Oedometer used, could be made use of to make such a filter and study its properties.

The Oedometer could also be used to conduct extra and more comprehensive testing on bentonite, like investigating the additional effect of heat on the sealing properties of the material.

8. CONCLUSION

- Water does not transport through mud by means of its pores. This has been the case in every single test performed for this thesis.
- Injection flow into the pipe results in compression of bentonite mud and the flow cannot be considered as flow of water going through the mud.
- As bentonite mud is being drained under compression, the pore water having constant pressure then transports into sand column which initially has atmospheric pressure. When this pressure changes, the drained compression that the mud was undergoing so far is converted into undrained compression were pore water no longer has constant pressure, but increasing with increased confining pressure.
- Restraining mud expansion by means of clamp helps reduce deformation of mud and possibly the loss of friction between mud and inner pipe wall.
- Drained bentonite mud has a rapid rate of volume changes. The magnitude of the overall deformation here is large.
- Restraining the expansion of drained bentonite mud helps diminish volume changes and decrease the overall deformation compared to the case of unrestrained expansion of the same mud.
- After compressing bentonite mud up to a certain level, the pressing water always finds the path, in shape of channels or beams, between bentonite mud column and inner pipe wall as the easiest escape route to take in its way upward to the sand column placed on top of mud column. The reason for this is thought to be due to friction loss between mud and pipe wall.
- Pore fluid helps carry some of the uniaxial stress applied onto the mud. The effective stress carried by mud bulk is accordingly decreased.
- When magnitude of stress carried by pore fluid equals the stress carried by bulk frame of mud, criterion for hydraulic fracture starts to be fulfilled.
- It was found that when sand column is saturated with water and top outlet on the pipe is closed, water; starting from the already formed beams or channels, have two possible paths. The first one is proceeding upward between the mud column and inner wall of pipe. The second path is propagating into the mud radially in an explosive manner.
- Water propagation into bentonite starts when hydraulic fracturing criterion is met. This done when effective stresses inside bentonite become negative, meaning that the stresses carried by pore fluid are bigger than that carried by mud framework.
- Compaction or draining of hydrated bentonite and bentonite mud contributes to make the material more resilient to compressive stresses. The framework in other words, carries larger portions of the compressive stresses compared to stresses carried by pore fluid.
- Barite settling, according to our experimenting, does not constitute a good sealant for water under pressure.
- Water propagation through mud, as far our experiments go, is related to hydraulic fracturing of bentonite mud.

- The degree of compaction or drainage of hydrated bentonite dictates to a great deal its sealing properties.

9. REFERENCES

[1] Englehardt, J., Wilson, M.J. and Woody, F. (2001). *New Abandonment Technology New Materials and Placement Techniques.* Paper SPE 66496 presented at the SPE/EPA/DOE Exploration and Production Environmental Conference, San Antonio, Texas, USA, 26-28 March

[2] Carl, M. A. (2004). *Final Close-Out Report*. Submitted by The Interstate Oil and Gas Compact Commission (IOGCC), loaded 15.02.2013 from http://www.netl.doe.gov/kmd/cds/disk23/E-Regulatory%20Streamlining/General%5C15336%5C15336%20IOGCC%20final.pdf

[3] Clark, J. and Salsbury, B. (2003). *Well Abandonment Using Highly Compressed Sodium Bentonite – An Australian Case Study.* Paper SPE 80592 presented at SPE/EPA/DOE Exploration and Production Environmental Conference, San Antonio, Texas, USA, 10-12 March

[4] Dullien, F.A.L. (1992). *Porous Media, Fluid Transport and Pore Structure*. 2nd Edition, Academic Press, Inc.

[5] Bear, J. (1972). *Dynamics of Fluids in Porous Media*. American Elsevier Publishing Company, Inc.

[6] Clifford, K. Ho and Stephen, W. Webb (2006). *Gas Transport in Porous Media.* Volume 20, Springer

[7] Leverett, M. C. (1938). *Flow of Oil-water Mixtures through Unconsolidated Sands.* Part of a thesis submitted to the Massachusetts Institute of Technology in partial fulfillment of the requirements for the degree of Doctor of Science in Chemical Engineering. Massachusetts, USA

[8] Zolotukhin, A. B. and Ursin, Jann-Rune (2000). *Introduction to Petroleum Reservoir Engineering.* Høyskoleforlaget – Norwegian Academic Press

[9] Jaeger, J.C., Cook, N.G.W., Zimmerman, R.W. (2007). *Fundamentals of Rock Mechanics*. 4th Edition, Blackwell Publishing

[10] Detournay, E. and Cheng, A. H. -D. (1988). *Poroelastic Response of a Borehole in a Non-hydrostatic Stress Field.* International Journal of Rock Mechanics and Mining Sciences & Geomechanics Abstracts. Volume 25, issue 3, Pergamon Press

[11] Rudnicki, J. W., and Hsu, T. -C. (1988). *Pore Pressure Changes Induced by Slip on Permeable and Impermeable Faults*. Journal of Geophysical Research: Solid Earth. Volume 93, issue B4, American Geophysical Union

[12] Biot, M. A. (1941). *General Theory of Three-Dimensional Consolidation.* Journal of Applied Physics. Volume 12, No. 2, American Institute of Physics

[13] Detournay, E. and Cheng, A. H. –D. (1993). *Fundamentals of Poroelasticity* in *Comprehensive Rock Engineering.* Volume 2, Pergamon Press

[14] Norris, A. (1992). *On the Correspondence between Poroelasticity and Thermoelasticity.* Journals of Applied Physics. Volume 71, issue 3, American Institute of Physics

[15] Boley, B. A. and Weiner, J. H. (1960). *Theory of Thermal Stresses*. John Wiley & Sons, Inc.

[16] Fahrenthold, E. P., and Cheatham, J. B. (1986). *An Approximate Rock Stress Field for Steady Flow into Production Casing*. Journal of Energy Resource Technology. Volume 108, issue 2.

[17] Zimmerman, R. W. (2000). *Coupling in poroelasticity and thermoelasticity.* International Journal of Rock Mechanics and Mining Sciences. Volume 37, issue 2.

[18] Zimmerman, R. W. (1991). *Compressibility of Sandstones*. Elsevier Publishing

[19] Geertsma, J. (1957). *The Effect of Fluid Pressure Decline on Volumetric Changes of Porous Rocks*. Petroleum Transactions, AIME. Volume 210.

[20] Gassmann, F. (1951). *Elastic Waves through a Packing of Spheres.* Society of Exploration Geophysicists. Volume 16, issue 4.

[21] Digby, P. J. (1981). *The Effective Elastic Moduli of Porous Granular Rocks.* Journal of Applied Mechanics. Volume 48, issue 4.

[22] Anagnostopoulos, A. (1993). *Geotechnical Engineering of Hard Soils – Soft Rocks*. Balkema and Rotterdam.

[23] Zimmerman, R. W., Somerton, W.H. and King, M. S. (1986). *Compressibility of Porous Rocks.* Journal of Geophysical Research. Volume 91, issue B12.

[24] Carpenter, C. B. and Spencer, G. B. (1940). *Measurements of compressibility of consolidated oil-bearing sandstones*. Report 3540, United States Bureau of Mines. Denver.

[25] Dobrynin, V. M. (1962). *Effect of Overburden Stress on some Properties of Sandstones*. Society of Petroleum Engineer Journal. Volume 2, No. 4.

[26] Anderson, O. L., Schreiber, E., Liebermann, R. C., and Soga, N. (1968). *Some Elastic Constant Data on Minerals Relevant to Geophysics*. Review of Geophysics. Volume 6, issue 4.

[27] Domenico, S. N. (1977). *Elastic Properties of Unconsolidated Porous sand Reservoirs*. *Geophysics*. Volume 42.

[28] Newman, G. H. (1973). *Pore-Volume Compressibility of Consolidated, Friable, and Unconsolidated Reservoir Rocks under Hydrostatic Loading.* Journal of Petroleum Technology. Volume 25, No. 2.

[29] Fabre, D. and Gustkiewicz, J (1997). *Poroelastic Properties of Limestones and Sandstones under Hydrostatic Conditions.* International Journal of Rock Mechanics and Mining Sciences & Geomechanics Abstracts. Volume 34, issue 1.

[30] Carroll, M. M., and Katsube, N. (1983). *The Role of Terzaghi Effective Stress in Linearly Elastic Deformation*. Journal of Energy Resources Technology. Volume 105, issue 4.

[31] Zimmerman, R. W., Myer, L. R., and Cook, N. G. W. (1994). *Grain and Void Compression in Fractured and Porous Rock*. International Journal of Rock Mechanics. Volume 31.

[32] Murphy, W. F, Winkler, K. W., and Kleinberg, R. L. (1984). *Frame Modulus Reduction in Sedimentary Rocks: The Effect of Adsorption on Grain Contacts.* Geophysical Research Letters, 11.

[33] Zimmerman, R. W. (1985). *Discussion of the Constitutive Theory for Fluid-Filled Porous Materials* by Katsube, N., Journal of Applied Mechanics. Volume 52.

[34] Biot, M. A. (1962). Mechanics of deformation and acoustic propagation in porous media. Journal of Applied Physics. Volume 33, No. 4.

[35] Fjær, E., Holt, R. M., Horsrud, P., Raaen, A. M. and Risnes, R. (2008). *Petroleum Related Rock Mechanics.* 2nd Edition, Elsevier B. V.

[36] Skempton, A.W. (1954). *The Pore Pressure Coefficients A and B*. Geotechnique. Volume 4.

[37] Paterson, M. S. (1978). *Experimental Rock Deformation – The Brittle Field*. Springer-Verlag

[38] Terzaghi, K. (1936). *The Shearing Resistance of Saturated Soils and the Angle between the Planes of Shear*. International Conference on Soil Mechanics and Foundation Engineering. Volume 1. Harvard University Press

[39] Ahmed, T. (2001). *Reservoir Engineering Handbook.* 2nd Edition. Elsevier

[40] Corey, T. A. (1994). *Mechanics of Immiscible Fluids in Porous Media*. Water Resource Publications

[41] Rashid, S. (2013). Drilling Engineering. Department of Petroleum Engineering and Applied Geophysics. Norwegian University of Science and Technology, NTNU

[42] Wall, C.G., and Archer, J. S. (1986). *Petroleum Engineering: Principles and Practices. Springer Publishing*

[43] Torsæter, O. and Abtahi, M. (2001) *Experimental reservoir engineering – Laboratory workbook.* Institutt for Petroleumsteknologi og Anvendt Geofysikk, NTNU.

[44] Loaded from http://www2.ggl.ulaval.ca/personnel/paglover/CD%20Contents/Formation%20Evaluation%20English/Chapter%208.PDF visited 28.02.2013.

[45] Dake, L.P. (1983) *Fundamentals of Reservoir Engineering*. 8th Edition. Elsevier Publishing Company

[46] Loaded from http://infohost.nmt.edu/~petro/faculty/Engler524/PET524-2a-permeability.pdf Visited 28.02.2013

[47] Klinkenberg, L.J (1941). *The Permeability of Porous Media to Liquids and Gases*. American Petroleum Institute

[48] Jones, S.C. (1972). *A Rapid Accurate Unsteady-Sate Klinkenberg Parameter*. SPE Journal. Volume 12. No 5.

[49] Ringøen, N. (2011). *Introduction to Plug & Abandonment Forum*. Presented on P&A Workshop in Sola, Stavager.

[50] Sørheim, O. I., Ribesen, B. T., Sivertsen, T. E., Saasen, A., and Kanestrøm, Ø. (2011). *Abandonment of Offshore Exploration Wells using a Vessel Deployed System for Cutting and Retrieval of Wellheads.* Paper SPE 148859, presented at the SPE Arctic and Extreme Environments Conference and Exhibition held in Moscow, Russia, 18-20 October.

APPENDIX A

A-1

SATURATION

Saturation is defined as that fraction, or percent, of the pore volume occupied by a particular fluid (oil, gas, or water). This property is expressed mathematically by the following relationship:

$$fluid\ saturation = \frac{\text{total volume of fluid}}{\text{pore volume}} \tag{A.1}$$

Applying the above mathematical concept of saturation to each reservoir fluid gives:

$$S_o = \frac{V_o}{V_p} \tag{A.2}$$

$$S_w = \frac{V_w}{V_p} \tag{A.3}$$

$$S_g = \frac{V_g}{V_p} \tag{A.4}$$

Where S_o, S_w, S_g are saturation of oil, water and gas respectively. V_o, V_w, V_g and V_p are the oil, water, gas and pore volumes respectively. By definition the sum of all fluid saturations in the reservoir is equal to 1, as follows:

$$S_w + S_o + S_g = 1 \tag{A.5}$$

The fluids in most reservoirs are believed to have reached a state of equilibrium and, therefore, will have become separated according to their density, i.e., oil overlain by gas and underlain by water. In addition to the bottom (or edge) water, there will be connate water distributed throughout the oil and gas zones. The water in these zones will have been reduced to some irreducible minimum. The forces retaining the water in the oil and gas zones are referred to as capillary forces because they are important only in pore spaces of capillary size. Connate (interstitial) water saturation S_{wc} is important primarily because it reduces the amount of space available between oil and gas. It is generally not uniformly distributed throughout the reservoir but varies with permeability, lithology, and height above the free water table. Another particular phase saturation of interest is called the

critical saturation and it is associated with each reservoir fluid. The definitions and the significance of the critical saturation for each phase are described below. [39]

- *Critical oil saturation, S_{oc}*

  For the oil phase to flow, the saturation of the oil must exceed a certain value which is termed critical oil saturation. At this particular saturation, the oil remains in the pores and, for all practical purposes, will not flow.

- *Residual oil saturation, S_{or}*

  During the displacing process of the crude oil system from the porous media by water or gas injection (or encroachment) there will be some remaining oil left that is quantitatively characterized by a saturation value that is larger than the critical oil saturation. This saturation value is called the residual oil saturation, S_{or}. The term residual saturation is usually associated with the non-wetting phase when it is being displaced by a wetting phase.

- *Movable oil saturation, S_{om}*

  Movable oil saturation S_{om} is another saturation of interest and is defined as the fraction of pore volume occupied by movable oil as expressed by the following equation:

  $$S_{om} = 1 - S_{wc} - S_{oc} \qquad \text{(A.6)}$$

  where S_{wc} = connate water saturation and S_{oc} = critical oil saturation

- *Critical gas saturation, S_{gc}*

  As the reservoir pressure declines below the bubble-point pressure, gas evolves from the oil phase and consequently the saturation of the gas increases as the reservoir pressure declines. The gas phase remains immobile until its saturation exceeds certain saturation, called critical gas saturation, above which gas begins to move.

- *Critical water saturation, S_{wc}*

  The critical water saturation, connate water saturation, and irreducible water saturation are extensively used interchangeably to define the maximum water saturation at which the water phase will remain immobile.

Flow of immiscible fluids in porous media may be conveniently subdivided into two categories: (1) *steady-state*, i.e., pressure, p, density, ρ, flow rate, q, and saturation, S, are all time invariant or constant [40]. This is considered to be a special case of a more general one which is (2) *unsteady state*, where all the above mentioned parameters change with time. Since the saturation at a given point in the system will, in general, change with time, thus displacement phenomena fall in the latter category. [4]

1.1 Interfacial Tension and Capillary Pressure

The interaction process between two or more fluids confined or not confined in small spaces; e.g. pore channels and throats are governed by some fundamental concepts. These and the affecting elements are defined in this section.

1.1.1 Saturation

When the void space of the porous medium is filled by two or more immiscible fluids, the saturation at a point with respect to a particular fluid is defined as that fraction, or percent, of the void volume occupied by that particular fluid (oil, gas or water) within a *representative elementary volume* (REV), which in usually is a core sample [5]. This property is expressed mathematically by the following relationship:

$$S_i(Fluid\ Saturation) = \frac{\text{Total Volume of Fluid } i \text{ within Sample}}{\text{Volume of Pores within Sample}}\ ;\ \sum_i^n S_i = 1 \qquad \text{(A.7)}$$

Here, i denote one particular fluid that occupies the pore volume. Since the saturations are percentages of the total 100%, then by definition the total sum of the fluid saturations equals to 1.

1.1.2 Interfacial Tension and Wettability

On a microscopic level, when two or fluids come in contact with each other, the molecules within the fluid are attracted to each other and to the molecules of the adjoining fluid, by an electrostatic force generally known as *cohesion*. If the intrafluid molecular attraction is significantly stronger than the interfluid attraction, the two fluids are immiscible. Examples

of such fluids are water, oil and gas. In the other case, the fluids may readily mix with each other and are called miscible. Furthermore, the molecules of each fluid are to some degree attracted to the molecules of an adjoining solid, by an electrostatic force called *adhesion*. When there are several fluids present at solid's surface, the one fluid that is most adhesive sticks preferentially to the solid and is called the wetting phase.

The interface between two immiscible fluids can be considered as a membrane-like equilibrium surface separating phases with relatively strong intermolecular cohesion, exposing minimum free molecular surface, and little or no molecular exchange. The cohesive force is stronger on the denser fluid's side, which means that there is a sharp change in molecular pressure across the boundary. As a result, the boundary surface – much like the rubber surface of a balloon – is in a state of tangential tension, called the interfacial tension. The magnitude of the interfacial tension represents the work, or energy, required to keep the two fluids apart in a pressure equilibrium state. In other terms, the interfacial tension is the energy needed to move molecules from the inside of the droplet to the surface and thus increasing the surface area of a droplet of the fluid by one unit [8].

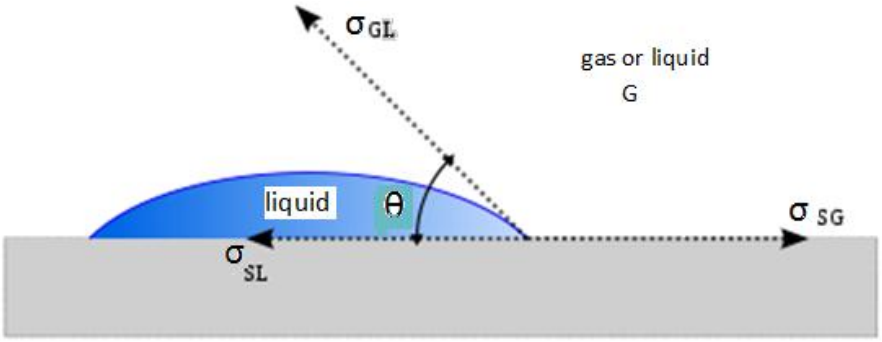

Figure A.1 Interfacial tensions for liquid-gas-solid system at equilibrium [41]

Figure (A.1) shows interfacial tensions between two immiscible fluids (liquid and gas) in contact with a solid surface. In the figure θ denotes the angle between the interface and surface. By convention, θ ($0 < \theta < 180°$) is measured through the denser fluid. σ_{SL} is the interfacial tension between solid and liquid, while σ_{GL} and σ_{SG} are the surface tensions between gas and liquid and surface and gas respectively. Equilibrium requires that

$$\sigma_{GL}\cos\theta = \sigma_{SG} - \sigma_{SL}; \qquad \cos\theta = \frac{\sigma_{SG} - \sigma_{SL}}{\sigma_{GL}} \tag{A.8}$$

From equation (3.1), called Young's equation, it follows that no equilibrium is possible if $(\sigma_{SG} - \sigma_{SL})/\sigma_{GL} > 1$. In this case, liquid will spread indefinitely over solid. This leads to the concept of wettability of a solid by a liquid. The angle θ in equation (3.1) is called the *contact angle*. The product $\sigma_{GL}\cos\theta$ is called the *adhesion tension*; it determines which fluid will *preferentially wet* the solid, i.e., adhere to it and, spread over it. [5]

The wettability of a solid can thus be defined as the tendency of one fluid to adhere to, the solid's surface in the presence of another immiscible fluid.

As shown in Figure (A.1), as the contact angle decreases, the wetting characteristics of the liquid increase. Complete wettability would be evidenced by a zero contact angle, and complete non-wetting would be evidenced by a contact angle of 180°. There have been various definitions of intermediate wettability but, in much of the published literature, contact angles of 60° to 90° will tend to repel the liquid, Figure (A.2).

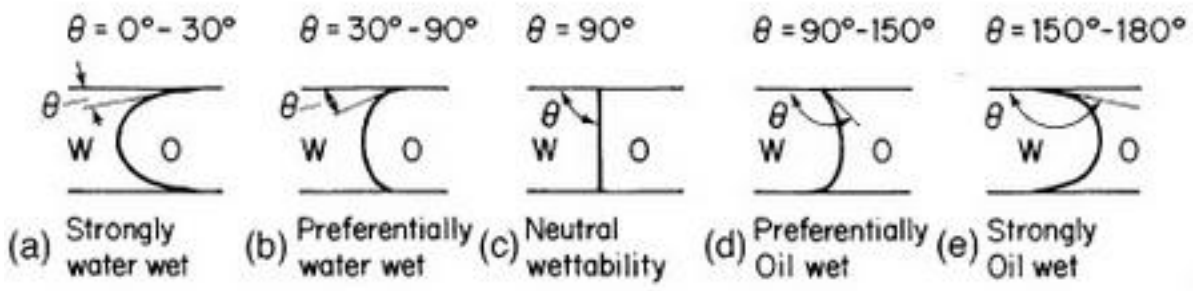

Figure A.2: *Wetting contact angles in confined capillaries [42]*

Interfacial tension and wettability may be different when a fluid-fluid interface is advancing or receding on a solid surface. This phenomenon is called *hysteresis*.

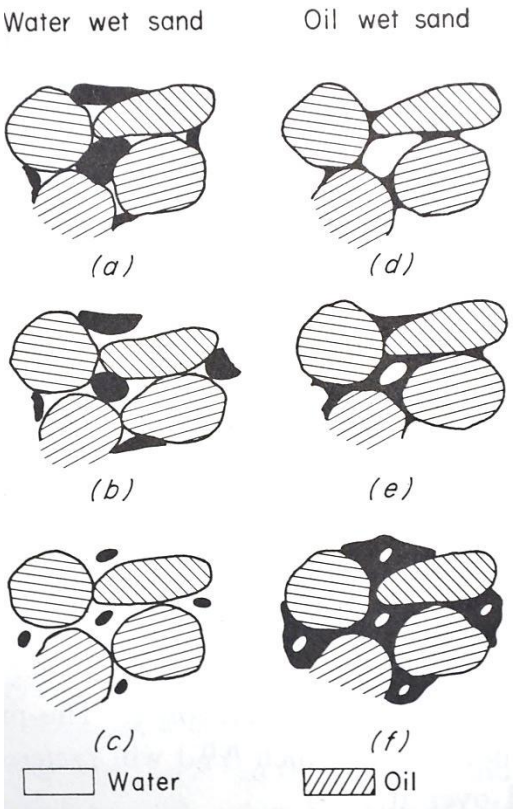

Figure A.3: Possible Fluid Saturation states [5]

With the concept of wettability we may distinguish three types of fluid saturation between the limits 0% to 100%. [5]. Figures (A.3a) through (A.3c) show water-wet sand. Figures (A.3d) through (A.3f) show oil-wet sand. At very low a very low water saturation Figure (A.3a),

water forms rings called pendular rings around the grain contact points. At this low water saturation the rings are isolated and do not form continuous water phase, except for a very thin film of water of nearly molecular thickness on the grains' surfaces. Practically no pressure can be transmitted from one ring to the next within the water phase. As the wetting phase saturation increases, the pendular rings expand until a continuous wetting fluid phase is formed. The saturation at which this occurs is called *equilibrium saturation to the wetting phase.* Above this critical saturation, the saturation is called *funicular* and the flow of the wetting phase is possible. As the saturation of the wetting phase increases, a situation develops on which the non-wetting fluid is no longer a continuous phase; it breaks into individual droplets lodged in the larger pores Figure (A.3c). The non-wetting phase is then said to be in a state of *insular saturation*. A globule of this type can move only if a pressure difference sufficient to squeeze it through capillary restrictions is applied across it in the wetting phase. Similar considerations may be applied to the oil-wet sand, Figure (A.3d, e, f). [*5*]

1.1.3 Capillary Pressure

When two immiscible fluids are in contact, a discontinuity in pressure exists between the two fluids, which depend upon the curvature of the interface separating the fluids. This curvature is a result of the stronger adhesive force of the wetting fluid: an axisymmetric meniscus develops, convex towards the wetting fluid, and the angle of the meniscus contact to the solid's surface is the wetting (contact) angle, θ. The pressure difference along the discontinuity described is called the capillary pressure and it is referred to by p_c. In short p_c is the molecular pressure differences between the wetting and non-wetting fluid and in principle can be applied to any pair of immiscible fluids, confined or not. *Capillary pressure equation is as follow:*

$$p_c = p_{nw} - p_w \tag{A.9}$$

Here, p_w is the pressure in the wetting fluid by and p_{nw}, is the pressure in the non-wetting fluid. That is, the pressure excess in the non-wetting fluid is the capillary pressure, and this quantity is a function of saturation. This is the defining equation for capillary pressure in a porous medium.

Temperature has also an effect on the magnitude of capillary pressure. Consider a liquid that has an interface with a gas, then some molecules of the liquid will be found in a vapor phase in the gas above the interface. These molecules contribute to reduce the surface tension. When temperature increases; the concentration of the vapor phase increases, and the surface tension decreases. At the critical point there are as many molecules in the gas phase as in the liquid phase, the interface effectively disappears, and the surface tension becomes zero. [43]

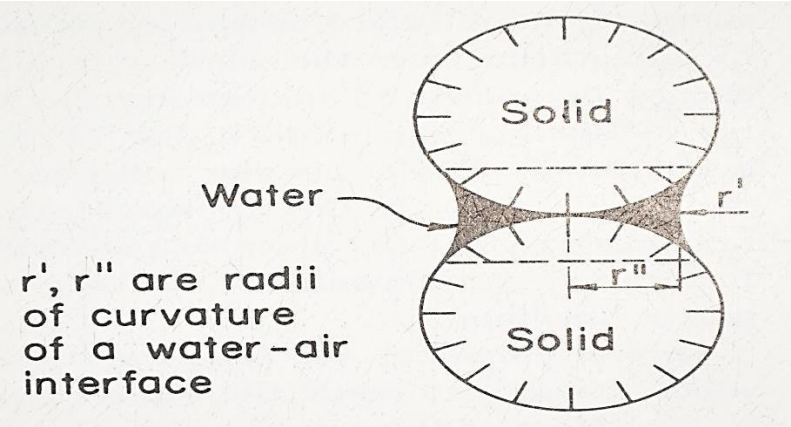

Figure A.5: Curvature radii for a water-air interface [5]

Figure (A.5) shows r' and r'' for a water-air interface in a pendular ring. By considering the change in direction of the forces acting on opposite sides of the curvature separating the two fluids, we obtain:

$$\Delta p = p_c = p_{nw} - p_w = \sigma\left(\frac{1}{r'} + \frac{1}{r''}\right) = \frac{2\sigma}{r^*} \qquad \text{(A.10)}$$

Where r*=r'=r'' is the mean radius of curvature (2/r* = 1/r' + 1/r''). Equation (A.10) is known as the Laplace equation for capillary pressure. The capillary pressure is thus a measure of the tendency of a porous medium to suck in the wetting fluid phase or to repel the non-wetting fluid phase.

In actual porous medium, all terms in equation (A.9) have the meaning of a *statistical average taken over the void space in the vicinity of a considered point in the porous medium*. Because of the dependency of p_c locally (i.e., within each pore) on interfacial tension σ and r*(which is of the order of magnitude of the pore or grain size), it depends on the geometry of the void space (e.g., in terms of the contact angle θ) and the degree of saturation S. in natural porous media, the geometry of the void space is extremely irregular and complex and cannot be defined through the values or r' and r'' obtained by integrating over the whole interface, satisfying the condition that a minimum energy be consumed in forming the surface. Instead, an idealized model of the pore space may be adopted for which the relationship $p_c = p_c(S_w)$ may be derived. Obviously this idealized approach can only indicate the effects of various factors buy fails to yield the macroscopic relationship $p_c = p_c(S_w)$ for any idealized medium. Laboratory experiments are the only way to derive this relationship for any given porous medium.

Several empirical and semi-empirical expressions are available in the literature [J. Bear], which attempt to relate the capillary pressure to medium and fluid properties and to S_w. Most of them are based on one of the idealized porous media models. For example, for a capillary tube of radius r, we obtain:

$$p_c = \left(\frac{2\sigma}{r}\right)\cos\theta \qquad \text{(A.11)}$$

On should recall that (arbitrarily) r in equation (A.11) is taken as negative. For other shapes of the cross-section, 2/r is replaced by 1/r*, where r* is some equivalent radius equal to the ratio of volume to surface of the capillary. A semi-empirical approach showing that the function [7]:

$$J = J(S_w) = \left(p_c / \sigma \right) \sqrt{k / n}; \quad p_c = p_c(S_w) \tag{A.12}$$

Called the *J-Leverett function*, reduces to a common curve when plotted for several unconsolidated sands Figure (A.6). In equation (A.12), k is the medium's permeability, n is its porosity and the ration $(k/n)^{1/2}$ may be interpreted as some mean pore diameter.

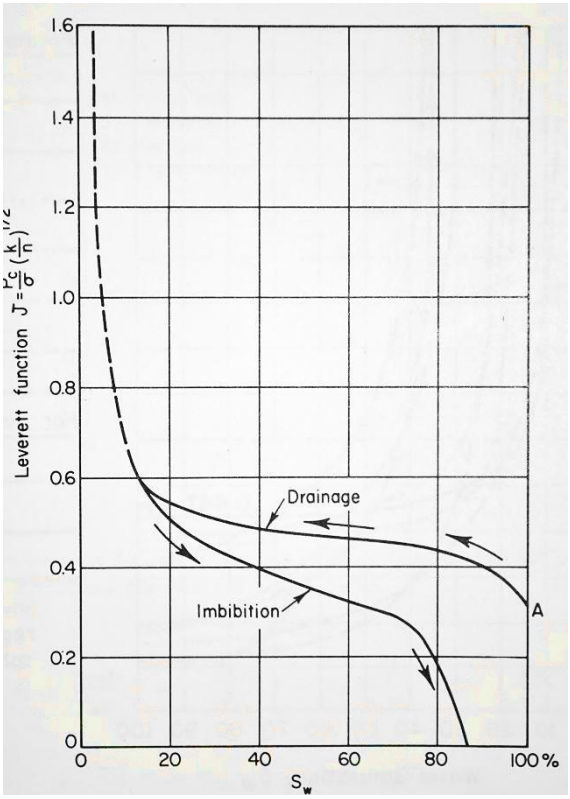

Figure A.6 Typical Leverett functions for sand [7]

Some authors suggest:

$$J(S_w) = \left(p_c / \sigma \cos\theta \right) \sqrt{k / n} \tag{A.13}$$

Other authors show that different curves $J(S_w)$ characterize different formations Figure (A.7).

Capillary pressure is a subject to *hysteresis* as the contact angle is a function of the direction of displacement; θ may have different value if equilibrium is approached by advancing or receding over a surface. This character of the contact angle is the reason for the difference in capillary pressure curves, $p_c = p_c(S_w)$ derived from a static experiment and those derived under dynamic conditions. Another mechanism causing hysteresis is the geometry of the void space with many bottlenecks. This is called the *ink-bottle effect*.

Because of the hysteresis phenomena, the relationship between *J*-function (or the capillary pressure) and S_w are not unique and we cannot determine p_c from knowledge of S_w,, or vice versa, without knowing the past wetting-drying history of the sample considered. [5]

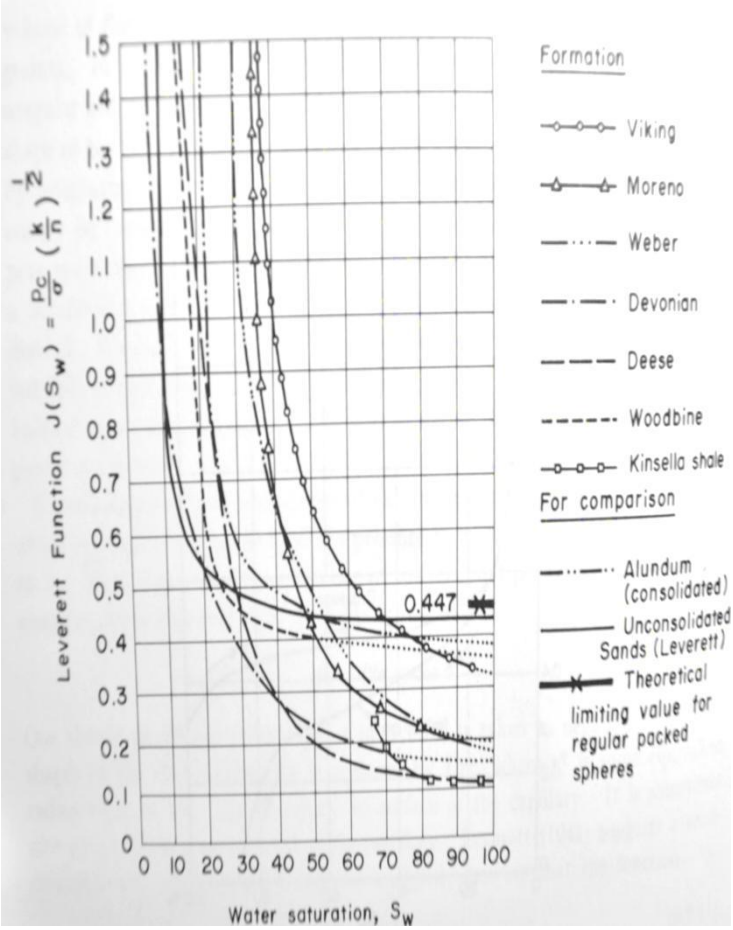

FIGURE A.7: LEVERETT FUNCTION FOR VARIOUS FORMATIONS [5]

1.2 SATURATION AND CAPILLARY PRESSURE

1.2.1 THRESHOLD PRESSURE AND SATURATION DISTRIBUTION

Based on the previous sections, we can conclude that the static equilibrium distribution of fluid saturations in a petroleum reservoir prior to production is governed by pore space characteristics, particularly by the pore channel diameters and their frequency distribution. As hydrocarbons migrate into a reservoir trap, the non-wetting fluids (oil or gas) enter the pore space initially occupied by the wetting fluid (water). For the non-wetting phase to displace the wetting phase, some driving force, or pressure differential is required to overcome the threshold capillary pressure, also known as entry pressure. This force is equivalent to the minimum injection pressure. In the case of oil, the droplets initially

retarted by the threshold pressure P_c – amalgamate with other arriving droplets into progressively longer filaments, until their increased buoyancy allows them to displace the water and eventually move to the top of the reservoir. Gas has due to its very low density and viscosity, has much less problem with overcoming the threshold pressure and migrates easily ahead of oil.

The threshold capillary pressure determines the height by which the level of 100% water saturation in the reservoir exceeds the free water level (FWL). The level of 100% water saturation is then, in practice, the level of the capillary rise of water in the largest pore channels, Figure (A.8). This level is often called the edge water level (EWL) and considered the reservoir's physical water-oil contact (WOC). The FWL is the level of 100% saturation in conditions free of capillary pressure influence.

The relationship between EWL and capillary pressure can be derived by considering equilibrium between capillary pressure and gravity force (fluid weight). Using the FWL as a datum and defining its position in the reservoir as the level where the oil-zone pressure, p_o, equals the water-zone pressure, p_w, we obtain:

$$p_{c(FWL)} = p_o - p_w = 0 \tag{A.14}$$

At any particular height (h) above FWL, the respective fluid pressures are:

$$p_o = p_{FWL} - \rho_o gh \tag{A.15}$$

$$p_w = p_{FWL} - \rho_w gh \tag{A.16}$$

And the corresponding capillary pressure is:

$$p_c = p_o - p_w = (p_{FWL} - \rho_o gh) - (p_{FWL} - \rho_w gh) = gh(\rho_w - \rho_o) \tag{A.17}$$

The height of any particular water saturation, h_{Sw} above the FWL can be calculated as follows:

$$h_{S_w} = \frac{2\sigma_w \cos\theta}{rg\left(\rho_w - \rho_o\right)} \tag{A.18}$$

$$h_{EWL} = \frac{p_c}{g\left(\rho_w - \rho_o\right)} \tag{A.19}$$

We need to keep in mind that the reservoir rocks are mainly heterogeneous, comprised of range of lithofacies units. Each unit may have different pore characteristics and hence different capillary pressure. [8]. In our case where we know the exact composition of our mud, we consider the effect of such heterogeneities irrelevant.

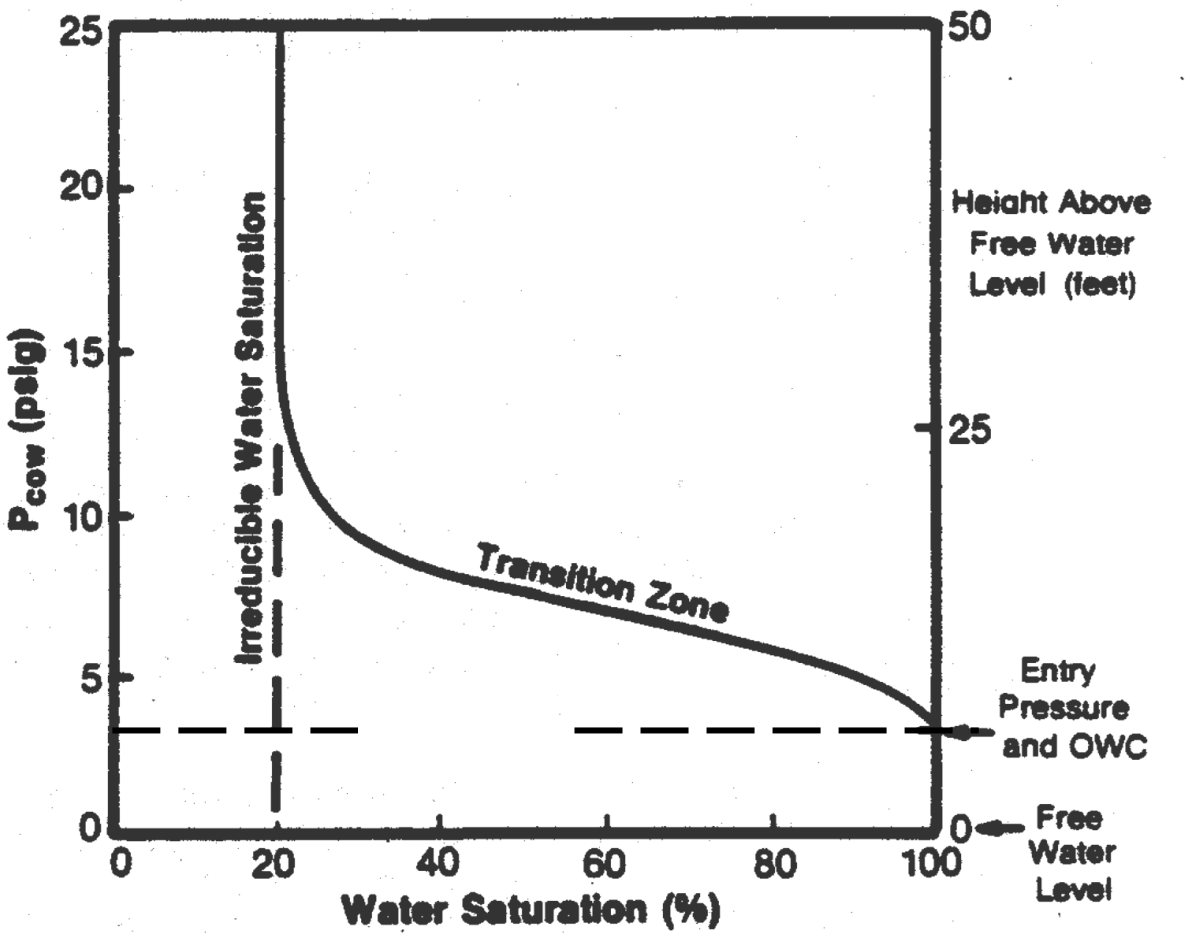

FIGURE (A.8) CONVENTIONAL CAPILLARY PRESSURE CURVE Capillary Pressure vs. Water Saturation characteristic curve after van Genuchten–Mualem [6]

As discussed earlier, the smaller the radius of the pore throat, i.e. lower permeability, the lager the threshold pressure as shown in the Figure (A.9)

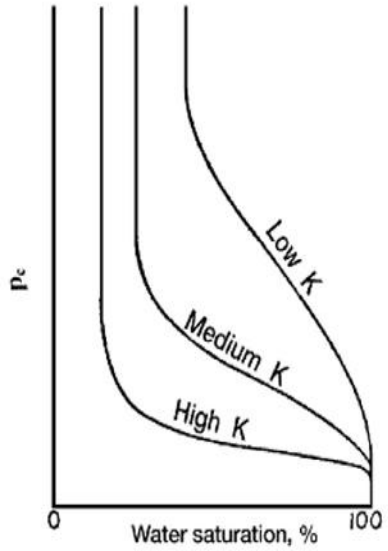

Figure A-9: Capillary pressure for different permeabilities. Notice the increasing trend of threshold pressure as we get lower permeability [44]

1.2.2 Hysteresis – Imbibition vs. Drainage

The capillary pressure as a function of saturation depends on the direction of saturation change, Figure (A.10). The drainage curve is the relationship followed during normal migration and accumulation of oil in the reservoir. Originally the reservoir was completely filled with water (water saturation of 100%). The non-wetting oil phase first enters the reservoir at entry pressure. As the capillary pressure increases, so does the oil saturation. The arrows on the drainage curve show the direction of saturation change. By convention, because wetting-phase saturation is decreasing, it is called a drainage process. Water saturation continues to reduce until it reaches irreducible water saturation, S_{wi}.

For this discussion, let us assume that the oil reservoir was at irreducible water saturation at discovery. The imbibition curve is the path followed if water is injected into the rock starting at irreducible water saturation. This is a common laboratory procedure, and is the case during water flooding an oil reservoir. In Figure (A.10), the arrows show the direction of saturation change. By convention, because wetting-phase saturation is increasing (water is being imbibed into the rock), the process is called imbibition. The difference in paths between the drainage an imbibition curves is called *hysteresis*. We note from the figure that imbibition process terminates at water saturation less than 100%, this is because not all of the oil will be displaced, some will be trapped and this is what we call the immobile oil saturation, or residual oil saturation, S_{or}.

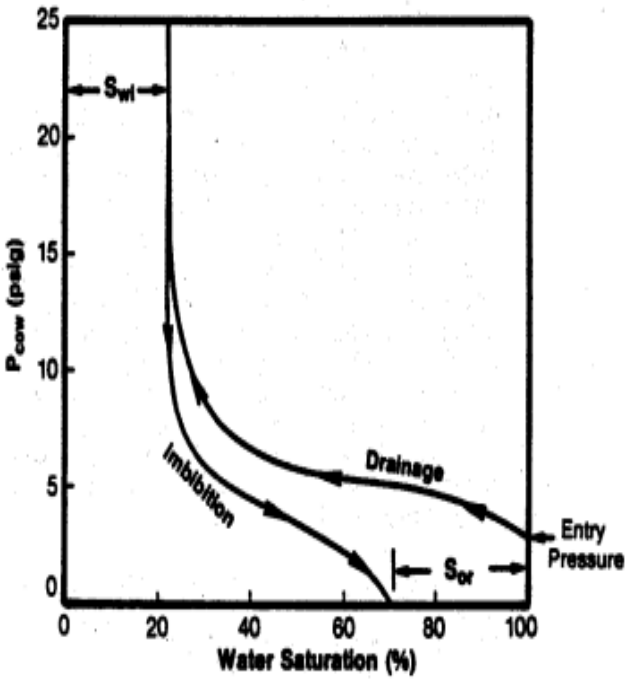

Figure A.10: Imbibition and Drainage capillary pressure curves illustrating hysteresis [9]

Starting at point A, with the core sample 100% saturated with water, the water is displaced by the oil, which is a drainage process. If the difference in phase pressures (imposed pressure differential) is plotted as a function of the decreasing water saturation the result would be the dashed line shown in Figure (A.11), the capillary pressure drainage curve.

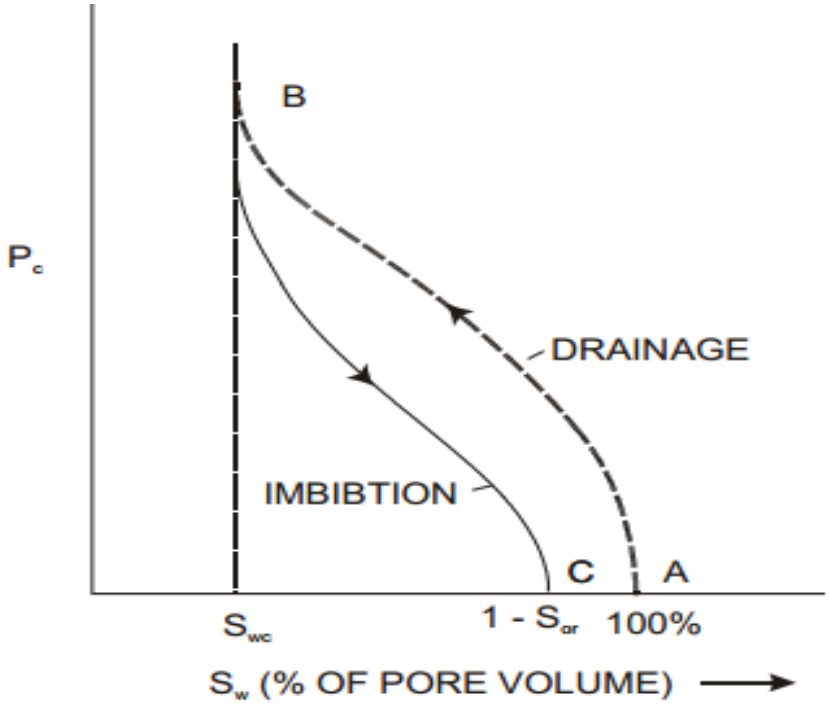

Figure A.11: Drainage and imbibition capillary pressure function [45]

At the connate water saturation (point B) there is an apparent discontinuity at which the water saturation cannot be reduced further, irrespective of the imposed difference in phase (capillary) pressure. If the experiment is reversed, by displacing the oil with water, the result

would be the imbibition curve shown as the solid line in Figure (A.11). The drainage and imbibition plots differ due to the hysteresis in contact angle, the latter being the one required for the displacement described in this chapter. When the water saturation has risen to its maximum value Sw = 1 − Sor the capillary pressure is zero (point C). At this point the residual oil saturation, Sor, cannot be reduced (Pc−negative).

1.3 PERMEABILITY

Permeability, denoted k, of a porous medium is the medium's capability to transmit fluids through its network of interconnected pores. There are numerous factors affect the magnitude and/or direction of permeability.

1. Textural properties
- pore size and pore size distribution
- Grain size and grain size distribution
- Shape of grains
- Packing of grains
2. Gas slippage
3. Amount, distribution, and type of clays
4. Type and amount of secondary porosity
5. Overburden pressure
6. Reactive Fluids
7. High velocity flow effects

Let us begin by investigating the role of textural properties on the permeability. Experimental evidence has shown that (k) is proportional with (cd), where c is a characteristic of the rock and d is the grain diameter. Bigger grains would mean greater permeability. The dimensions of permeability are square length (m^2), which is directly related to the cross sectional area of the pore throats. Therefore as grain size increases, so will the pore throat size and a subsequent increase in permeability occurs. In Figure (A.12) an artificial mixing of sands illustrates the significant effect of grain size on permeability. As can be seen, an approximate 25:1 increase in permeability occurs from coarse to very fine grains.

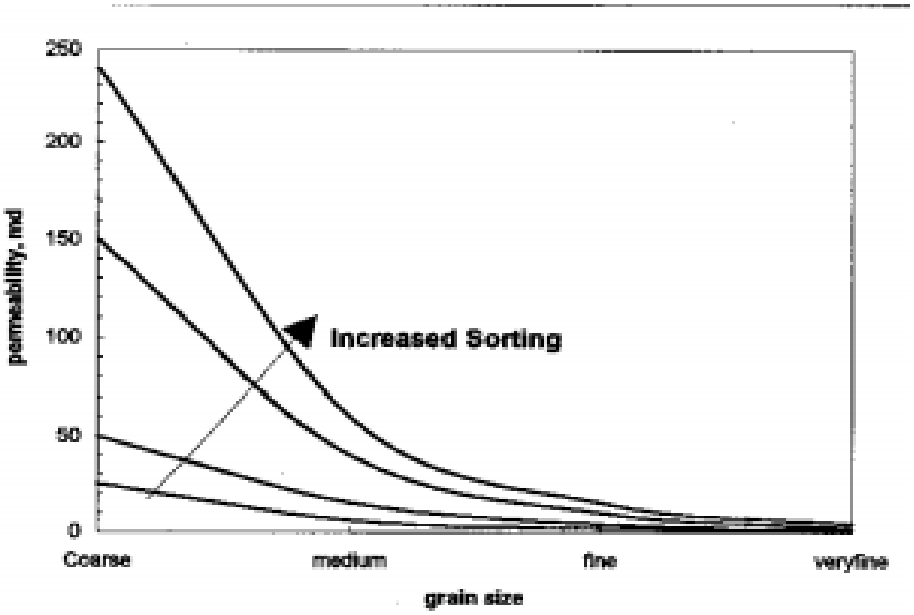

Figure (A.12) Effect of grain size and sorting on permeability [46]

1.3.1 THE KLINKENBERG EFFECT

I start by quoting L. J. Klinkenberg on the matter of his effect, "- *in many cases-at least for formations of moderately high permeability-not of the first importance for practical purposes*" [47]. But in our case where the permeability is in the range of [0,1 - 1 mD] and the pressure in the range of 1-15 bars, I found it useful to include this in the thesis. This was, wrongly, assumed to be the case at the time when flow into pipe was considered as flow through bentonite mud.

The true absolute permeability of porous rock is an intrinsic property of the rock, reflecting its internal structure. The permeability of a rock is a constant value, unchanged by different types of fluids that have different viscosities or other physical properties. This rule is followed by all liquids at laminar flow rates that are nonreactive with the rock. However, when gases are used as the flowing fluid at low pressures, calculated permeability may be greater than true permeability of the rock.

In liquid laminar flow, the velocity profile of the liquid is at its max at the center of the passageway and zero at the walls. However, when using gas in the same flow system, the gas velocity profile is not zero at the walls, but has a finite velocity in the direction of flow. Here it is assumed that the gas is in steady state and the flow is laminar.

Gas molecules are in constant motion, colliding with one another after traveling an average distance equal to the "mean free path." At lower pressures, the mean free path is greater, and the distance between molecular collisions is increased. Internal resistance to flow is provided by gas molecular collisions with the walls. At any location on a wall, there will be

some periods when no gas molecule is in contact with the wall, yet the congregation of gas molecules is continuing its movement through the pore due to molecular diffusion (slip) and not pressure differential. During these periods of no wall contact, flow is being achieved without the normally expected friction loss at the wall. The result is that the gas molecules get through the porous medium more easily than expected (i.e., the calculated permeability of the rock or capillary tube would be artificially high). As expected, gas flow at higher pressures reduces the mean free path between molecular collisions, and the calculated permeability more closely approximates the true absolute permeability of the rock. [7]

Klinkenberg [47] conducted experiments on this phenomenon and conclude that

- Gas permeability is a function of the gas composition
- Gas permeability is a function of mean pressure
- The equivalent liquid permeability is independent of the above two factors

He presented a useful relationship:

$$k_g = k_L\left(1+\frac{b}{\overline{p}}\right) \qquad \text{(A.20)}$$

k_g is the corrected Klinkenberg permeability for gas, while k_L is the absolute permeability of the medium. The parameter b is Klinkenberg correction factor, a constant for a particular gas in a particular porous medium, while p is the mean flow pressure of the gas.

The Klinkenberg correction to reduce gas permeability varies with the magnitude of the absolute permeability. Actually, the constant b declines with increasing absolute permeability. Several correlations have been developed; the most recent [48] is:

$$b\ [kPa] = k_L^{-0,36}\ [mD] \qquad \text{(A.21)}$$

Capillary pressure per definition is difference between pressure found in the non-wetting phase and that found in the wetting phase. That is, the pressure excess in the non-wetting fluid is the capillary pressure, and this quantity is a function of saturation and is affected by among others temperature.

1.3.2 Relative Permeability

The dynamic behavior of a system in which two fluids are flowing simultaneously is best described in terms of its "effective permeability" to either phase, M.C. Leverett. Relative permeability is a concept used to relate the absolute permeability, 100% saturation of one fluid, of a porous system, to the effective permeability of a particular fluid in the system,

when this particular fluid only occupies a fraction of the total pore volume. For incompressible fluids flowing through a system of uniform cross section, the effective permeability of the two phases, in Darcy's, may be defined by the equations:

$$k_j = \frac{q_j \cdot \mu_j \cdot L}{A \cdot \Delta p} \qquad \text{(A.22)}$$

Where k_j, q_j μ_j are the effective permeability, flow rate and viscosity of fluid *j* respectively. L is the length traveled, A is cross sectional area of the medium (not pores) and Δp is the pressure difference.

Relative permeability, k_{rj} is the ratio of the effective permeability of a particular fluid, *j*, to the absolute permeability of that medium, k, as follows:

$$k_{rj} = \frac{k_j}{k} \qquad \text{(A.23)}$$

Since the effective permeability is always less than the absolute permeability, the relative permeability lies between 0 and 1, and the sum of relative permeabilities for all phases in the same medium is less than the absolute permeability. The relationship between relative permeability and wettability for a two phase flow (oil and water) and (gas and water) is shown in Figure (A.13).

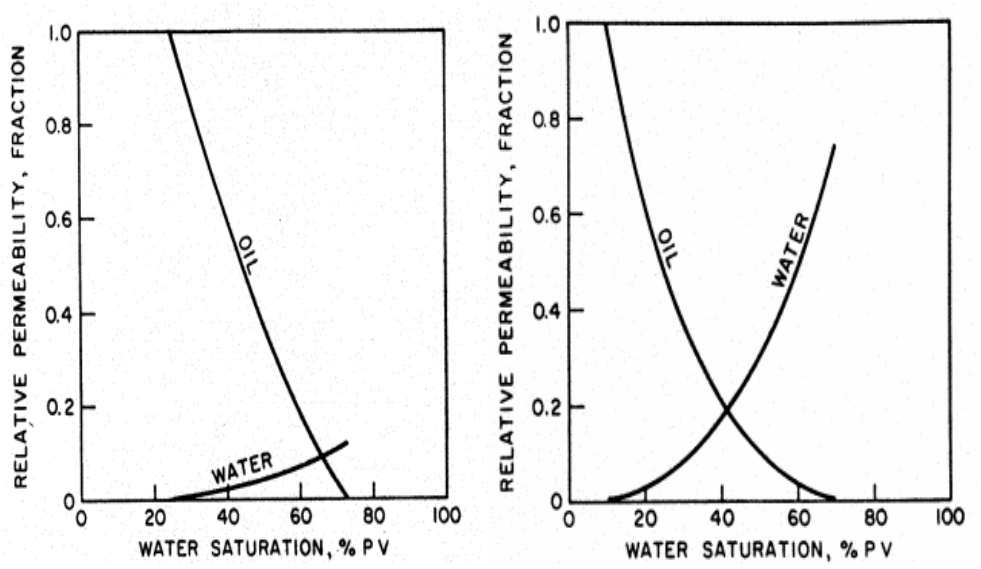

Figure A.13: Characteristics of typical relative permeability for a two phase flow, where water is the wetting phase(left) and oil is the wetting phase(right) [8]

In the Figure (A.13 left), k_{ro} is the non-wetting phase and has the curve shape characteristic of the non- wetting phase (S-shaped). The typical shape of the wetting phase is that of the k_{rw} curve (concave upward throughout). Preferential wettability is also shown by the crossover of the two curves. In Figure (A.13 left), the curves cross at a water saturation greater than 50%, which indicates a system that is probably water wet. If the curves had crossed at water saturation less than 50%, the system would probably be preferentially oil

wet, and the shapes of the curves would be reversed. It is common for laboratory-measured relative-permeability curves to cross very near the 50% water saturation and the shape of both curves to be similarly concave up. This would indicate intermediate wettability; however, no hard and fast rules can be established. Each system must be investigated individually, and the discussion above is only a generalization. Residual oil saturation, irreducible water saturation, curve shapes, and crossover points must all be considered when investigating wettability. Figure (A.13 right) is an example of an oil-wet system for comparison.

A-2

RHEOLOGICAL CLASSIFICATION OF FLUIDS

Two types of fluids are encountered in the petroleum drilling and production operations: *Newtonian fluids* and *non-Newtonian* fluids. The viscous forces present in a simple Newtonian fluid are characterized by the fluid viscosity. Examples of such fluids are water, gases and thin (high gravity) oils. These kinds of fluids will exhibit direct proportionality between *shear stress* and resulting *rate of shear* (γ) with pressure and temperature kept constant. Mathematically, Newtonian fluids are defined by

$$\tau = \mu\left(\frac{-dv_r}{d_r} = \gamma\right) \qquad \text{(A.13)}$$

Where $(dv_r/d_r)=\gamma$ is shear rate for the laminar flow within a circular pipe. As we see from Fig.4.2 the plot of Shear stress τ versus shear rate γ for Newtonian model shows a straight line passing through the origin with absolute viscosity μ as slope.

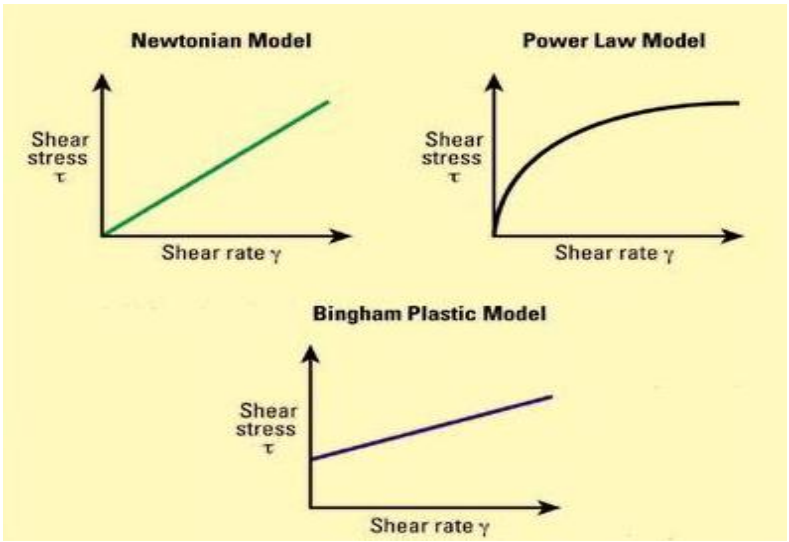

FIGURE A.2 DIFFERENT RHEOLOGICAL MODELS [43]

Fluids that are too complex to be characterized by single value for viscosity and thereby do not exhibit a direct proportionality between shear stress and shear rate are classified as a non-Newtonian fluid. Drilling mud, cement slurries, heavy oil and various gelled fracturing fluids are examples of non-Newtonian fluids.

These non-Newtonian fluids are further classified into *Bingham plastic* fluids, *power law* fluids and *time-dependent* fluids. The Bingham plastic and power law fluids are generally referred to as time-independent fluids; the magnitude of viscosity is not affected by duration of shear. Per contra, in the time-dependent fluids, the apparent viscosity at a fixed value of

shear rate and temperature, changes with the duration of time. Time dependent fluids are yet classified into *thixotropic* fluid and *rheopectic* fluid. Thixotropic fluid exhibits a decrease in shear stress with duration of shear at constant shearing rate, while rheopectic fluid shows an increase in shear stress with duration of shear at a given shearing rate and constant temperature. Drilling fluids and cement slurries are generally thixotropic.

Mathematically, the Bingham plastic and power law fluid models are represented by the following relationships:

$$\tau = \tau_y + \mu_p \left(\frac{-dv_r}{d_r} \right) = \tau_y + \mu_p \cdot \gamma \qquad \text{(A.14)}$$

Power-law fluid model:

$$\tau = K \left(\frac{-dv_r}{d_r} \right)^n = K \cdot \gamma^n \qquad \text{(A.15)}$$

Where τ_y is yield point (lbf/100ft^2), μ_p is plastic viscosity (cp), *n* is flow behavior index and *K* is consistency index. The value of n ranged between 0 and 1 and gives indication of the non-Newtonian behaviour (n = 1 for Newtonian fluid), and K refers viscosity of the fluid; the larger the K, the more viscous it is.

Back to Figure A.2 we notice that for the Bingham fluid, the plot shows a straight line with the slope equal to the plastic viscosity (μ_p) and intercept equal to the yield point τ_y . This means that for an ideal Bingham plastic fluid, the fluid exhibits rigid body behaviour until enough, e.g. τ_y , is applied and in that case will have a proportionality between shear stress and shear rate similar to that for Newtonian fluids.

For the power law fluid, a shear plot made on a log-log scale shows a straight line with a slope equal to the flow behaviour index *n* and intercepts equal to the consistency index log *K*.

In order to measure the rheological properties of the mud, a rotational viscometer is commonly used, Figure A.3. Six standard speeds and variable speed settings are normally available on rotational viscometer. In the field, however, there are usually two-speed (300 and 600 rpm) viscometers that are being used. The following equation can be used to calculate various mentioned in this section:

Newtonian fluid model:

$$\mu_a = \frac{300}{N} \theta_N \qquad \text{(A.16)}$$

$$\gamma = \frac{5.066}{r^2} N \tag{A.17}$$

Bingham plastic fluid model:

$$\mu_p = \theta_{600} - \theta_{300} = \frac{300}{N_2 - N_1}\left(\theta_{N_1} - \theta_{N_2}\right) \tag{A.18}$$

$$\gamma = \frac{5.066}{r^2} N + \frac{479\tau_y}{\mu_p}\left(\frac{3.174}{r^2} - 1\right) \tag{A.19}$$

$$\tau_y = \theta_{300} - \mu_p = \theta_{N_1} - \mu_p \frac{N_1}{300} \tag{A.20}$$

$\tau_{gel} = \theta_{\max}$ at N= 3 rpm. For the power law fluid model we use:

$$n = 3.322 \log\left(\frac{\theta_{600}}{\theta_{300}}\right) = \frac{\log\left(\frac{\theta_{N_2}}{\theta_{N_1}}\right)}{\log\left(\frac{N_2}{N_1}\right)} \tag{A.21}$$

$$K = \frac{510 \cdot \theta_{300}}{511^n} = \frac{510 \cdot \theta_N}{\left(1.703N\right)^n} \tag{A.22}$$

$$\gamma = 0.2094N \frac{\frac{1}{r^{2/n}}}{n\left[\frac{1}{r_1^{2/n}} - \frac{1}{r_2^{2/n}}\right]} \tag{A.23}$$

Where r_2 is the rotor radius (in), r_1 is bob radius (in), r any radius between bob and rotor radius (in), θ_N is the dial reading of the viscometer at speed N and N is the speed of rotation of the outer cylinder (rpm).

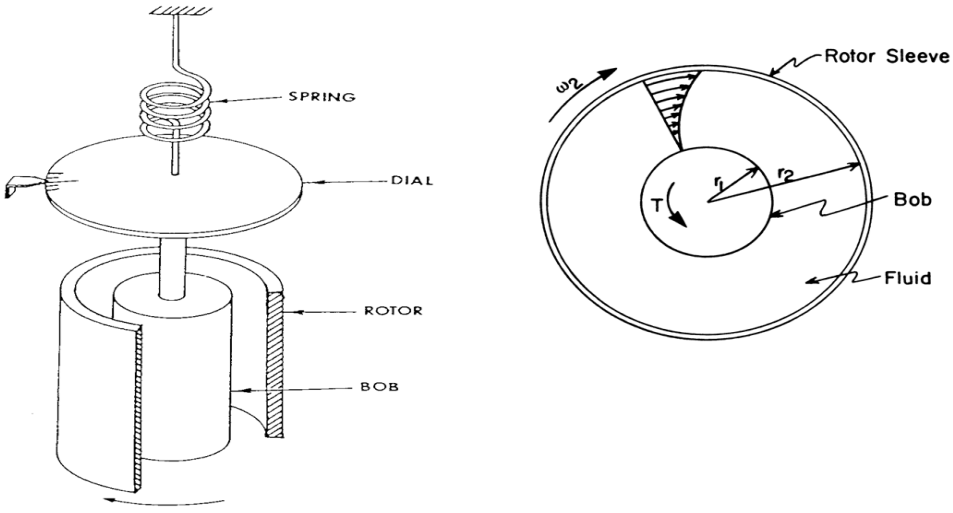

FIGUREA.3 SCHEMATIC ILLUSTRATION OF A ROTATIONAL VISCOMETER [43]

A-3

MAXWELL–BETTI RECIPROCAL THEOREM

This appendix is taken from Chapter 5, section 5.8 in the book *Fundamentals of Rock Mechanics*. Consider two sets of forces, consisting of surface tractions and body forces, which may be applied to a given body. Let these sets of forces be denoted by {F1, p1} and {F2, p2}, and let the stresses, strains, and displacements due to these two sets of forces be denoted by {τ1, ε1, u1} and {τ2, ε2, u2}. The reciprocal theorem states that the work W_{12} that would be done by the first set of forces if they acted through the displacements that are due to the second set of forces is equal to the work W_{21} that would be done by the second set of forces if they acted through the displacements that are due to the first set of forces. Both of these work terms are hypothetical work terms, computed by assuming that the final equilibrium loads act throughout the total displacement process. To prove the reciprocal theorem, we start with, from the verbal definition given above,

$$W_{12} = \frac{1}{2}\iint_{\partial B} p^1 \bullet u^2 dA + \frac{1}{2}\iiint_B \rho F^1 \bullet u^2 dV \tag{5.161}$$

$$W_{12} = \iiint_B trace\left(\tau^1 \varepsilon^2\right) dV \tag{5.162}$$

$$\begin{aligned} W_{12} &= \iiint_B trace\left\{\left[\lambda trace\left(\tau^1\right)\mathrm{I} + 2G\varepsilon^1\right]\varepsilon^2\right\} dV \\ &= \iiint_B trace\left\{\left[\lambda trace\left(\varepsilon^1\right)\varepsilon^2 + 2G\varepsilon^1\varepsilon^2\right]\right\} dV \\ &= \iiint_B \left[\lambda trace\left(\varepsilon^1\right) trace\left(\varepsilon^2\right) + 2G trace\left(\varepsilon^1\varepsilon^2\right)\right] dV \end{aligned} \tag{5.163}$$

where use has been made of the linearity of the trace operation. Furthermore, since trace (AB) **=** trace (BA), the last expression on the right-hand side of (5.163) is symmetric with respect to the superscripts 1 and 2. Hence, (5.163) shows that $W_{12} = W_{21}$.

APPENDIX B

DATA SHEET FOR BENTONITE PELLETS

The pellets used to make bentonite mud and hydrated bentonite:

	Mikolit®00	**Mikolit®300**	**Mikolit®B**
Description	Moderate swelling sealing pellet for basic swelling	The adding of bentonite results in a powerfully swelling sealing pellet, combining good sealing results with excellent application properties	Extremely powerful swelling because only pure bentonite is used. Thanks to the special production process, application properties remain good
Dimensions			
Standard length	7 – 12 mm	7 – 12 mm	7 – 12 mm
Standard diameter	± 6mm	± 6mm	± 6mm
Colour	Greyish brown	Greyish brown	Light olive
Size of the clay articles (DIN 18123)			
< 0,002 mm	53%	56%	71%
0,002 – 0,006 mm	40%	40%	29%
> 0,006 mm	7%	4%	0%
Water absorption capacity ENSLIN/NEFF (DIN 18 132)			
After 24 h	80%	160%	350%
After full swelling	100%	240%	800%
Course of water absorption			
After 1 h			190%
After 24 h			150%
After 48 h			650%
After 96 h			800%
Water impermeatibility Kf-value (DIN 18 130)	$<10^{-10}$ m/s	$< 10^{-11}$ m/s	$< 10^{-12}$ m/s
Swelling capacity Free swelling in demineralised water, 1 litre beaker, pore volume included	50 – 60%	100 – 120%	250 – 280%
Course of swelling			
Initiated after	15 min	15 min	15 min
After 1 h	15%	15%	20%
After 24 h	35%	45%	200%
After 48 h	50%	90%	250%
Moisture content DIN 18121	< 15%	< 15%	< 20%
Swelling pressure	3,5 kN/ m^3	13,0 kN/ m^3	15,0 kN/ m^3
Mineralogical main structure (RDA/IR) DIN 51001			
Kaolinite	15-20%	15-20%	20-30%
Illite/Glimmer	15-205	15-20%	
Illite-smectite	10-155	15-20%	
Smectite	10-15%	20-25%	60-70%
Quartz	25-30%	15-20%	5-10%
Other	5-10%	5-10%	5-10%
Chemical main structure (RFA)			
SiO_2	72%	70%	63%
Al_2O_3	18%	20%	21%
Fe_2O_3	2%	2%	11%
Other	8%	8%	5%
Glowing loss (DIN 18 128, 550°C)	9%	7%	5%
γ-radiation (Gamma Ray Log)	80-105 API	80-105 API	80-100 API
Bulk weight	1,1 t/m^3	1,1 t/m^3	1,0 t/m^3
Density of the pellet	2 t/m^3	2 t/m^3	1,9 t/m^3
Specific weight of the clay	2,6 t/m^3	2,6 t/m^3	2,6 t/m^3
Sinking speed in water	21 m/min	21 m/min	21 m/min

APPENDIX C

LAPONITE MANUFACTURER DATA SHEET

ROCKWOOD ADDITIVES LIMITED / ROCKWOOD CLAY ADDITIVES GMBH

PRODUCT BULLETIN/Laponite®

WWW.ROCKWOODADDITIVES.COM

Laponite RD

Description

Laponite RD is a synthetic layered silicate. It is insoluble in water but hydrates and swells to give clear and colourless colloidal dispersions. At concentrations of 2% or greater in water, highly thixotropic gels can be produced.

Application

Used for imparting a shear sensitive structure to a wide range of waterborne formulations. These include household and industrial surface coatings, cleansers, ceramic glazes, agrochemical, oilfield and horticultural products.

Typical Characteristics

Property	
Appearance	free flowing white powder
Bulk Density	1000 kg/m^3
Surface Area (BET)	370 m^2/g
pH (2% suspension)	9.8

Chemical Composition (dry basis)	
SiO_2	59.5%
MgO	27.5%
Li_2O	0.8%
Na_2O	2.8%
Loss on Ignition	8.2%

General Specifications

Property	Specification	Rockwood QA Test Code
Gel strength	22g min	ELP-L-1H
Sieve Analysis	2% Max >250 microns	ELP-L-6A
Free Moisture	10% Max	ELP-L-5A
Specifications can be agreed to meet individual requirements.		

Storage

Laponite products are hygroscopic and should be stored under dry conditions.

ROCKWOOD ADDITIVES LIMITED / ROCKWOOD CLAY ADDITIVES GMBH / SOUTHERN CLAY PRODUCTS, INC.

Rockwood Additives Limited
Moorfield Road
Widnes, Cheshire
UK WA8 3AA
Telephone: 44 (0) 151 495 2222
Fax: 44 (0) 151 420 4401

Rockwood Clay Additives GmbH
Stadtwaldstr. 44,
85368 Moosburg, Germany
Telephone: 49 (0) 8761 72 150-0
Fax: 49 (0) 8761 72 150-334

Southern Clay Products, Inc.
1212 Church Street
Gonzales, TX 78629
Telephone: 1-800-324-2891
Fax: 1-830-672-1903